GEORG-AUGUST-UNIVERSITÄT
GÖTTINGEN IN PUBLICA COMMODA SEIT 1737

Ultrafast spin dynamics in FeNi alloys

Dissertation

for the award of the degree
"Doctor rerum naturalium" (Dr. rer. nat.)
of the Georg-August-Universität Göttingen

–

within the doctoral program ProPhys
of the Georg-August-University School of Science (GAUSS)

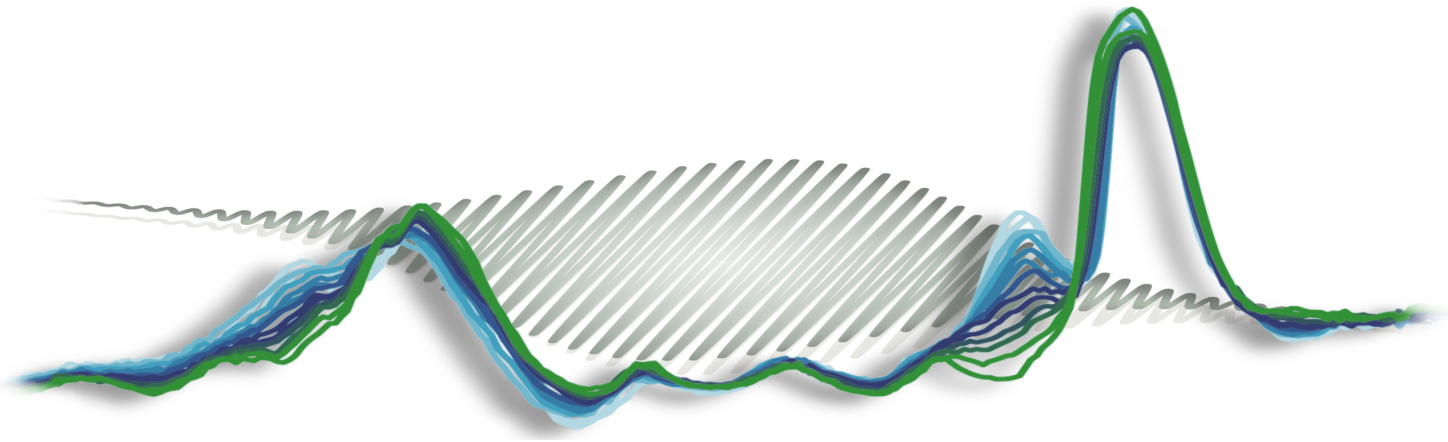

submitted by

Christina Möller

from Paderborn

Göttingen, 2023

Thesis Committee

Prof. Dr. Stefan Mathias,
I. Physikalisches Institut, Georg-August-Universität Göttingen

Prof. Dr. Claus Ropers
Max-Planck-Institut für Multidisziplinäre Naturwissenschaften

Prof. Dr. Vasily Moshnyaga,
I. Physikalisches Institut, Georg-August-Universität Göttingen

Members of the Examination Board

Reviewer:
Prof. Dr. Stefan Mathias,
I. Physikalisches Institut, Georg-August-Universität Göttingen

Second Reviewer:
Prof. Dr. Claus Ropers,
Max-Planck-Institut für Multidisziplinäre Naturwissenschaften

Further Members of the Examination Board

Prof. Dr. Martin Wenderoth
IV. Physikalisches Institut, Georg-August-Universität Göttingen

Prof. Dr. Simone Techert
Deutsches Elektronen-Synchrotron DESY, Photon Science Department

Prof. Dr. Vasily Moshnyaga,
I. Physikalisches Institut, Georg-August-Universität Göttingen

PD Dr. Salvatore R. Manmana
Institut für Theoretische Physik, Georg-August-Universität Göttingen

Date of oral examination: 18.08.2023

It is through science that we prove,
but through intuition that we discover.

- Henri Poincaré -

For Philipp and Lorenz.

Contents

1

Introduction

Light has long been a source of inspiration for mankind, not only in works of art such as paintings and photographs, but also in natural phenomena such as rainbows or fireflies. In our daily lives, light enables our visual perception of the world around us and plays a crucial role in many key technologies: Light connects the citizens of the world through the internet via optical fibers and is the basis for numerous applications in fields as diverse as healthcare, solar energy and advanced manufacturing.

In physics, light is a fundamental tool for investigating the electronic, structural, and magnetic properties of matter in a non-invasive way. There are many different techniques that use scattering of light [1–3], imaging with light [4,5] and spectroscopic measurements using multiple wavelengths [6–9]. In magnetically ordered materials, magneto-optical effects describe the change in polarization or intensity of light when light interacts with a magnetic material [10]. Hence, this change and the magnetization state of the studied system are intimately connected.

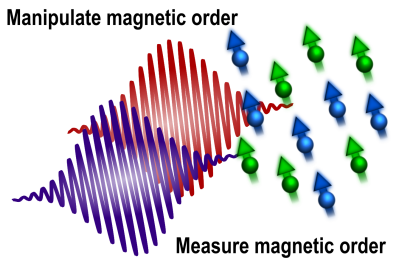

Understanding the magnetic state and dynamics of a material is of great interest in fundamental research. Light pulses cannot only be used as a tool to measure the magnetic properties of matter but also to manipulate its magnetic order. In contrast to magnetic fields (e.g., used in conventional data storage), laser pulses can be so short that they operate on the same timescale as the exchange interaction that is responsible for the existence of magnetic order itself [11]. The intrinsic timescale of the exchange interaction is around 50 fs, while the timescale of the spin-orbit interaction is between 100 fs and 1 ps (see figure 1.1), and these interactions are all accessible using ultrashort light pulses with durations down to the femto- and even attosecond regime.

Ultrafast magnetism is a vivid research field where ultrashort laser pulses are used to investigate and manipulate the magnetization on sub-ps timescales [12–14]. Multiple different mechanisms (electron-electron, electron-phonon, electron-magnon scattering; spin currents) [15–21] involved in the ultrafast demagnetization lead to complex microscopic processes. To investigate the underlying microscopic processes in ultrafast magnetism when a fs laser strongly excites the

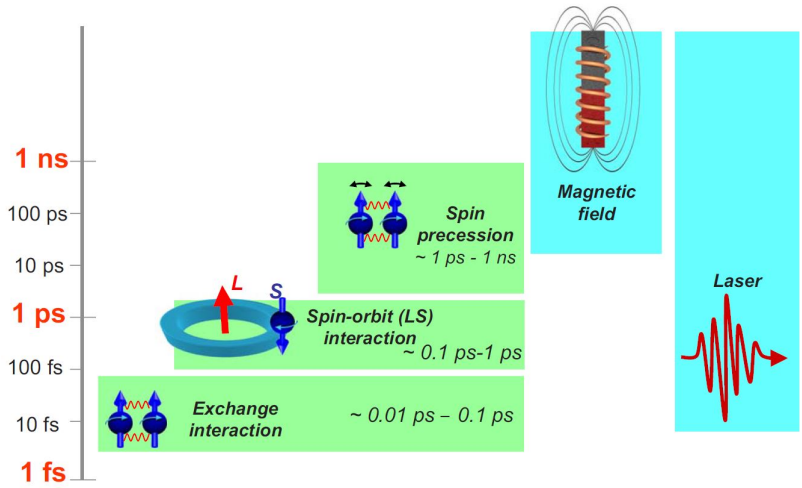

Figure 1.1.: Laser pulses can control the magnetization on much shorter timescales than magnetic fields – which is of interest for data storage technologies aiming to increase the speed of writing (and reading). Reprinted with permission from Ref. [11]. Copyright (2010) by the American Physical Society.

material and initiates the dynamics, a rich variety of magneto-optical experimental techniques were developed. These developments have been closely linked to the invention of new light sources. First, the development of modern femtosecond laser sources allows to induce and detect spin and charge dynamics by means of time-resolved methods. Synchrotrons, free electron lasers, and high harmonic sources paved the way to probe the magnetization with short wavelengths allowing for element specificity and high-resolution imaging [2]. Recent advances in THz technology have made it possible to perform broadband THz emission spectroscopy and to measure the magnetic dipole THz emission from a magnetic sample after excitation with an ultrashort laser pulse [22, 23].

The basic idea behind all magneto-optical techniques is that the magnetic nature of the material affects the transition probabilities between different energy levels and, thus, the absorption of a photon changes when the magnetization of the sample or the polarization of the light is changed. Light therefore provides indirect access to the magnetization by probing the electronic band structure, which is, however dependent on the magnetic state of the material.

There are controversial discussions about whether the magneto-optical signal in ultrafast spectroscopy is purely sensitive to the magnetization, or whether it has a strong optical contribution that might lead to misleading results. Koopmans [24] wrote in 2003 "*Clearly we are hindered by our indirect optical view on the matter.*" Zhang et al. [25] claimed to have resolved this enduring controversy because their calculations show that for photon energies below 2 eV no optical misleading contributions are to be expected in the magneto-optical response for nickel. Carva et al. [26], however, disagree and note that the calculations of Zhang et al. do not correctly address the case of an actual pump-probe experiment. According to their reply and in line with [27], the

magneto-optical Kerr effect (MOKE) signal cannot be directly linked to the magnetization for the case of a non-equilibrium electron distribution caused by a femtosecond laser pulse.

This thesis focuses on a specific magneto-optical technique using extreme ultraviolet (EUV) light: the EUV transverse magneto-optical Kerr effect (EUV T-MOKE). The initial implementation of the element-specific femtosecond Kerr setup in 2009 [28] marked the beginning of a successful series of experiments with this technique. These experiments uncovered a number of key findings in ultrafast magnetism: Superdiffusive spin currents and spin flips in Ni/Ru/Fe trilayers [21], delayed response of Ni in the exchange coupled FeNi alloys [29], and optical intersite spin transfer in the half-metallic Heusler Co_2MnGe [30], in $Fe_{50}Ni_{50}$ [31] and in Co_2MnGa [32].

The impact of purely optical contributions to the EUV T-MOKE signal were already debated in the literature [33–35] and Jana et al. [36] found that the spectrally-resolved measurement signal in EUV T-MOKE, the so-called asymmetry is not always proportional to the magnetization. This thesis provides a solution and clarifies the relation between the T-MOKE measurement signal and the magnetization by the development of a new fit routine to the data that extracts the full dielectric tensor. This new data analysis was developed to explain alarming, seemingly contradictory dynamics in FeNi alloys which we measured with EUV T-MOKE at different incidence angles. On the one hand, the new analysis explains the observed contradictory dynamics and, on the other hand, allows to disentangle the magnetic and optical contributions to the T-MOKE measurement signal. More importantly, an explicit connection can be made between the measurement signal and the element-specific changes in the transient spin-resolved occupation with the help of time-dependent density-functional theory (TDDFT) [37]. So far, only an indirect comparison between TDDFT with experiment was possible because the experimental observable (EUV T-MOKE asymmetry) and the observable from TDDFT (energy-resolved magnetic moment) were not the same. For the first time for this experimental technique, it is now possible to directly compare the same observable, the magneto-optical response function, namely the transient dielectric tensor.

The main part of this thesis focuses on long-standing problems in the interpretation of ultrafast spin dynamics in FeNi alloys. In 2012, Mathias et al. [29] found a delayed demagnetization of nickel compared to iron in the exchange coupled $Fe_{19}Ni_{81}$ alloy. These results were heavily discussed because Radu et al. [38] and Eschenlohr [39] did not observe a delayed behavior in similar systems and also different time constants for both elements using XMCD at the L edge. However, a recent study by Jana et al. [40], also using time-resolved X-ray magnetic circular dichroism (XMCD) experiments at the L edges, confirmed the delay between Ni and Fe. Günther et al. [41] (suppl.), Jana et al. [42], and Hofherr et al. [31] (suppl.) also measured the delayed demagnetization behavior of Fe and Ni in these alloys employing EUV T-MOKE. In this thesis, we show how all these different experimental results can be reconciled.

Moreover, the $Fe_{50}Ni_{50}$ alloy was one of the first sample systems in which the theoretically proposed optical intersite spin transfer (OISTR) [43] was experimentally demonstrated by Hofherr

et al. [31]. OISTR is the fastest mechanism that redistributes spins between two or more sublattices in a multi-component alloy [12, 30, 44]. Spin-preserving optical transitions change the magnetization in each subsystem while leaving the total magnetization unchanged. The results of this thesis call the validity of the study by Hofherr et al. into question, since we measured the same sample system using the same magneto-optical technique and found contradictory dynamics. However, with our new approach to reconstruct the full dielectric tensor, we can provide experimental evidence for optical intersite spin transfer in two FeNi alloys and do a quantitative comparison with TDDFT. This also allows us to compare the strength of the spin transfer between $Fe_{50}Ni_{50}$, $Fe_{19}Ni_{81}$ and pure Ni. These findings are directly related to the observed delayed behavior of Ni relative to Fe, which enables us to trace the microscopic origin of this controversial experimental observation and fully explain the observed dynamics.

In summary, this thesis addresses the following research questions:

- How can we interpret the measurement signal in EUV T-MOKE?
- What is the microscopic origin of the controversially discussed delayed demagnetization of Fe and Ni in FeNi alloys?
- Does (strong) optical intersite spin transfer exist in FeNi alloys?

Chapter 2 provides a short introduction into the field of ultrafast magnetism focusing on the optical intersite spin transfer. Chapter 3 presents the fundamental concepts of magneto-optical spectroscopy, the advantages of using extreme ultraviolet light and the basics of our specific magneto-optical technique, the EUV transverse magneto-optical Kerr effect. Particularly noteworthy are sections 3.4 and 3.5 in which we explain our new understanding of the connection between the EUV T-MOKE measurement signal and the dielectric tensor and how we can extract the dielectric tensor with our new analysis from angle-resolved EUV T-MOKE data. In chapter 4, our new setup employing the EUV transverse magneto-optical Kerr effect is described in detail. The data quality is compared to similar setups and the additional options to also measure the s-polarized reflectivity and to modify the incidence angle are introduced. Chapter 5 describes our results of ultrafast spin transfer in two FeNi alloys ($Fe_{50}Ni_{50}$ and $Fe_{19}Ni_{81}$). Our new data analysis to extract the full dielectric tensor is used to identify signatures of the optical intersite spin transfer and make a quantitative comparison with TDDFT. The final chapter 6 concludes with a brief summary and outlook.

2

Ultrafast magnetism

This chapter provides a brief introduction to the field of ultrafast magnetism, and highlights the optical intersite spin transfer (OISTR) as one mechanism that manipulates spins on the ultrafast timescale. For a complete description of the microscopic mechanisms of ultrafast demagnetization, the reader is referred to: Kirilyuk et al. (2010) [11], Bigot et al. (2013) [45] and Fähnle et al. (2011) [46]. A current overview of the field and recent experimental and theoretical results are given by Jeppson et al. (2021) [47], Lloyd-Hughes et al. (2021) [9] and Kimel et al. (2022) [14].

2.1. Ultrafast demagnetization

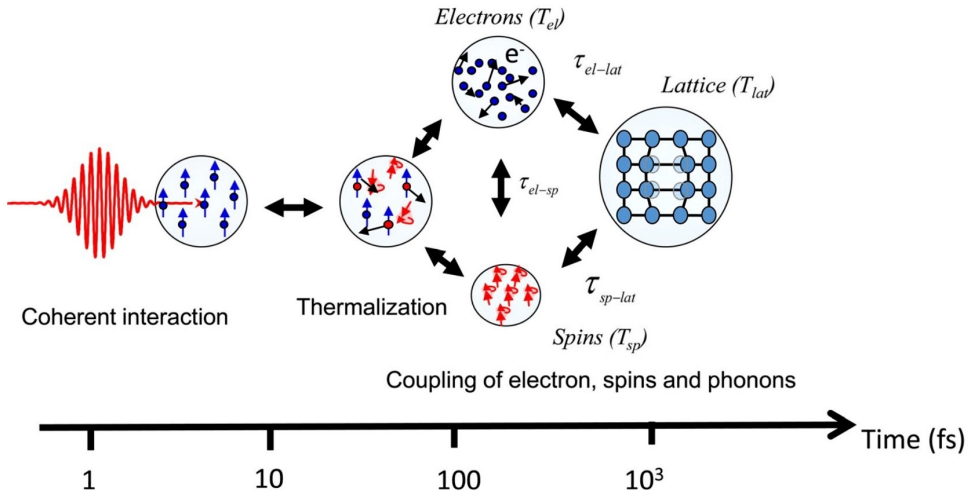

Figure 2.1.: A femtosecond laser pulse coherently interacts with the electrons and spins of a ferromagnet resulting in a non-equilibrium of excited electrons. These excited electrons and spins thermalize via secondary incoherent processes leading to the demagnetization of the ferromagnet. Reprinted from Ref. [48], with permission of AIP Publishing. Copyright (2016) AIP Publishing.

The field of ultrafast magnetism aims to understand the "fundamental" timescales on which the magnetic order in a material can be manipulated. When a femtosecond laser pulse hits a magnetic sample, the electromagnetic field first interacts coherently with the electrons (cf.

figure 2.1) and creates excited non-thermalized electrons. In a second step, this non-equilibrium state of excited charges and spins relaxes back to a hot equilibrium distribution via phonons (Elliot-Yafet electron phonon scattering [16,17,49]), electron-electron scattering [15,50], electron-magnon scattering [18, 19, 51, 52] or superdiffusive spin currents [20, 21, 53]. Thus, we can think of ultrafast demagnetization as a two-step process, where the reduction of the magnetic moment mainly takes place via the secondary processes [54]. The different processes occur on different timescales as electron scattering can be as fast as 10 fs while the electron phonon thermalization time is usually around 1 ps [45].

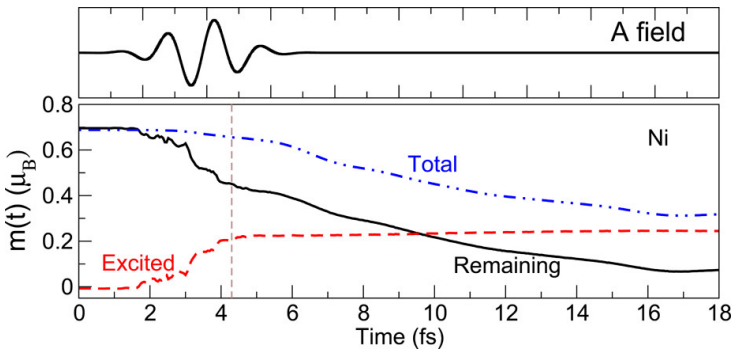

Figure 2.2.: The total magnetic moment of nickel (blue) calculated with TDDFT is shown after the excitation with an ultrashort laser pulse (2.2 fs FWHM). The magnetic moment of the excited electrons (red) increases in the first 5 fs approximately at about the same rate as the moment of the remaining electron decreases, resulting in a constant total moment. Then, spin flips of the remaining electrons lead to the demagnetization and the loss of the total moment. Reprinted with permission from Ref. [55]. Copyright (2015) American Chemical Society.

Krieger et al. [55] use time-dependent density-functional theory (TDDFT) to investigate the ultrafast demagnetization in ferromagnetic nickel at early timescales. Since they use a very short laser pulse of only 2.2 fs FWHM to excite the system, it becomes clear that spin flips and other secondary processes happen after the laser excitation. This is depicted in figure 2.2, where the total magnetic moment starts to significantly change after the laser pulse is already gone. TDDFT can distinguish between the moment of the optically excited electrons and the electrons that are not excited and remain in their original state. The main contribution to the demagnetization comes from the "remaining electrons" performing spin-orbit induced spin flips.

The remaining localized electrons are more prone to perform spin flips due to the spin-orbit term in the Hamiltonian $\frac{1}{4c^2}\vec{\sigma}\cdot(\nabla v_s(\boldsymbol{r},t)\times i\nabla)$, which is proportional to the local potential [43]. As the gradient term is large for the localized electrons, the spin orbit term is most prominent for these.

In order to understand the excitation pathways in multi-component alloys, it is helpful to have

not only an energy/DOS picture of the excited electrons, but also a spatial picture as shown in figure 2.3. The excited electrons are more delocalized in contrast to the remaining electrons, which are localized close to the nuclei in the muffin tin potential. Thus, TDDFT can distinguish between the delocalized excited electrons in the interstitial region and the remaining localized electrons of which the moment is shown in figure 2.2. The moment of the remaining electrons was calculated by integrating the magnetization density over a small muffin tin sphere around each nucleus [55].

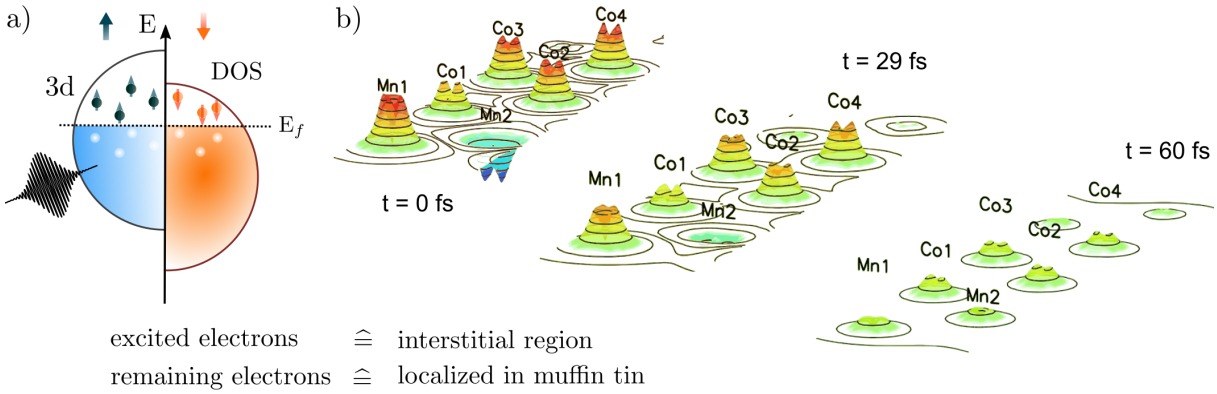

Figure 2.3.: a) Electrons are optically excited from occupied 3d states to empty states above the Fermi level. b) Exemplary magnetization density for a Mn/Co bilayer for three time steps after the excitation with a 13 fs, 1.55 eV pump pulse calculated with TDDFT. Excited electrons are delocalized while the remaining electrons are localized close to the nuclei in their muffin tin potential. Adapted and reprinted from Ref. [43], used here in accordance with ACS AuthorChoice License. Copyright (2018) American Chemical Society.

2.2. Optical intersite spin transfer

Regarding fundamental physics as well as applications, the question of how fast spins can be manipulated with light is extremely interesting. Recently, the *optical intersite spin transfer* (OISTR) was proposed theoretically by Dewhurst et al. [43] and experimentally demonstrated via various techniques and in different sample systems:

- Siegrist et al. in Ni/Pt multilayers using attosecond EUV MCD [12]
- Hofherr et al. in a $Fe_{50}Ni_{50}$ alloy employing EUV T-MOKE [31]
- Tendgin et al. in a Co_2MnGe alloy using EUV T-MOKE [30]
- Willems et al. in a CoPt alloy with helicity dependent EUV absorption [44]
- Chen et al. in Co/Cu(001) measured via second harmonic generation at interfaces [56]
- Steil et al. in a NiMnSb alloy using visible MOKE [57]

- Golias et al. in antiferromagnetic Mn in Co/Mn multilayers with time-resolved resonant magnetic x-ray reflection (RMXR) [58]
- Liu et al. in Gd/Fe bilayer (OISTR between surface and bulk states) using spin-resolved photoemission [59]
- Häuser et al. in $Fe_{20}Ni_{80}$/Au employing EUV T-MOKE [60]
- Ryan et al. in a Co_2MnGa alloy using EUV T-MOKE [32].

The optical intersite spin transfer describes the excitation of spins from one atomic species to another, e.g., in an alloy or multilayer [43]. The total magnetic moment does not change, but the magnetic moment in the respective subsystems changes. In a spatial picture, the local spin moments change and spin is transferred to a neighboring atomic site. The number of states below and above the Fermi level in combination with the transition probabilities in the different subsystems determines whether OISTR is dominant or not.

What makes OISTR so special is its speed: OISTR is fast. The timescale at which OISTR happens is only determined by the length of the optical laser pulse and, thus, allows for very fast manipulation of spins with light. Siegrist et al. [12] found OISTR signatures in Ni/Pt multilayers using an attosecond probe and 4 fs pump pulses showing coherent dynamics on the sub-5 fs timescale. With OISTR, it is possible to control spins faster than the intrinsic spin orbit time (around 50 fs in 3d ferromagnets [61]). Such fast OISTR processes during the optical excitation contrast sharply with secondary scattering processes (spin-orbit mediated spin flips, e-e scattering, e-phonon scattering, e-magnons, spin currents), which happen on a timescale > a few 10 fs.

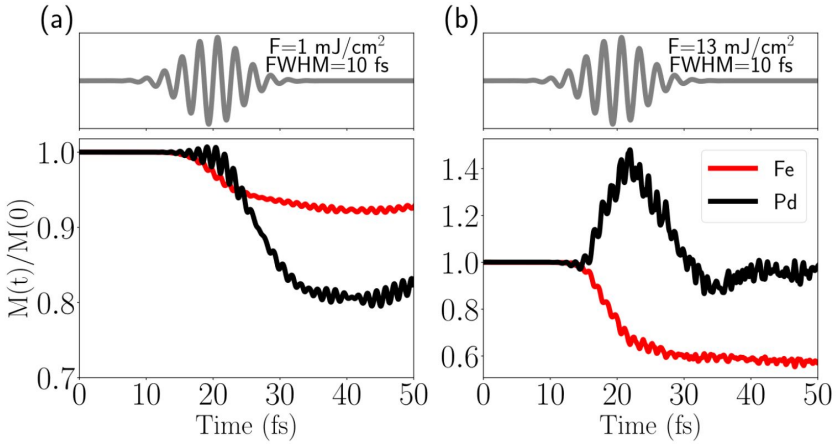

Figure 2.4.: Magnetic moment of Fe (red) and Pd (black) in FePd after the excitation with a 10 fs (FWHM), 800 nm laser pulse. The fluence of the laser pulse drastically influences the dynamics and is 1 $^{mJ}/_{cm^2}$ for a) and 13 $^{mJ}/_{cm^2}$ for b). Reprinted from Ref. [62], used here in accordance with *Creative Commons Attribution 4.0 International* (CC BY 4.0).

To be able to experimentally observe OISTR, the strong pulse dependence of this effect is important [62]. Elhanoty et al. [62] calculate the magnetic moment in FePd for two different pump fluences of 1 $^{mJ}/_{cm^2}$ and 13 $^{mJ}/_{cm^2}$ (cf. fig. 2.4) with TDDFT. In both cases, an optical intersite spin transfer takes place and occupied minority spins of Pd are transferred to the unoccupied minority states of Fe. This corresponds to an increase in the Pd moment and a decrease in the Fe moment as depicted for the larger fluence in figure 2.4 b). For the low fluence in figure 2.4 a) the dynamics look totally different because OISTR is less strong and, thus, less important. The magnetic moment doesn't change much while the pulse is present. For times greater than 20 fs, spin-orbit induced spin flips dominate the dynamics.

OISTR signatures in FeNi alloys

This thesis deals with the optical intersite spin transfer in FeNi alloys, which is schematically shown in figure 2.5. TDDFT calculations predict an increase in the magnetic moment of nickel as minority spins are transferred from nickel to iron. The spin magnetic moment of Fe reduces from its ground state value of 2.89 μ_B to 2.38 μ_B. For nickel the moment first increases from 0.67 μ_B to 0.69 μ_B due to OISTR and then decreases by spin-orbit mediated spin flips to 0.57 μ_B.

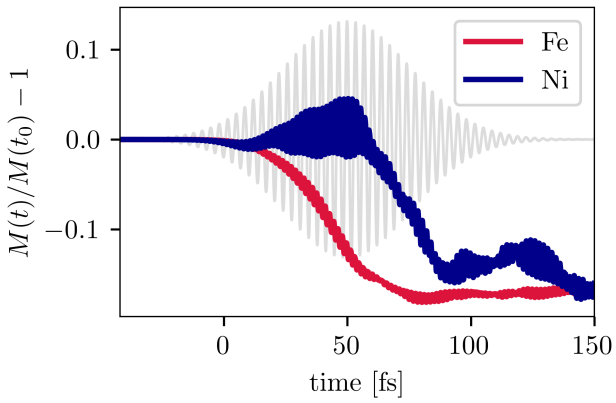

Figure 2.5.: Magnetic moment of Fe (red) and Ni (blue) in $Fe_{50}Ni_{50}$ after the excitation with a 47 fs (FWHM), 1030 nm laser pulse (18 $^{mJ}/_{cm^2}$). The transfer of minority nickel spins to iron leads to an increase in the magnetic moment of nickel. Data provided by Sangeeta Sharma.

Hofherr et al. [31] investigated the optical intersite spin transfer in a $Fe_{50}Ni_{50}$ alloy in a joint experimental EUV T-MOKE and theoretical TDDFT study. Figure 2.6 illustrates the main results of this paper. $Fe_{50}Ni_{50}$ has a large amount of empty minority states in the projected density of states for iron above the Fermi edge and a large density of minority states for nickel below the Fermi edge. Thus, OISTR transfers spins from minority nickel to minority iron states. Of course, transitions within the subsystem (Ni to Ni and Fe to Fe) also occur, but do not contribute to the OISTR effect. The resulting loss of minority carriers for nickel below the

edge and the increase of minority carriers for iron above the edge are depicted in figure 2.6 b), calculated with TDDFT for the 1.55 eV pump pulse. Experimentally, the OISTR signatures become visible for a photon energy of ~ 64 eV (2 eV below the Ni edge) and 2 eV above the Fe edge as shown in figure 2.6 c). The experimental asymmetry probing states below the Ni edge (blue) shows an ultrafast increase indicating the loss of minority carriers while the experimental asymmetry probing states above the iron edge (green) exhibits a fast decrease. The validity of these experimental observations is discussed in detail in section 5.1, where we present results on two FeNi alloys, also measured with EUV T-MOKE, but for multiple incidence angles.

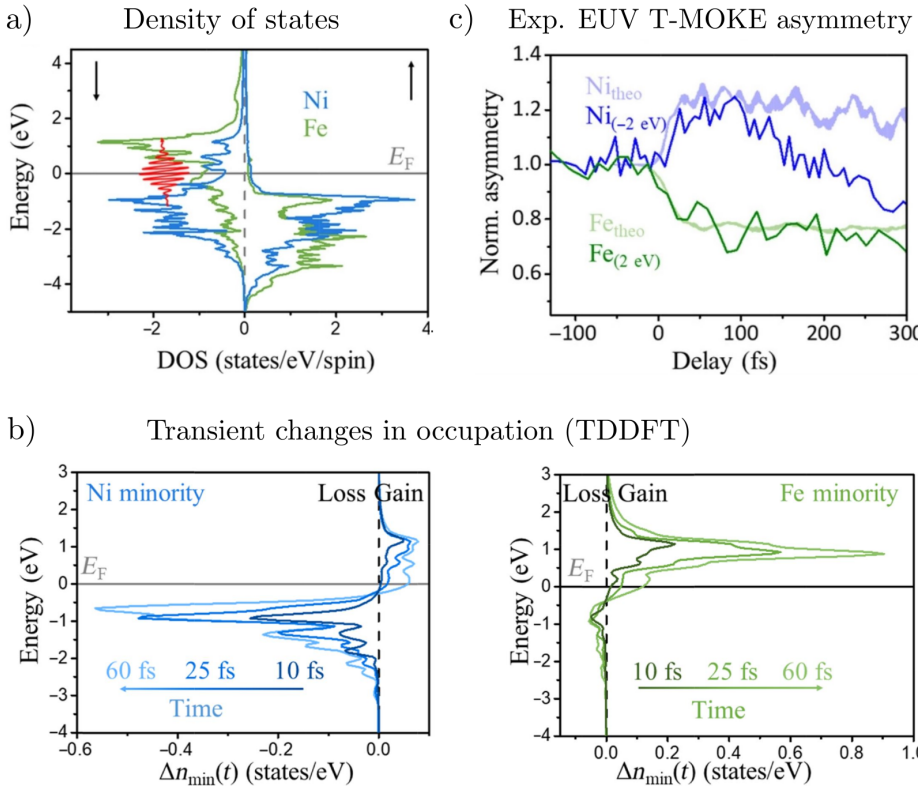

Figure 2.6.: a) Projected density of states for iron and nickel-like states in $Fe_{50}Ni_{50}$ alloy calculated with TDDFT. For iron, there is a large number of unoccupied minority states above the Fermi edge while there is a large number of occupied nickel minority states below E_f. This leads to a strong optical intersite spin transfer from minority nickel to minority iron states – cf. b) where the transient changes of the occupation for Ni and Fe are plotted. c) Experimental EUV T-MOKE asymmetry for a photon energy of 64 eV (2 eV below the Ni edge showing a fast increase in the asymmetry) and 2 eV above the Fe edge, where a fast decrease of the asymmetry is observed. Adapted and reprinted from Ref. [31], used here in accordance with the *Creative Commons Attribution NonCommercial License 4.0* (CC BY-NC 4.0).

3

Transverse magneto-optical Kerr effect with extreme ultraviolet light

To investigate and understand ultrafast magnetism, powerful experimental techniques operating at the ultrafast timescale are indispensable. The fundamental concepts for magneto-optical spectroscopy in general and for the transverse magneto-optical Kerr effect with extreme ultraviolet light (EUV T-MOKE) in particular are presented in this chapter.

The first focus is on the propagation of light in a magnetic medium and a microscopic view on the dielectric tensor. Then, the advantages of extreme ultraviolet light in magneto-optical spectroscopy and its probing window are discussed. The subsequent section focuses on the transverse magneto-optical Kerr effect with EUV light as this is the main experimental technique used in this thesis.

The final section is a detailed description of the new fit routine to extract the dielectric tensor from angle-resolved EUV T-MOKE data. The new analysis yields a massive improvement for the interpretation of EUV T-MOKE data and was developed within the scope of this thesis together with Henrike Probst and Matthijs Jansen. This approach is also described in our publication

> H. Probst, C. Möller, M. Schumacher, et al. Unraveling femtosecond spin and charge dynamics with EUV T-MOKE spectroscopy. `arXiv:2306.02783 [cond-mat.mtrl-sci]`, 2023

where the magnetic as well as the non-magnetic response of ferromagnetic nickel after the excitation with an ultrashort laser pulse is investigated.

3.1. Light in magnetic matter

Propagation of light in a magnetic medium can be described by the four Maxwell equations (in Gaussian units) [64, p. 330]:

$$\begin{aligned}
\nabla \cdot \boldsymbol{D} &= 4\pi\rho \\
\nabla \cdot \boldsymbol{B} &= 0 \\
\nabla \times \boldsymbol{E} &= -\frac{1}{c}\frac{\partial \boldsymbol{B}}{\partial t} \\
\nabla \times \boldsymbol{H} &= \frac{1}{c}\frac{\partial \boldsymbol{D}}{\partial t} + \frac{4\pi}{c}\boldsymbol{J},
\end{aligned}$$

where ρ is the density of external charges introduced into the medium, $\boldsymbol{J}$ is the external current present in the medium, $\boldsymbol{B}$ is the magnetic field, $\boldsymbol{E}$ is the electric field, $\boldsymbol{D}$ is the displacement field and $\boldsymbol{H}$ is the magnetizing field.

In addition, we have the following three material dependent equations which relate the displacement field $\boldsymbol{D}$ and the magnetizing field $\boldsymbol{H}$ to the averaged microscopic fields $\boldsymbol{E}$ and $\boldsymbol{B}$:

$$\boldsymbol{D} = \epsilon_0 \hat{\epsilon} \boldsymbol{E} \tag{3.1}$$

$$\boldsymbol{B} = \mu_0 \hat{\mu} \boldsymbol{H} \tag{3.2}$$

$$\boldsymbol{J} = \hat{\sigma} \cdot \boldsymbol{E}, \tag{3.3}$$

where $\hat{\epsilon}$ denotes the dielectric tensor, $\hat{\mu}$ the magnetic permeability and $\hat{\sigma}$ the electric conductivity [64]. The dielectric tensor $\hat{\epsilon}$ connects the induced polarization in the x, y and z directions to the driving field.

The following description follows Beaurepaire et al. [65], Oppeneer [10], Pershan et al. [66] and Erskine et al. [67].

The displacement field $\boldsymbol{D}(\boldsymbol{r}, t)$ is, in general, space and time dependent, and the electric wave field for the general case of an inhomogeneous medium can be written as

$$\boldsymbol{E}(\boldsymbol{r}, t) = \int \mathrm{d}\boldsymbol{k} \int \mathrm{d}\omega \boldsymbol{E}(\boldsymbol{r}, \omega) e^{i\boldsymbol{k}\cdot\boldsymbol{r} - i\omega t}, \tag{3.4}$$

where $\boldsymbol{k}$ is the wave vector and ω the angular frequency. Note that a different sign convention in front of ω in equation (3.4) would lead to different expressions for the later defined magneto-optical functions. The typical magnetic materials have lattice constants around 2 - 10 $\mathring{A}$ and appear reasonably homogeneous for visible light (400 to 800 nm) such that we can neglect the spatial dependence. Thus, it is reasonable to only consider the frequency dependence of the dielectric tensor $\hat{\epsilon}$, the conductivity tensor $\hat{\sigma}$ and the magnetic permeability tensor $\hat{\mu}$.

We focus on optical phenomena and, hence, the frequency dependence of the magnetic permeability tensor is usually neglected such that $\hat{\mu}(\omega) = \mu_0 \cdot \hat{1}$ holds ($\hat{1}$ is the identity matrix) [68].

Nonetheless, we can describe the response of ferromagnetic materials; the missing frequency dependence $\hat{\mu}(\omega)$ only means that the electric response dominates the propagation of the electromagnetic wave.

The shape of the dielectric tensor reflects the symmetry of the crystal structure of the solid. If we assume a cubic crystal structure and choose a magnetization $\boldsymbol{M}||[001]$ in z direction, the dielectric tensor $\hat{\epsilon}$ has the following form:

$$\hat{\epsilon}(\boldsymbol{M},\omega) = \begin{pmatrix} \epsilon_{xx} & \epsilon_{xy} & 0 \\ -\epsilon_{xy} & \epsilon_{xx} & 0 \\ 0 & 0 & \epsilon_{zz} \end{pmatrix} \tag{3.5}$$

The off-diagonal matrix element ϵ_{xy} is often called the magneto-optical constant. Both the diagonal and the off-diagonal elements are complex numbers. The diagonal components of the dielectric tensor are an even function of $\boldsymbol{M}$, so they describe in first order the normal optical properties of the material. To the contrary, the off-diagonal components are odd in $\boldsymbol{M}$ and, thus, proportional to the magnetization $\boldsymbol{M}$. This follows directly from the Onsager relations $\epsilon_{ij}(\boldsymbol{M},\omega) = \epsilon_{ji}(-\boldsymbol{M},\omega) = -\epsilon_{ji}(\boldsymbol{M},\omega)$ [69].

One can directly relate the diagonal elements to the square of the complex refractive index $\epsilon_{xx} = n_0^2 = (1-\delta+i\beta)^2$. In the extreme ultraviolet region, the complex refractive index is close to unity while the off-diagonal element ϵ_{xy} is in the order of 10^{-2} to 10^{-3} [70, 71]. Thus, the off-diagonal elements are usually very small compared to the diagonal elements, i.e., $|\epsilon_{xy}| \ll |\epsilon_{xx}|$.

It is worth considering the symmetry of the dielectric tensor for the above specified crystal in the non-magnetic case, i.e., above the Curie temperature T_C. Then, all components of the dielectric tensor are equal, and $\hat{\epsilon}(\omega) = \epsilon \cdot \hat{1}$. Thus, the magnetic ordering reduces the symmetry compared to the non-magnetic case. This reduction in symmetry only occurs when spin-orbit coupling is present, so many magneto-optical effects exist only because magnetic order and spin-orbit coupling are present at the same time [10, 72]. Beaurepaire [65] summarizes this fact in the following way:

> "The magnitude of the off-diagonal components of the conductivity tensor depends on the magnitude of the magnetization and the strength of spin-orbit coupling."

To facilitate a microscopic understanding of the dielectric tensor and the resulting magneto-optical effects, the conductivity tensor $\hat{\sigma}$ shall be considered in more detail. It is directly related to the dielectric tensor via

$$\hat{\epsilon} = \hat{1} + \frac{4\pi i}{\omega}\hat{\sigma}(\omega). \tag{3.6}$$

The imaginary part of off-diagonal conductivity tensor element $\mathrm{Im}(\sigma_{xy}) = -\frac{\omega}{4\pi}\mathrm{Re}(\epsilon_{xy})$ is related to the real part of the off-diagonal dielectric tensor element. The expression for the off-diagonal

conductivity tensor can be obtained from Fermis golden rule or the Kubo formalism [73, 74], which, for $\omega > 0$, reads

$$\mathrm{Re}(\epsilon_{xy}) \propto \mathrm{Im}(\sigma_{xy}) \propto \sum_{i,f} f(E_i)(1 - f(E_f)) \cdot \left(|\langle i|p_-|f\rangle|^2 - |\langle i|p_+|f\rangle|^2 \right) \cdot \delta(E_f - E_i - \hbar\omega), \quad (3.7)$$

where $p_\pm = p_x \pm p_y$ are the linear momentum operators, ω is the light frequency and the summation takes all initial $|i\rangle$ and $|f\rangle$ final states into account [75]. Here, $(|\langle i|p_-|f\rangle|^2 - |\langle i|p_+|f\rangle|^2)$ reflects the difference in absorption for left and right circular polarized light. For the case of a bulk paramagnet, these transition probabilities are equal and, thus, the difference between them is zero, and magneto-optical effects are not present. $f(E_i)$ is the Fermi function and represents the occupation of the initial state, whereas $(1 - f(E_f))$ represents the amount of empty final states. Ω is the total volume and the δ-function ensures energy conservation.

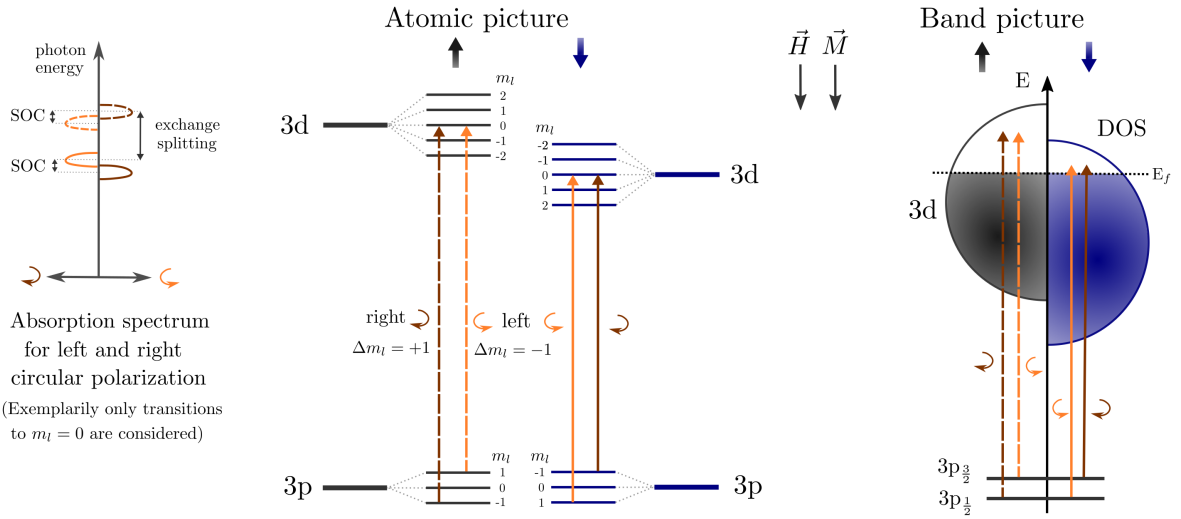

Figure 3.1.: Absorption spectrum for left and right circular polarization and atomic and band picture for the transitions between the 3p core levels and the 3d bands. For the sake of clarity only transitions to the $m_l = 0$ level of the 3d states are drawn and taken into account for the schematic absorption spectrum. The spin-orbit splitting of the initial states and the exchange split 3d bands lead to the absorption "peaks" located at different photon energies for right and left circular polarization. Inspired by Ref. [74].

The optical transitions shown in figure 3.1 directly reflect the relations in equation (3.7) and the different absorption for left and right circular polarized light. The dipole selection rules allow only

$$\Delta j = 0, \pm 1 \qquad \Delta s = 0 \qquad \Delta l = \pm 1 \qquad \Delta m_l = \begin{cases} -1 & \text{left circular polarization} \\ +1 & \text{right circular polarization} \end{cases}$$

for circularly polarized light [76]. At the M edge, the transitions occur from $3p$ states $|l, m_l\rangle$ into $3d$ states with $|\, l+1, m_l \pm 1\rangle$ and are exemplarily shown in the atomic picture in figure 3.1.

In the end, the spin-orbit split initial states, the exchange splitting in the final states and the selection rules for dipole transitions with circularly polarized light are all relevant to get different absorption spectra for left and right circular polarized light. The spin-orbit interaction leads to spin-split $3p$ core levels, and the exchange interaction of the order of 1 eV leads to spin-splitting of the d-bands.
A simple two-step picture gives an intuitive view and distinguishes between step one – the resonant excitation of a spin-polarized electron via absorption of a circularly polarized photon – and step two, the excited electrons "finding" an unoccupied state above the Fermi level [77]. If a circularly polarized photon is absorbed, the angular momentum $\pm\hbar$ of the photon has to be conserved and is transferred to the spin of the electron in a spin-orbit split energy level [78]. E.g., for the $3p_{3/2}$ ($j = l + s$) initial state and photons with a right circular polarization, more spin-up than spin-down electrons are excited resulting in a spin polarization of the excited electrons. Note that this spin polarization of the excited electrons is reversed for the $3p_{1/2}$ state due to opposite spin orbit coupling $j = l - s$ [76, p. 12]. In the second step, the amount of available unoccupied states in the $3d$ bands differs for spin up and spin down electrons in a ferromagnetic material [79, p. 25].

The diagonal elements of the conductivity tensor (and thereby the dielectric tensor) reflect the optical absorption, which is independent of the magnetization of the material. The imaginary part of the diagonal dielectric tensor element can be expressed as

$$\mathrm{Im}(\epsilon_{xx}) \propto \mathrm{Re}(\sigma_{xx}) \propto \sum_{i,f} f(E_i)(1 - f(E_f)) \cdot \left(|\langle i|p_-|f\rangle|^2 + |\langle i|p_+|f\rangle|^2 \right) \cdot \delta(E_f - E_i - \hbar\omega),$$

and contains the sum $\langle i|p_-|f\rangle|^2 + |\langle i|p_+|f\rangle|^2$ for left and right circular polarized light.

3.2. Element sensitivity using extreme ultraviolet light

In magneto-optical spectroscopy, the use of extreme ultraviolet (EUV) or X-ray light instead of visible light has several advantages that will be illustrated in this section. The extreme ultraviolet region includes photon energies between 30 and 250 eV (cf. figure 3.2) while soft X-rays have 250 eV to several keV [80]. These high photon energies cover the absorption edges of most elements (cf. table 3.1). Thus, almost all materials exhibit high absorption in these spectral regions and are only transparent for lower photon energies, e.g., in the visible region. High absorption can be an experimental challenge for magnetic spectroscopy techniques in transmission, but, the use of thin membranes and thin magnetic layers overcomes this problem. As listed in table 3.1, extreme ultraviolet light can probe the M edges (3p to 3d) of many magnetic materials, e.g., at 54 eV for iron, 58.9 eV for cobalt, and 66.2 eV for nickel [81]. The L edges (2p to 3d) of these materials can be probed using soft X-rays with photon energies between 700 eV and 900 eV.

Spectroscopy in the EUV and X-ray spectral range has the enormous advantage of providing ele-

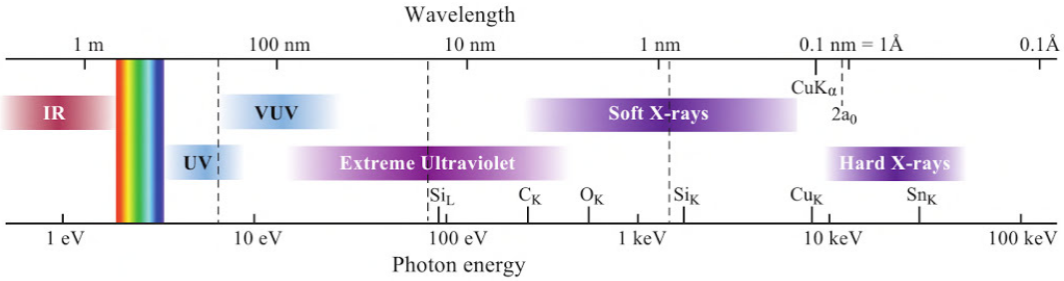

Figure 3.2.: Electromagnetic spectrum spanning from infrared to hard X-rays. In contrast to the visible light around 400 - 800 nm, the extreme ultraviolet and X-ray region describes photons with significantly smaller wavelengths and, thus, higher photon energies between 30 eV and 100 keV. Reprinted from Ref. [80] with permission of Cambridge University Press through PLSclear. Copyright (1999) Cambridge University Press.

	Absorption Edges				Attenuation Lengths		
element	M_2 [eV]	M_3 [eV]	L_2 [eV]	L_3 [eV]	100 eV [nm]	1 keV [nm]	10 keV [nm]
Fe	54		720	707	22	140	7400
Co	59.9	58.9	793	778	17	116	6200
Ni	68.0	66.2	870	853	16	111	5400

Table 3.1.: The M absorption edges of the 3d ferromagnets are in the extreme ultraviolet while the L edges are in the soft X-ray region. The spin orbit splitting with up to 17 eV for nickel is significantly larger for the 2p states at the L edge compared to the 3p core levels at the M edge (1.8 eV for Ni). The absorption in the extreme ultraviolet is quite high resulting in small attenuation lengths shown on the right. Data taken from [81] and [82].

ment sensitivity, as the absorption edges for different elements are separated in energy. Element sensitivity allows to distinguish between the measurement signal coming from element A and element B which are components in an alloy or multilayer. Figure 3.3 illustrates the absorption of the alloy $Fe_{19}Ni_{81}$ for different photon energies. The different absorption edges (M, L and K) are the "steps" in the absorption spectrum and can be associated with the position of the different core levels shown in fig. 3.3 b). The absorption increases abruptly when the photon energy is larger than the energetic distance between the core level and the Fermi edge. Core levels are unique for each element and are at different binding energies for different elements. This can be seen in figure 3.3 a), where the different contributions of the two elements nickel and iron correspond to the two steps at each absorption edge.

Techniques using photon energies around the M or L absorption edge follow the same physics and probe the same d-states. The only difference is that for the L edge the two spin-orbit split core levels are further apart such that transitions from one or the other core level are clearly

separated in energy in the measurement signal. This allows for the application of the XMCD sum rules at L edges in order to get the spin and orbital moments [83], which is not possible at the M edge because of the energetic overlap of transitions from both core levels. Sharma et al [84] pointed out that these sum rules have limitations in extracting the "real" spin moment for ultrafast optical excitations with high pump fluences. The XMCD sum rules are derived for an atomic picture and assume that the electrons are excited into d-orbitals. Since electrons are also excited into states of non-d character the extracted demagnetization amplitude can have errors up to 50 % [84].

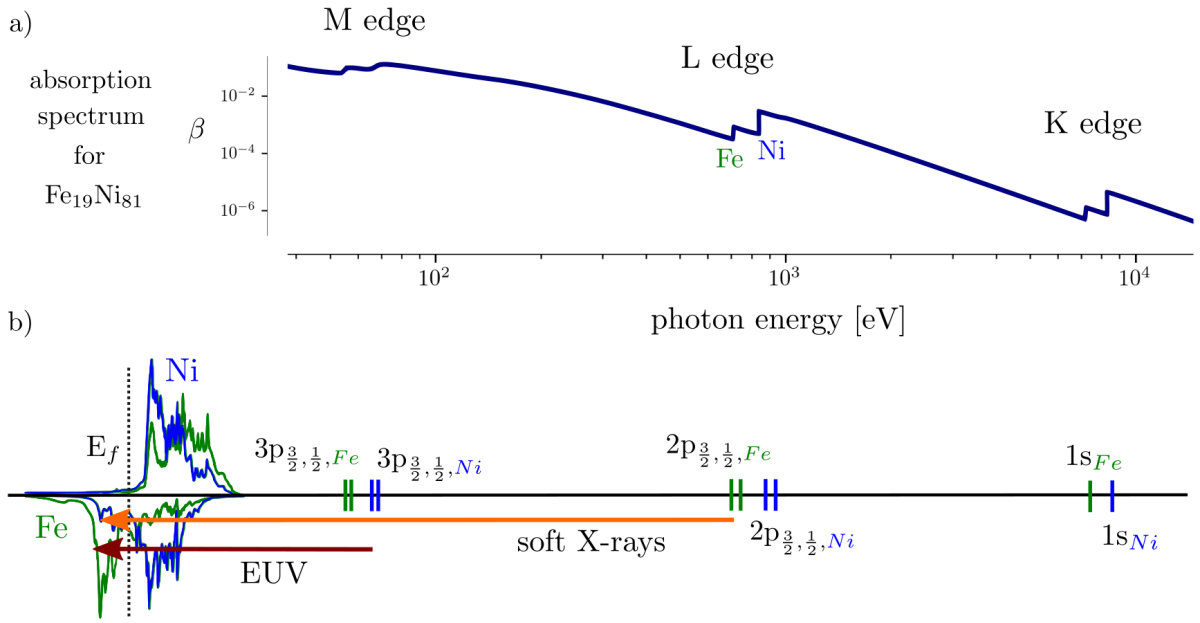

Figure 3.3.: a) Absorption spectrum of $Fe_{19}Ni_{81}$ for photon energies between 40 and 10000 eV (data for β taken from CXRO [81]). The M, L, and K edges are clearly visible as steps in the absorption curve. The two-step behavior at each edge is caused by the distinct iron and nickel contributions. b) Core levels and optical transitions for the M, L and K edge. For the M and L edge, the 3p and 2p states are spin-orbit split. Also, the separation between the nickel and iron core levels is depicted which is the prerequisite for the element specificity of all EUV and X-ray techniques. Density of states adapted and reprinted from Ref. [31], used here in accordance with the *Creative Commons Attribution NonCommercial License 4.0* (CC BY-NC 4.0).

The influence of the probe photon energy becomes also apparent in the off-diagonal element of the dielectric tensor in equation (3.7). Using visible light, the initial states of the optical transitions are the occupied 3d states and the final states are the 4p states above the Fermi level. Therefore, visible light is usually not element specific because all states involved are close to the Fermi level, where many bands overlap and distinguishing energetically between, e.g., more "iron like" or more "nickel like" d bands is extremely challenging and cannot be done without further modeling.

In the case of extreme ultraviolet light, the initial states are 3p core levels and the final states correspond to the unoccupied 3d states. The 3d bands are exchange split and govern the magnetic properties, allowing to probe the magnetic properties of the sample. The core levels are localized, have no dispersion in k-space and have specific energies for each element. These features make extreme ultraviolet light an element-specific probe [65].

3.3. Photon energy-dependent probing – width of probing window

	Distance btw. 3p states [eV]	Width of $3p_{\frac{1}{2}}$	Width of $3p_{\frac{3}{2}}$ [eV]
Fe	1.1	1.22	0.44
Co	1.4	1.26	0.71
Ni	1.5	1.19	1.19

(a)

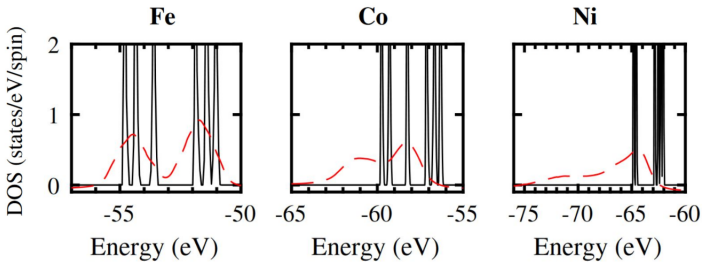

(b)

Figure 3.4.: (a) Spin-orbit coupling constant for the 3d ferromagnets, which corresponds to the energetic splitting of the $3p_{\frac{1}{2}}$ and $3p_{\frac{3}{2}}$ states. In addition, the lifetime-broadened width (FWHM) of the 3p states measured by Nyholm et al. [85] using photoelectron spectroscopy is shown (coupling constants from [86], width of 3p states from [85]). (b) Spin-averaged Kohn-Sham density of states (black) and GW spectral function (red) from TDDFT for the 3p states of Fe, Co and Ni. Reprinted figure with permission from Ref. [87]. Copyright (2019) by the American Physical Society.

Different magneto-optical techniques measure different experimental observables (such as the polarization/intensity of the reflected or transmitted light), which are ultimately related to the off-diagonal dielectric tensor element ϵ_{xy}. In recent years, many studies focused on the transient spin dynamics measured with multiple EUV photon energies to understand the dynamics not only in an element-resolved but in an energy-resolved manner, e.g. [31,36,44,88,89]. Frequently, the measured dynamics are different for different photon energies which provides insights into the population changes of minority and majority spins or band-structure renormalization [90]. For each specific photon energy, the resulting measurement signal is related to the off-diagonal tensor element $\epsilon_{xy}(E)$ for a specific photon energy $E = \hbar\omega$. As can be observed from the off-diagonal tensor element $Re(\epsilon_{xy}(E))$ in equation (3.7), one photon energy does not probe a single final state in the band structure. Instead, all optical transitions that are possible for this photon energy are included in the off-diagonal tensor element.

Considering the size of the spin-orbit coupling and the lifetime broadened width of the initial 3p states in table 3.4a), it becomes clear that the initial states are not infinitely narrow in energy, but span a certain width of energies (around 2 eV). Thus, magneto-optical spectroscopy in the

EUV always probes the spin polarization of many empty 3d states of a certain width on the order of 2 eV, which, in a sense, constitutes the spectral width of the probing window [91].

Figure 3.4b) depicts the density of states for the initial 3p states for Fe, Co and Ni calculated by Sharma et al. [87] with time-dependent density functional theory (TDDFT). To improve the agreement with experimental EUV MCD data, many-body corrections and a fully spin-polarized GW calculation were included, resulting in the spectral function shown in red in figure 3.4b). This spectral function is red-shifted compared to the Kohn-Sham density of states and has a finite

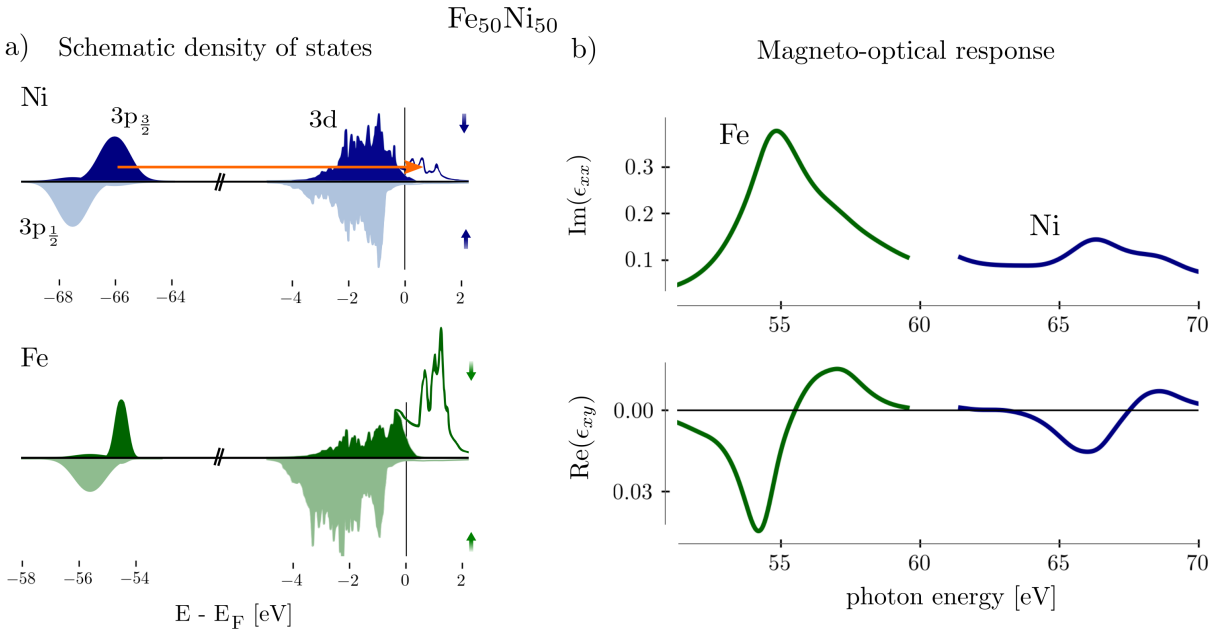

Figure 3.5.: Connection between the spin-resolved density of states and the magneto-optical response of $Fe_{50}Ni_{50}$. a) Element-projected density of states for the 3d states calculated with TDDFT. Only empty final states are relevant for the magneto-optical signal. Thus, mainly optical transitions in the minority channel contribute to the absorption because of the small majority density of states above the Fermi level (E_F). b) Magneto-optical response calculated with TDDFT. The upper graph shows the absorption, i.e., the imaginary part of the diagonal tensor element ϵ_{xx}. The lower graph shows the magneto-optical response, represented here by the real part of the off-diagonal tensor element ϵ_{xy}, which is non-zero due to the imbalance of free minority and majority 3d states. The blue color marks the photon energies around the nickel M edge while the green color shows the response for photon energies around the iron edge. The relatively broad initial 3p states compared to the approx. 2 eV broad energy region, where many empty states above the Fermi level are available, shows again that many different optical transitions contribute to the magneto-optical signal for one photon energy. Projected DOS for 3d states and dielectric tensor calculated by Sangeeta Sharma. The width of the initial 3p states was chosen according to table 3.4a) and [85].

width. In addition, local field effects had to be included to be able to model the experimental measurements. Thus, the analysis in [87] shows that the exact shape and position of the 3p states are very important to describe the magneto-optical response function, or in other words, to adequately obtain $\mathrm{Re}(\epsilon_{xy})$ in TDDFT.

As described before, the magneto-optical response for a specific EUV photon energy involves a certain range of final 3d states, which is given by the shape and width of the initial 3p states. The projected density of states and the magneto-optical response for a $Fe_{50}Ni_{50}$ alloy is exemplarily shown in figure 3.5. The TDDFT calculations were done by S. Sharma. Above the Fermi level, the amount of empty states is high for the minority and low for the majority spins. Thus, mainly optical transitions in the minority channel contribute to the magneto-optical signal. The optical absorption described by the imaginary part of the diagonal tensor element ϵ_{xx} (fig. 3.5 b)) is higher for photon energies around the iron M edge compared to the nickel edge. This is not surprising due to the higher amount of empty states above the Fermi level for iron compared to nickel. The imbalance of free majority and minority states above the Fermi level leads to different absorption for left and right circular polarization. Hence, the off-diagonal tensor element $\mathrm{Re}(\epsilon_{xy})$ is non-zero around each absorption edge. The magneto-optical signal for a specific photon energy is composed of all possible transitions for this photon energy, so that multiple initial and also final states are involved. In the thermal equilibrium case considered here (without an additional optical pump pulse) the magneto-optical signal $\mathrm{Re}(\epsilon_{xy})$ probes only empty 3d states that lie *above* the Fermi level. An optical excitation leads to a non-equilibrium in the occupation, and, thus, also empty states *below* the Fermi level can contribute to the magneto-optical response.

3.4. Understanding the T-MOKE asymmetry

In this section, we focus on one specific magneto-optical technique: the magneto-optical Kerr effect in transversal geometry (T-MOKE) with extreme ultraviolet light. The magneto-optical Kerr effect describes the change in polarization or intensity of light after reflection on a magnetic sample [83, 92]. In the transverse geometry, the magnetization of the sample is orthogonal to the plane of incidence of the incoming and reflected light, cf. figure 3.6 a). In the following, we assume a single vacuum/magnetic material interface and neglect additional capping layers.

According to [93, p. 37], the reflection coefficient for p-polarized light with an incidence angle of θ is

$$\frac{E_{R_0}}{E_{I_0}} = \frac{n_0\cos(\theta) - \sqrt{1-\frac{\sin^2(\theta)}{n_0^2}}}{n_0\cos(\theta) + \sqrt{1-\frac{\sin^2(\theta)}{n_0^2}}} + \frac{\sin(2\theta)}{n_0^2\left(n_0\cos(\theta)+\sqrt{1-\frac{\sin^2(\theta)}{n_0^2}}\right)^2}\cdot\epsilon_{xy} \tag{3.8}$$

$$= R_0 + R_m\cdot\epsilon_{xy}. \tag{3.9}$$

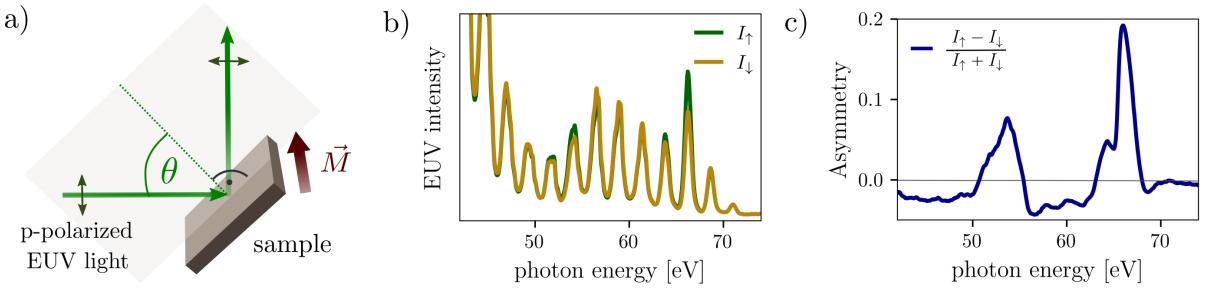

Figure 3.6.: a) Transversal geometry of the magneto-optical Kerr effect: The magnetization of the sample and the plane of incidence are orthogonal to each other. b) The intensity of the reflected EUV light depends on the magnetization direction of the sample. Here, the reflected high harmonic spectrum is shown for a $Fe_{19}Ni_{81}$ alloy. c) Asymmetry for the $Fe_{19}Ni_{81}$ alloy. The normalized difference between the reflected intensities $I_{\uparrow/\downarrow}$ for both magnetic field directions is called asymmetry. The asymmetry is largest around the M absorption edges of iron (54 eV) and nickel (66.2 eV).

Here, R_0 is the Fresnel coefficient for the reflection of p-polarized light and R_m summarizes all terms in front of the off-diagonal tensor element ϵ_{xy}. Note that the refractive index n_0 of the sample is a complex quantity and, thus, R_0 and R_m are also complex (as well as ϵ_{xy}).

The p-polarization of the incident light together with the transverse orientation of the magnetization are the important characteristics in the T-MOKE geometry. For s-polarized light, the reflection coefficient does not depend on the magnetization of the sample [33]

$$R_{0,s} = \frac{\cos(\theta) - n_0\sqrt{1 - \frac{\sin^2(\theta)}{n_0^2}}}{\cos(\theta) + n_0\sqrt{1 - \frac{\sin^2(\theta)}{n_0^2}}}.$$

In the transversal MOKE geometry the intensity of the reflected p-polarized light is different for opposite magnetic field directions. This can be also seen in figure 3.6 b), where the high harmonic spectrum after reflection on a $Fe_{19}Ni_{81}$ alloy is shown. Switching the sign of the magnetic field corresponds to a sign change of the off-diagonal tensor element ϵ_{xy}. The reflected intensity for opposite magnetic field directions $I_\uparrow$ and $I_\downarrow$ can be expressed as

$$\begin{aligned} I_{\uparrow/\downarrow} &= |E_{R_0}(\pm\epsilon_{xy})|^2 \\ &= |R_0 \pm R_m \cdot \epsilon_{xy}|^2 \cdot |E_{I_0}|^2 \\ &= I_0 \cdot \left[|R_0|^2 + |R_m\epsilon_{xy}|^2 \pm 2\,\mathrm{Re}(R_0^* R_m \epsilon_{xy})\right]. \end{aligned} \tag{3.10}$$

In T-MOKE experiments, the asymmetry parameter A is usually extracted from the measured reflected intensities in the following way [29]

$$A = \frac{I_\uparrow - I_\downarrow}{I_\uparrow + I_\downarrow} = \frac{2\,\mathrm{Re}(R_0^* R_m \epsilon_{xy})}{|R_0|^2 + |R_m\epsilon_{xy}|^2}$$

By normalizing to the sum of both reflected intensities, the intensity of the incoming light I_0 vanishes in this equation, which makes the asymmetry less sensitive to intensity fluctuations of the EUV light. The magnetic asymmetry of $Fe_{19}Ni_{81}$ in figure 3.6 c) peaks around the M absorption edges of Fe and Ni.

There is a common approximation to simplify the equation for the asymmetry [93, p. 39], which assumes that the optical term is much larger than the magnetic mixed term, i.e., $|R_0|^2 \gg |R_m \epsilon_{xy}|^2$:

$$A \approx \frac{2\,\mathrm{Re}(R_0^* R_m \epsilon_{xy})}{|R_0|^2} = 2\,\mathrm{Re}\left(\frac{\sin(2\theta)}{n_0^4\cos^2(\theta) - n_0^2 + \sin^2(\theta)} \cdot \epsilon_{xy}\right)$$

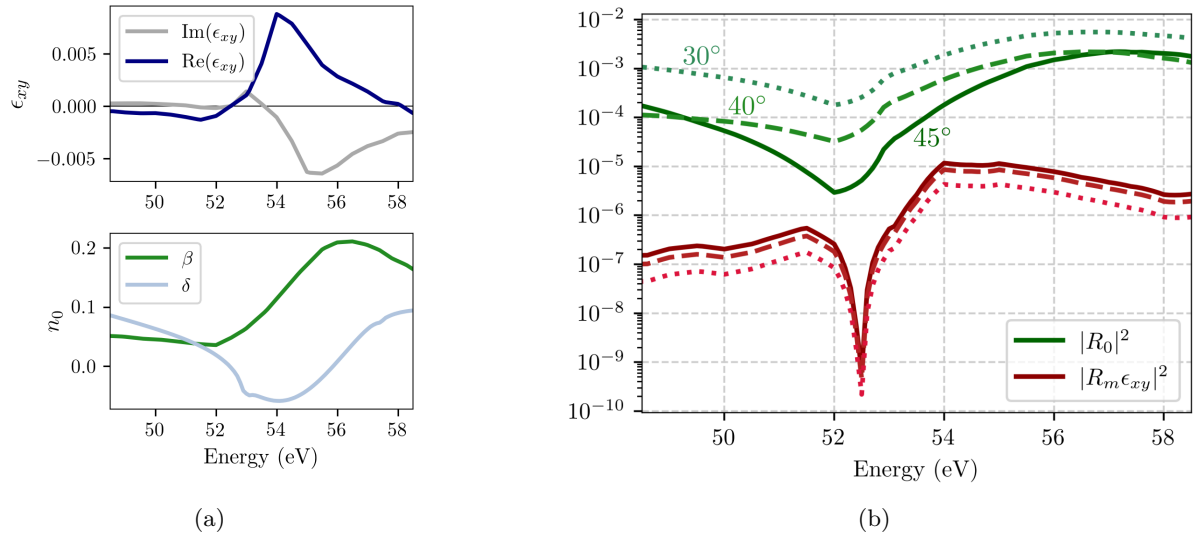

Figure 3.7.: The off-diagonal tensor element ϵ_{xy} and the refractive index n_0 (a) are used to calculate the size of the optical term $|R_0|^2$ and the mixed term $|R_m\epsilon_{xy}|^2$ for iron (b). The approximation $|R_0|^2 \gg |R_m\epsilon_{xy}|^2$ is valid for all shown energies around the M absorption edge, especially for incidence angles far away from the Brewster angle ($\approx$ 45°). However, the approximation is less reliable around the commonly used angle of 45°, because here the reflection for p-polarized light is low and, hence, $|R_0|^2$ is smaller. The off-diagonal tensor element ϵ_{xy} is taken from Höchst et al. [71]. The imaginary part of the complex refractive index β is taken from Willems et al. [87], while the real part is calculated from β via the Kramers-Kronig relation.

To estimate whether the assumption $|R_0|^2 \gg |R_m\epsilon_{xy}|^2$ is valid for the material under investigation, it is possible to calculate the size of the different terms if reasonable values for the complex refractive index n_0 and the off-diagonal tensor element ϵ_{xy} are available. Figure 3.7 b) depicts the size of both terms for ferromagnetic iron for different incidence angles. For the case of iron, the relation $|R_0|^2 \gg |R_m\epsilon_{xy}|^2$ is valid for all energies and all incidence angles. However, for incidence angles near the Brewster angle ($\approx$ 45°), the reflection of p-polarized light $|R_0|^2$ is lower and, therefore, the approximation is less reliable.

In the following, I would like to introduce a new intuitive picture for the relation between the magnetic asymmetry in T-MOKE and the off-diagonal tensor element ϵ_{xy}. The asymmetry can be written as the scalar product of a probe vector $\vec{p} = \binom{p_1}{p_2}$ and the off-diagonal tensor element vector $\vec{\epsilon_{xy}} = \binom{\mathrm{Re}(\epsilon_{xy})}{\mathrm{Im}(\epsilon_{xy})}$ in the complex plane. This disentangles the purely optical terms summarized in the probe vector p_1 and p_2 and the magnetic contribution represented in the real and imaginary part of ϵ_{xy}:

$$
\begin{aligned}
A &\approx \frac{2\,\mathrm{Re}(R_0^* R_m \epsilon_{xy})}{|R_0|^2} \\
&= \underline{\frac{2}{|R_0|^2} \cdot [\mathrm{Re}(R_0^*)\,\mathrm{Re}(R_m) - \mathrm{Im}(R_0^*)\,\mathrm{Im}(R_m)] \cdot \mathrm{Re}(\epsilon_{xy})} \\
&\quad + \underline{\frac{2}{|R_0|^2} \cdot [-\mathrm{Re}(R_0^*)\,\mathrm{Im}(R_m) - \mathrm{Im}(R_0^*)\,\mathrm{Re}(R_m)] \cdot \mathrm{Im}(\epsilon_{xy})} \\
&= \underline{\mathrm{p_1}} \cdot \mathrm{Re}(\epsilon_{xy}) + \underline{\mathrm{p_2}} \cdot \mathrm{Im}(\epsilon_{xy}) \\
&= \begin{pmatrix} p_1 \\ p_2 \end{pmatrix} \cdot \begin{pmatrix} \mathrm{Re}(\epsilon_{xy}) \\ \mathrm{Im}(\epsilon_{xy}) \end{pmatrix}
\end{aligned}
$$

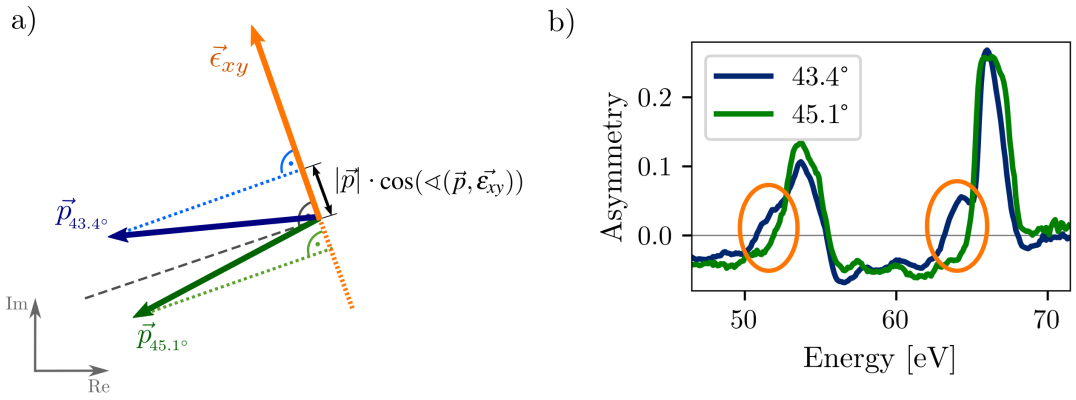

Figure 3.8.: a) The off-diagonal tensor element for one photon energy and two probe vectors are shown schematically. The asymmetry is the scalar product of the $\vec{\epsilon}_{xy}$ and $\vec{p}$ vector, so the length of $|\vec{\epsilon}_{xy}|$ times the projection of $\vec{p}$ on $\vec{\epsilon}_{xy}$. Thus, the relative orientation between both vectors is important and this changes when the incidence angle in the T-MOKE experiment is varied. The $\vec{p}_{43.4°}$ vector has an angle smaller than 90° to the $\vec{\epsilon}_{xy}$ vector, which results in a positive value for the asymmetry. In contrast, the angle $\sphericalangle(\vec{p}_{45.1°}, \vec{\epsilon}_{xy})$ is larger than 90° resulting in a negative value for the asymmetry. b) Experimental asymmetries for $Fe_{19}Ni_{81}$ for two incidence angles. The orange regions highlight energies where the asymmetry is positive for one incidence angle and negative for the other.

The probe vector $\vec{p} = \binom{p_1}{p_2}$ contains the complex numbers R_0 and R_m, which only depend on the incidence angle θ and the refractive index n_0 (see equation (3.9)). Thus, changing the incidence angle in a T-MOKE experiment results in a different orientation of the probe vector $\vec{p}$ in the complex plane. Moreover, the relative orientation of this probe vector $\vec{p}$ to the off-diagonal

tensor element $\vec{\epsilon}_{xy}$ determines the value of the measured asymmetry. Exemplarily, this is shown in figure 3.8 a) for two different incidence angles resulting in different orientations of the $\vec{p}$ vector. The T-MOKE asymmetry is the scalar product of both vectors

$$A = \vec{p} \cdot \vec{\epsilon}_{xy} = |\vec{p}| \cdot |\vec{\epsilon}_{xy}| \cdot \cos(\sphericalangle(\vec{p}, \vec{\epsilon}_{xy})),$$

such that the length of the off-diagonal tensor element $|\vec{\epsilon}_{xy}|$ is important as well as the projection of the probe vector on the $\vec{\epsilon}_{xy}$ vector. If the angle between both vectors, $\sphericalangle(\vec{p}, \vec{\epsilon}_{xy})$, is smaller than 90°, the asymmetry value is positive; for angles larger than 90°, the asymmetry value is negative. This explains the sign changes observed in the experimental asymmetries for $Fe_{19}Ni_{81}$ shown in figure 3.8 b). A zero-crossing of the magnetic asymmetry occurs when the off-diagonal tensor element $\vec{\epsilon}_{xy}$ and the probe vector $\vec{p}$ are orthogonal to each other in the complex plane.

3.5. Novel fit routine to obtain the off-diagonal tensor element from T-MOKE data

In the previous section, it has been shown that the probe vector $\vec{p}$ and, hence, the asymmetry change when the incidence angle is varied in a T-MOKE experiment. The magnetic properties and the off-diagonal tensor element ϵ_{xy} are always the same for a given material and do not depend on the experimental geometry. Thus, when measuring multiple angles of incidence, we gather information on the different probe vectors $\vec{p}$ and are then able to extract the off-diagonal tensor element ϵ_{xy} by simply fitting the measured asymmetry values. An advantage of this method is that it can be implemented in any usual EUV T-MOKE setup as only small angle variations of 2 - 3° are sufficient to extract the off-diagonal tensor element. The implementation of such a measurement in our setup will be described in section 4.3.

For the new fit routine, we take the whole multilayer stack of the sample into account, namely a capping layer, the thin magnetic layer and the substrate. We use the transfer matrix formalism from Ref. [94–96] and the symbolic math package (SymPy) [97] for Python to calculate the asymmetry and reflected intensities for the specific multilayer stack (e.g. Si_3N_4(5 nm)/$Fe_{19}Ni_{81}$(15 nm) /SiO_2 substrate). For the sake of clarity, the more simple equations for a single vacuum/magnetic layer interface are used in the following section.

We fit the following equation for the asymmetry for a single photon energy and multiple incidence angles θ with the free fit parameter $\epsilon_{xy} = \mathrm{Re}(\epsilon_{xy}) + \mathrm{Im}(\epsilon_{xy})$:

$$A(\theta) = \frac{2\,\mathrm{Re}(R_0^*(\theta) \cdot R_m(\theta) \cdot \epsilon_{xy})}{|R_0(\theta)|^2 + |R_m(\theta)\epsilon_{xy}|^2} \tag{3.11}$$

The incidence angle θ and the asymmetry values are measured in the EUV T-MOKE experiment, as shown in figure 3.10 - in this case for 13 different incidence angles for a $Fe_{19}Ni_{81}$ alloy. The

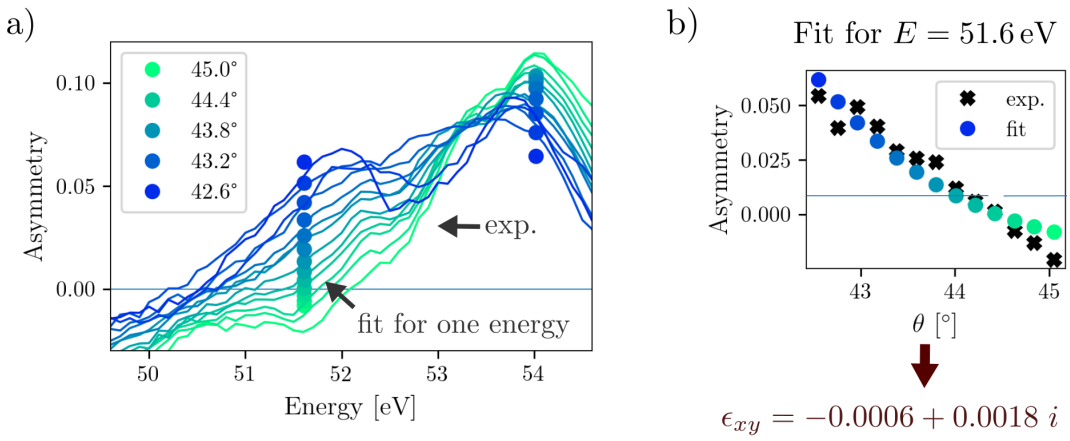

Figure 3.9.: a) Experimental asymmetry for $Fe_{19}Ni_{81}$ alloy for different incidence angles marked by different colors. We choose one specific energy, e.g. at 51.6 eV, and perform the fit for the measured asymmetry values for this energy vs. the incidence angles as shown in b). Fitting these 13 values gives the result for the free fit parameter ϵ_{xy}.

fitted values for the asymmetry (cf. equation (3.11)) are also depicted. In this example, the fit yields the value of $\epsilon_{xy} = -0.0006 + 0.0018i$ for the off-diagonal tensor element for a photon energy of 51.6 eV.

The reflection coefficients R_0 and R_m contain the refractive index n_0; therefore, the refractive index n_0 is needed as a fixed input. Ideally, one would measure the refractive index n_0 for the specific sample under investigation. As this is not trivial in the extreme ultraviolet regime, we use tabulated values for the refractive index $n_0 = 1 - \delta + i\beta$. The real part δ is from CXRO [81] and the imaginary part β is used from Willems et al. [87], who measured the magneto-optical properties of iron, cobalt and nickel with EUV magnetic circular dichroism and EUV Faraday rotation. Note that the choice of the refractive index n_0 for the sample under investigation is the largest source of error in this analysis.

To illustrate the robustness of the fit, figure 3.10 compares the extracted off-diagonal tensor element for the large data set of 13 different incidence angles with a smaller data set with only 4 incidence angles. The fit was performed for multiple energies to get the off-diagonal tensor element for all energies where the EUV intensity of the reflected high harmonic spectrum is reasonably high. The smaller data set of only 4 incidence angles still yields good results. A quantitative comparison between both fit results is shown in figure 3.10 c), where the difference between the ϵ_{xy} values for the fit with 13 incidence angles and the ϵ_{xy} values for the fit with only 4 incidence angles is shown. We observe that the fit with only 4 incidence angles yields sufficiently correct results with deviations up to max. 10%.

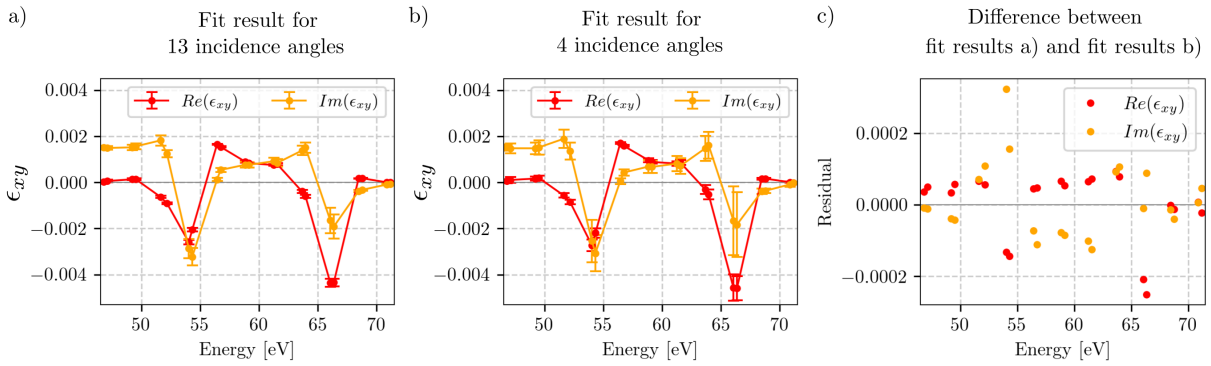

Figure 3.10.: a) Off-diagonal tensor element of $Fe_{19}Ni_{81}$ for all energies when fitting the asymmetries for 13 different incidence angles b) From the same data set, only 4 angles are used for the fit, which still provides good results but with larger errors. c) Quantitative comparison between both fit results: The difference between the ϵ_{xy} values for the fit with 13 incidence angles (a) and the ϵ_{xy} values for the fit with only 4 incidence angles (b) is shown and one magnitude smaller than the fit values themselves. This shows that the measurement with 4 incidence angles still delivers reliable results deviating up to max. 10% from the results shown in (a).

Transient dynamics of the dielectric tensor

This fit routine can also be performed for time-resolved measurements to extract the transient dynamics of the off-diagonal tensor element for all energies and times $\epsilon_{xy}(E,t)$ after an ultrafast excitation.

A similar extraction of the off-diagonal tensor was already done by Turgut et al. [52] for EUV T-MOKE data for three time steps and by Zusin et al. [70] for multiple time steps with the so called D-MOE technique.
Turgut et al. measured the EUV T-MOKE asymmetry of cobalt for 11 different incidence angles (37.5° to 52.5°) before and for two time steps after the ultrafast optical excitation. They compare their data to ab initio calculated values for the off-diagonal tensor element ϵ_{xy} and broaden and shift the theoretical $\epsilon_{xy}(E)$ curves to fit to the experimental data. Thus, they indirectly extract values for the transient off-diagonal tensor element ϵ_{xy}. Zusin et al. directly extract the transient dynamics of the off-diagonal tensor element ϵ_{xy} in cobalt using EUV D-MOE, where the magnetization of the sample is not orthogonal but "diagonal" to the plane of incidence.

After an ultrafast optical excitation, not only the magnetic properties and ϵ_{xy}, but also the refractive index n_0 change. The ultrashort laser pulse excites electrons to unoccupied states and this population change directly corresponds to a change of the optical absorption. In Turgut et al. [52], in Zusin et al. [70] and in the previously presented fit procedure, the optical properties of the sample were fixed and changes of the refractive index were neglected.

In the following section, I highlight the importance of including changes in the refractive index and present a new fit routine for the transient reflected intensity in EUV T-MOKE that takes all changes of the dielectric tensor into account – i.e., changes of ϵ_{xy} *and* ϵ_{xx}.

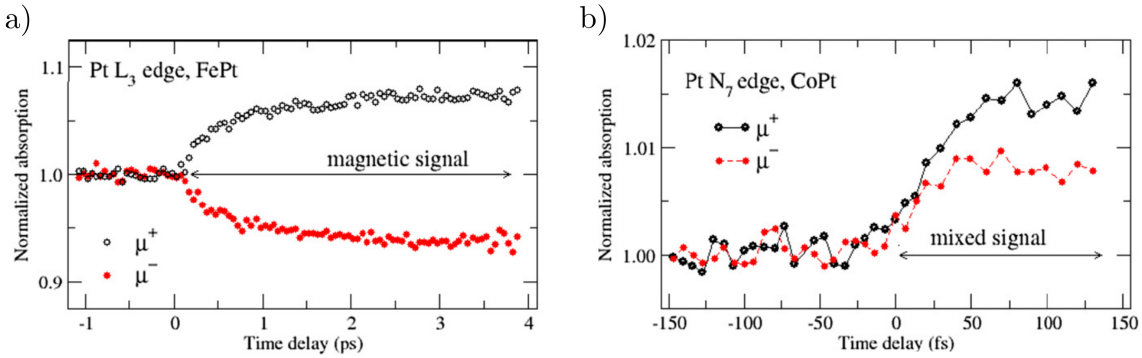

Figure 3.11.: a) FePt probed with XMCD at the L edge (11.57 keV) from [98] b) CoPt probed at the N_7 edge (72.7 eV) with helicity dependent absorption spectroscopy from [44]. The (x-ray) absorption for both helicities (μ^+ and μ^-) is normalized to its value before the pump pulse arrives. The symmetric behavior of μ^+ and μ^- in a) indicates a purely magnetic signal in contrast to the signal in b) which suggests a non-negligible charge contribution. Reprinted from Ref. [9] in accordance with the *Creative Commons Attribution 4.0* (CC BY 4.0) license.

Every experimental magneto-optical signal (XMCD, T-MOKE, ...) includes an optical contribution and is not "purely" magnetic, even though it aims to measure the magnetic properties of the sample. Thus, the reflected EUV T-MOKE intensity as well as, e.g., the transmitted intensity of EUV light in an MCD experiment are affected by refractive index changes after an ultrafast optical excitation. Oppeneer [9] stated that it is a great challenge in magneto-optics to disentangle the magnetic and the optical *charge* response after an ultrafast excitation. He exemplarily discusses two time-resolved XMCD measurements of CoPt and FePt [44,98] showing a symmetric and an antisymmetric behavior of the absorption coefficients, μ_+ and μ_- for left and right circularly polarized light (cf. figure 3.11). A purely magnetic response would require a symmetric behavior (mirror symmetry around the $\mu = 1$ axis) such that μ_+ and μ_- change in opposite directions. The missing symmetric behavior in figure 3.11 b) indicates a strong charge contribution equivalent to a change of the refractive index n_0 for the probing photon energy.

A similar argument applies to the two reflected intensities $I_{\uparrow/\downarrow}$ for opposite magnetic field directions in EUV T-MOKE:

$$I_{\uparrow/\downarrow} = I_0 \cdot \left[|R_0|^2 + |R_m \epsilon_{xy}|^2 \pm 2\mathrm{Re}(R_0^* R_m \epsilon_{xy}) \right] \tag{3.12}$$

The last term $2\mathrm{Re}(R_0^* R_m \epsilon_{xy})$ changes its sign for opposite magnetic field directions. $|R_0|^2$ is a pure optical contribution. In contrast to XMCD, the EUV T-MOKE reflected intensities

include a mixed term $|R_m\epsilon_{xy}|^2$, which is identical for both B-field directions, but also contains the off-diagonal tensor element ϵ_{xy}.

If this mixed term $|R_m\epsilon_{xy}|^2$ is negligible compared to $|R_0|^2$, and if only the off-diagonal tensor element ϵ_{xy} changes, we expect a symmetric change of the reflected intensities $I_{\uparrow/\downarrow}$. An asymmetric response of the reflected intensities $I_{\uparrow/\downarrow}$ is either an indication of a strong charge response – changing the refractive index n_0 and, thus, R_0 and R_m for this energy, or an indication of a non-negligible $|R_m\epsilon_{xy}|^2$ term. Figure 3.12 contains an example of such a symmetric and asymmetric behavior of the reflected intensities in EUV T-MOKE for a $Fe_{19}Ni_{81}$ alloy. For a photon energy of 63.9 eV, both intensity curves $I_\uparrow$ and $I_\downarrow$ increase after the ultrafast excitation and do not show a mirror symmetry around $I = 0.5$. In contrast, the signal for the photon energy of 66.4 eV exhibits a symmetric "purely" magnetic behavior as $I_\uparrow$ decreases while $I_\downarrow$ increases by the same amount.

We conclude that the transient reflected intensity curves in EUV T-MOKE possess valuable information on whether refractive index changes are present for specific photon energies or not. Based on this insight, we have developed a fit routine that handles the measured reflected EUV T-MOKE intensities $I_{\uparrow/\downarrow}$ instead of the transient asymmetries A to be able to include refractive index changes.

Novel fit routine for transient reflected intensities $I_{\uparrow/\downarrow}$

In this section, a novel fit routine for T-MOKE data is introduced including changes of the refractive index together with a quantitative comparison to the case neglecting refractive index changes.

As the incident light intensity I_0 before the sample is strongly photon energy dependent and cannot be independently measured in our setup, the reflected intensities $I_{\uparrow/\downarrow}$ (cf. equation (3.12)) are normalized to their sum before time zero $[I_\uparrow + I_\downarrow](t_0)$.

The following equations are fitted to the experimental values for each energy and time step independently, once allowing refractive index changes:

$$\frac{I_{\uparrow/\downarrow}(t,\theta)}{[I_\uparrow + I_\uparrow](t_0,\theta)} = \frac{|R_0(t)|^2 + |R_m(t)\epsilon_{xy}(t)|^2 \pm 2\,\mathrm{Re}\{R_0^*(t)R_m(t)\epsilon_{xy}(t)\}}{2\cdot|R_0(t_0)|^2 + 2\cdot|R_m(t_0)\epsilon_{xy}(t_0)|^2} \tag{3.13}$$

$$\text{with } R_0(t) = R_0[\theta,\beta(t),\delta(t)] \quad \text{and } R_m(t) = R_m[\theta,\beta(t),\delta(t)]$$
$$\text{with } R_0(t_0) = R_0[\theta,\beta(t_0),\delta(t_0)] \quad \text{and } R_m(t_0) = R_m[\theta,\beta(t_0),\delta(t_0)],$$

and once neglecting them:

$$\frac{I_{\uparrow/\downarrow}(t,\theta)}{[I_\uparrow + I_\uparrow](t_0,\theta)} = \frac{|R_0(t_0)|^2 + |R_m(t_0)\epsilon_{xy}(t)|^2 \pm 2\,\mathrm{Re}\{R_0^*(t_0)R_m(t_0)\epsilon_{xy}(t)\}}{2\cdot|R_0(t_0)|^2 + 2\cdot|R_m(t_0)\epsilon_{xy}(t_0)|^2}. \tag{3.14}$$

Neglecting changes of the refractive index implies that R_0 and R_m are time-independent and thus fixed. This corresponds to a probe vector $\vec{p}$ in the complex plane that is fixed and cannot

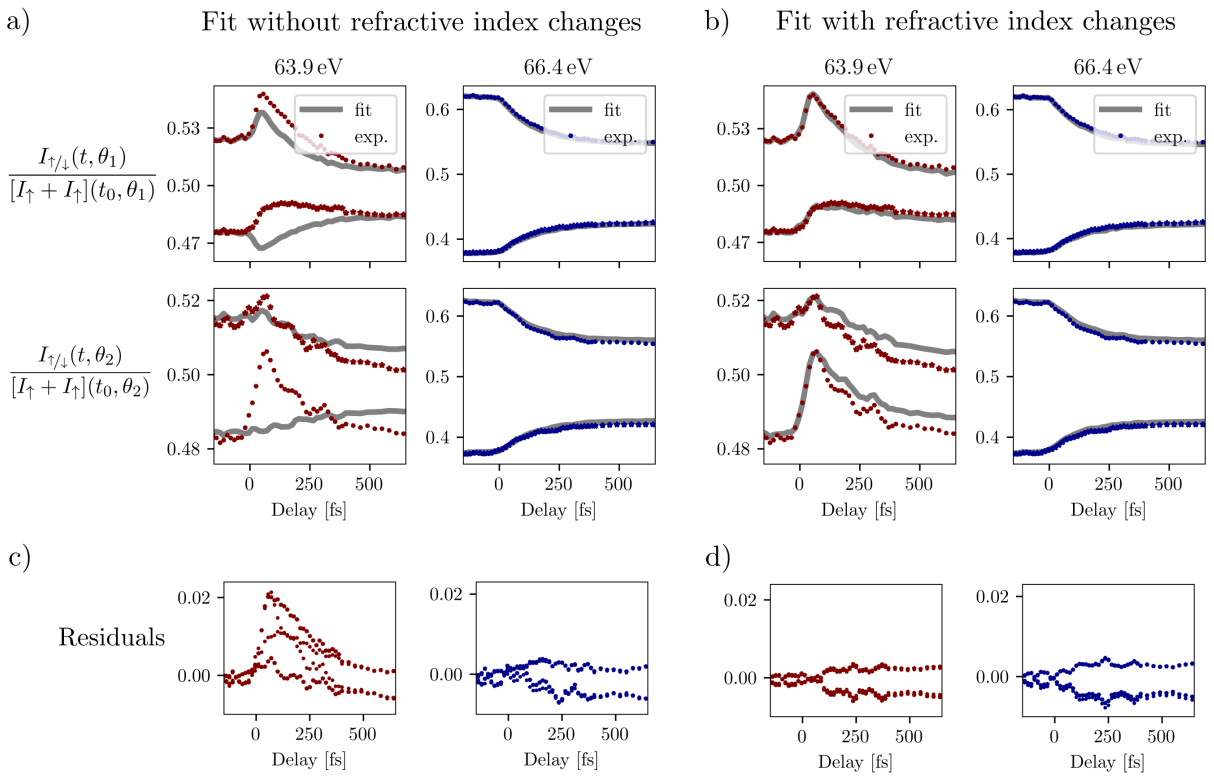

Figure 3.12.: Experimental reflected intensities and the fit results for both magnetization directions and two different incidence angles for $Fe_{19}Ni_{81}$. Exemplarily, the photon energies of 63.9 eV (red) and 66.4 eV (blue) are shown. The grey lines are the fitted values resulting from the fit routine disregarding changes of the refractive index in a) and for the fit taking into account changes of the refractive index in b). The residuals (difference between experimental and fitted value) are plotted in c) and d). The symmetric $I_{\uparrow/\downarrow}$ curves for the photon energy of 66.4 eV are in both cases fitted well. The asymmetric $I_{\uparrow/\downarrow}$ curves for 63.9 eV cannot be reproduced with the fit without refractive index changes. This is in line with the intuition that an increase in the optical absorption (of β) will increase both $I_\uparrow$ and $I_\downarrow$. However, a fit without refractive index changes only allows for $I_\uparrow$ and $I_\downarrow$ curves that go in "opposite" directions. The asymmetric behavior can be fitted well when refractive index changes are allowed in b).

change after the ultrafast optical excitation (cf. section 3.4). Literature values are used for the imaginary part of the refractive index $\beta(t_0)$ [87] and the real part $\delta(t_0)$ [81]. As a result, the off-diagonal tensor element $\epsilon_{xy}(t)$ is the only free fit parameter in this case.

When we include refractive index changes, we allow the refractive index to change with time, i.e., $n_0(t) = 1-\delta(t)+i\beta(t)$. We noticed that δ has no strong influence on the reflected intensities and cannot be accurately determined as a free fit parameter in the least-square fit. Thus, we add only the imaginary part $\beta(t)$ as a free fit parameter and determine the real part $\delta(t)$ via

the Kramers Kronig relation in an iterative process.
The details of the iterative fit routine are provided in figure 3.13. The input data are the measured reflected intensity curves $I_{\uparrow,\theta_1}$, $I_{\downarrow,\theta_1}$, $I_{\uparrow,\theta_2}$, $I_{\downarrow,\theta_2}$ normalized to their sum before t_0 since we measure the transient response for two different incidence angles θ_1 and θ_2. We fit the reflected intensities with a fixed δ and determine the off-diagonal tensor element ϵ_{xy} and the imaginary part of the refractive index β. Then, the real part of the refractive index δ is calculated via the Kramers Kronig relation and used as a fixed input in the next iteration. I implemented the KK algorithm according to Watts et al. [99] and used parts of the kkcalc program (`https://github.com/benajamin/kkcalc`) by Benjamin Watts. This approach makes use of piecewise Laurent polynomial representations of the input data such that additional energies up to 10000 eV from CXRO [81] could be included.

Figure 3.12 exemplarily depicts measured reflectivity curves and the corresponding fitted values for $Fe_{19}Ni_{81}$. The residuals in 3.12 c) and d) illustrate that the fit function (3.13) allowing for changes of the refractive index reproduces the data significantly better. This is especially true for the photon energy of 63.9 eV (red), where the $I_\uparrow$ and $I_\downarrow$ curves are asymmetric around the $I_{\uparrow/\downarrow} = 0.5$ axis and are both increasing after the optical excitation. This is an indication for a strong charge response. These refractive index changes cannot be fitted adequately with the fit function neglecting refractive index changes, where the fit function only allows for symmetric $I_\uparrow$ and $I_\downarrow$ changes (mirror symmetry around $I_{\uparrow/\downarrow} = 0.5$). This example highlights the importance of including refractive index changes and, hence, fitting the full dynamics of the dielectric tensor (i.e., ϵ_{xy} *and* ϵ_{xx}) to be able to correctly analyze the experimental data.

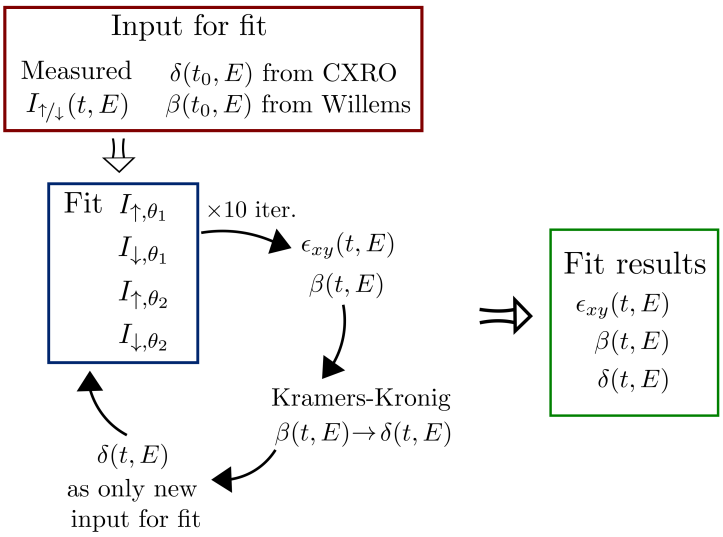

Figure 3.13.: Schematic illustration of the fit procedure for each time step and each energy. The input data are the measured reflected intensity curves $I_{\uparrow,\theta_1}$, $I_{\downarrow,\theta_1}$, $I_{\uparrow,\theta_2}$, $I_{\downarrow,\theta_2}$ normalized to their sum before t_0. As the real part of the refractive index δ is calculated from the imaginary part via the Kramers Kronig relation, the fitting is done in an iterative way where δ is the new input parameter after each iteration.

The new fit routine has the following advantages:

- It incorporates the full dynamics of the dielectric tensor. Thus, the experimental results can be more directly compared to TDDFT calculations, which also provide access to the dielectric tensor.
- Changes of the refractive index are included and, thus, also quantified. An independent measurement with s-polarized light can verify the refractive index changes predicted by the fit.
- Only small variations of the incidence angle are necessary such that this technique can be implemented in already existing T-MOKE setups with a fixed incidence angle.
- Measurement time is only by a factor of 2 - 3 longer compared to usual T-MOKE measurements as two or three incidence angles are sufficient.

The drawbacks of this new fit routine are the following:

- $\mathrm{Re}(\epsilon_{xy})$ and $\mathrm{Im}(\epsilon_{xy})$ are independent fit parameters despite they are connected to each other via the Kramers Kronig relation. Including the Kramers Kronig relation for ϵ_{xy} did turn out to be not feasible due to the low number of energies at which we have sufficient EUV photon flux to reliably extract the off-diagonal tensor element.
- The refractive index in the EUV of the sample is needed as an input for the fit and is often not available for the exact sample under investigation. Using literature values for the refractive index is possible as demonstrated here, but the choice of these parameters is likely the largest source of error for determining the off-diagonal tensor element.
- The depth dependence of the EUV light is taken into account in the transfer matrix formalism. However, so far we neglect any inhomogeneity of the optical excitation and do not account for the depth dependence of the pump pulse itself, cf. Ref. [100].

4

A tabletop setup for ultrafast element-specific magneto-optics

This chapter introduces the new EUV T-MOKE setup that was built within the scope of this thesis. The high repetition rate of 100 kHz of the used Yb-fiber laser allows for a better signal to noise ratio and shorter acquisition times compared to the setups in Uppsala [42] and Kaiserslautern [31]. In addition, the option to apply high magnetic fields (0.86 T) or to cool or heat the sample (10 K to 420 K) extends the range of experiments where new and interesting physics can be investigated. For example, we show first measurements on the material class of perovskites (here LSMO), which were only possible due to the combination of low sample temperatures and high magnetic fields.

We added the option to measure the intensity of reflected *s*-polarized light giving access to the electronic response of the system after the optical excitation (cf. section 4.2). Due to the intrinsic stability of the fiber laser, we can detect reflectivity changes on the order of 0.2%, which compares well with state-of-the-art setups [101] even without the implementation of a reference spectrometer. The last part of this chapter (section 4.3) describes the precise adjustment of the incidence angle on the sample because the incidence angle did turn out to be extremely important for the interpretation of EUV T-MOKE data.

The main part of this chapter (section 4.1) has been published in

> C. Möller, H. Probst, J. Otto, et al. Ultrafast element-resolved magneto-optics using a fiber-laser-driven extreme ultraviolet light source. *Review of Scientific Instruments*, 92(6):065107, 2021

 The author of this thesis contributed as follows: I had a significant contribution in planning and building the EUV T-MOKE setup together with Johannes Otto as part of his master thesis and Henrike Probst. I performed the corresponding measurements, data analysis, and interpretation together with Henrike Probst, and I had a significant contribution in writing of the manuscript. The data acquisition software was written by Johannes Otto. The data handling, preparation and post-production were developed and carried out by myself with contributions from Johannes Otto, Matthijs Jansen and Henrike Probst.

4.1. Ultrafast element-resolved magneto-optics using a fiber-laser-driven extreme ultraviolet light source

We present a novel setup to measure the transverse magneto-optical Kerr effect in the extreme ultraviolet spectral range based on a fiber laser amplifier system with a repetition rate between 100 and 300 kHz, which we use to measure element-resolved demagnetization dynamics. The setup is equipped with a strong electromagnet and a cryostat, allowing measurements between 10 and 420 K using magnetic fields up to 0.86 T. The performance of our setup is demonstrated by a set of temperature- and time-dependent magnetization measurements with elemental resolution.

4.1.1. Introduction

In the last decades, magneto-optical spectroscopy has led to an impressive series of discoveries in ultrafast magnetism, spanning from the discovery of optically-induced ultrafast manipulation of magnetic order [11, 103] to the experimental verification of the theoretically-predicted existence of femtosecond spin currents [20, 21, 104] and optically-induced spin transfer [12, 30, 31, 43, 44, 56, 57, 105]. Nevertheless, a complete and thorough understanding of the phenomena on a microscopic scale is still an area of active research. Here, the use of ultrashort extreme ultraviolet (EUV) light pulses to probe the instantaneous magnetization enables both few femtosecond time-resolution and the possibility to disentangle the contributions of individual elemental components of the probed system [33, 106]. Making use of the transverse magneto-optical Kerr effect (T-MOKE), full time- as well as energy-resolved (and thus element-resolved) data can be acquired from the wavelength-dependent reflection of the sample [28, 31, 36].

A commonly used light source for both magnetic [12, 28, 42, 107] and non-magnetic [108] extreme ultraviolet spectroscopy is high-harmonic generation (HHG) [109, 110]. HHG combines a compact, laboratory-scale light source with excellent properties of the EUV light; namely a high degree of coherence, broad bandwidth and ultrashort pulse durations in the low-femtosecond to attosecond regime, allowing state-of-the-art time resolution in pump-probe experiments. In comparison to alternative short-pulse EUV light sources such as free-electron lasers [111] and femtoslicing synchrotrons [112, 113], generation of a stable EUV source with high average power is challenging. In that regard, several approaches based on high-repetition-rate, high-power lasers have recently been developed [114, 115]. Up until now however, laboratory-based extreme ultraviolet magneto-optic experiments have been limited by the use of Ti:Sapphire laser systems at repetition rates below a few ten kilohertz [12, 28, 36, 42, 107].

In this article, we present a novel EUV T-MOKE experiment based on a high-repetition-rate fiber laser system to drive the high-harmonic generation. Amongst others, our photon energy range of 30 to 72 eV covers the $M_{2,3}$ absorption edges of the *3d* transition metals Co, Ni, Fe and Mn, allowing a simultaneous probing of magnetic properties of these elements. In contrast

to earlier HHG-based femtomagnetism experiments, we operate at much higher repetition rates up to 300 kHz. Based on a measurement of ultrafast demagnetization in $Fe_{19}Ni_{81}$, we will show that this setup allows for high signal quality in only limited acquisition time. Furthermore, we are able to apply high magnetic fields of up to 0.86 T and temperatures between 10 K and 420 K in our setup.

4.1.2. Setup for time-resolved T-MOKE at EUV wavelengths

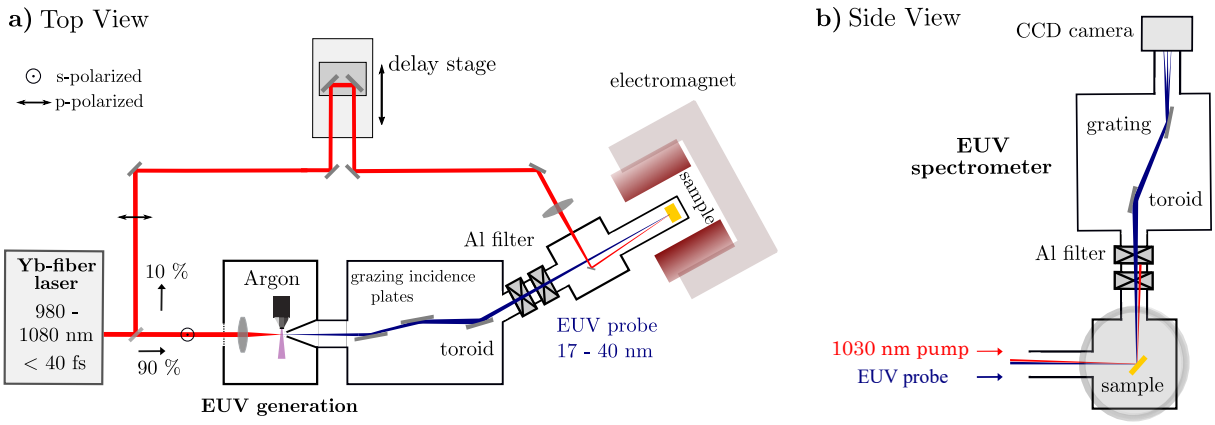

Figure 4.1.: Schematic overview of the setup: a) Top view: High harmonics are generated in an argon gas jet by intense IR pulses at a repetition rate up to 300 kHz. The fundamental beam is consequently filtered out by two grazing incidence plates and an Al filter. The toroidal mirror focuses the EUV beam onto the sample inside the electromagnet. b) Side view: After reflection on the sample, the high harmonic spectrum is analyzed by our custom-built spectrometer composed of a toroidal mirror, a grating and a CCD camera. The pump beam is coupled into the vacuum chamber and blocked by a second Al filter after reflection on the sample. Note that the grating dispersion is shown to be in plane for visualization purposes and is in fact normal to the drawing plane.

The experiment makes use of the transverse magneto-optical Kerr effect (T-MOKE) to measure the magnetization of the sample. In T-MOKE, the sample magnetization is aligned parallel to the sample surface and perpendicular to the plane of incidence of the light. Here, a magnetization-dependent change in the reflectivity can be observed for p-polarized light. As this can be measured by a simple intensity measurement, i.e., without polarization analysis, T-MOKE is especially well-suited in the EUV spectral range. Nevertheless, it should be noted that several polarization analysis techniques have recently been developed to access other magneto-optical effects at EUV and soft-X-ray wavelengths [116–118].

The quantity accessible by T-MOKE is the magnetic asymmetry A, which is the difference in reflected intensity from the sample for both magnetization directions ($I_\uparrow$ and $I_\downarrow$), normalized to

the sum of the intensities [33, 36, 119, 120]

$$A = \frac{I_\uparrow - I_\downarrow}{I_\uparrow + I_\downarrow} \approx 2\mathrm{Re}\left[\frac{\sin(2\theta_0)\epsilon_{xy}}{n^4\cos^2\theta_0 - n^2 + \sin^2\theta_0}\right]. \tag{4.1}$$

The index of refraction n and the off-diagonal elements of the dielectric tensor ϵ_{xy} describe the reaction of the full quantum-mechanical system to the incident light field, and can be calculated by considering all possible electronic transitions for the material's spin-resolved band structure and instantaneous electron occupation. [36, 120] As a result, both n and ϵ_{xy} are wavelength-dependent, and change rapidly near absorption edges. In particular, resonant enhancement of ϵ_{xy} at the M edges of transition metals [121, 122] combined with a general enhancement of the magnetic asymmetry at absorption edges [33] leads to a strong, wavelength-dependent T-MOKE signal in the EUV range for the *3d* transition metals. Here, spectroscopy can be optimally used to disentangle elemental contributions from the magnetic asymmetry.

In the second step of Eq. (4.1), the magnetic asymmetry was approximated by inserting the expressions for *p*-polarized reflected intensities under the assumption that the Fresnel coefficient is large compared to the magneto-optical term. [33] Higher order terms of the magnetization-dependent off-diagonal element of the dielectric tensor ϵ_{xy} are neglected. From this expression, it can be deduced that, in thermal equilibrium, the asymmetry is proportional to the magnetization inside the sample. The expression is maximized when the denominator approaches zero. This is exactly the case for $\tan\theta_0 = n$, which is the condition for the Brewster angle. Since $n \approx 1$ in the EUV range, the optimal angle of incidence corresponds to $\theta_0 \approx 45°$.

The fiber-laser HHG light source

Here, we present a T-MOKE setup using EUV light from a high-harmonic generation (HHG) light source to probe the sample. Ultrafast (de)magnetization dynamics are induced by tuneable pump pulses from the same high repetition-rate fiber laser system used to drive the HHG. After reflection from the sample, the EUV light is dispersed in a custom-built spectrometer and the diffracted harmonics are detected by a CCD camera. A schematic overview of the setup is shown in Fig. 4.1.

Ultrashort laser pulses with a center wavelength of 1030 nm, tuneable repetition rate up to 300 kHz, pulse energy of up to 150 µJ and pulse lengths below 40 fs are generated by a fiber laser system (Active Fiber Systems). This is achieved by self-phase modulation of 300 fs pulses from an ytterbium-doped fiber amplifier in a krypton-filled hollow-core fiber and subsequent compression by chirped mirrors. The beam is split into a pump and a probe beam by a variable attenuator, consisting of a $\lambda/2$-plate and two broadband thin film polarizers. The s-polarized output of the attenuator is focused by a 100 mm focal length lens into an argon gas jet to generate high harmonics, which provides the probe beam in our experiment. In order to optimize the HHG process, the gas jet is mounted on a 3-axis positioning system. Efficient HHG was observed at an argon backing pressure of 17 bar for a gas nozzle diameter of 100 µm.

Pumping of the HHG generation chamber is realized by placing a small conical aperture directly opposite to the gas outlet close to the HHG generation point, which already removes most of the gas load. In addition, a second bypass removes residual gas, leading to a pressure of 1.1 mbar in the generation chamber. To allow for high vacuum conditions in the mirror chamber, a 1 mm differential pumping aperture is placed less than 2 mm from the generation point. This yields a pressure of 2×10^{-4} mbar in the mirror chamber. The generated high harmonics are separated from the fundamental by two grazing-incidence plates (GIP). [123] These fused silica plates are anti-reflection coated for 1030 nm on the front and backside, whereby most of the fundamental beam is transmitted and dumped outside the vacuum chamber. An additional top Ta_2O_5 coating of the GIP allows for a high reflection (76% calculated reflectivity for 54.2 eV) of the EUV spectrum at 10° grazing incidence. After the GIPs, a B_4C-coated toroidal mirror (276 mm focal length at 15° grazing incidence angle, 74% calculated reflectivity for 54.2 eV) focuses the probe beam onto the sample in a 350x140 µm^2 spot ($1/e^2$-diameter). The EUV light then passes a 100 nm thick aluminum filter which is mounted in front of the sample in a VAT valve to block any residual fundamental light.

The generated EUV photon flux was estimated to be 1.9×10^{10} photons/second/eV assuming a reflection of 8×10^{-5} at the $Fe_{19}Ni_{81}$ sample [81] for 54.2 eV. This corresponds to an average generated power of 0.16 µW, and 4.6×10^9 photons/second/eV at the sample for the 45$^{\text{th}}$ harmonic.

Pump beamline

A second variable attenuator in the pump beamline allows for manipulation of the pump beam intensity. A motorized delay line changes the optical path length with respect to the probe path. After passing a 350 mm focal length lens, the pump beam is coupled into the vacuum chamber such that the angle between the pump and the EUV beamline is less than 2°. The beam diameter on the tilted sample was determined to be 760x1020 µm^2. The pulse duration is measured by intensity autocorrelation to be 58 fs, assuming a Gaussian pulse shape. The pump beam is s-polarized with respect to the plane of incidence on the sample for the measurements shown in this paper.

Sample environment

The sample environment is a custom-made chamber based on a CF150 flange and designed to fit in the 45 mm wide pole gap of the electromagnet (see Fig. 4.2). The flange can be opened from the side, which enables easy access to the sample. For this purpose the electromagnet surrounding the sample chamber is mounted on rails, allowing to remove the magnet and providing unobstructed access to the sample chamber. The switching time of the electromagnet varies from 60 ms for 100 mT up to 600 ms for the maximum field strength of 860 mT.

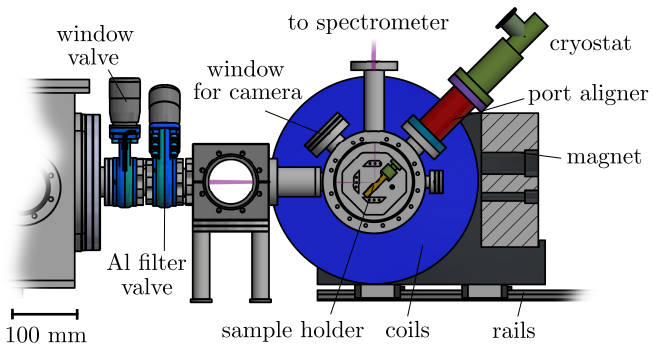

Figure 4.2.: Technical drawing of the custom-built sample chamber, providing a view directly into the sample chamber.

The samples are mounted on a removable copper sample holder attached to a cryostat, which is fixed at a 45° angle with respect to the incoming pump and probe beams. In order to make small changes to the position and angle of the sample, the cryostat is attached to the chamber with an ultrahigh vacuum (UHV) port aligner. The continuous-flow UHV cryostat (Janis Research ST400) enables temperature control of the sample in the range of ≈10 to 420 K. Typically, the pressure inside the chamber is below 1×10^{-7} mbar during operation, however, even UHV conditions can be achieved by baking out the vacuum chamber.

To verify spatial overlap of the pump and probe beam, the diffuse reflection of the pump and fundamental of the high harmonics on the sample is imaged with a CMOS sensor. The temporal overlap is achieved by observing sum frequency generation of both IR pulses in a beta barium borate (BBO) crystal at the sample position or recording interference fringes with a beam profiler. Both of these methods can be performed outside of the vacuum system by inserting a moveable mirror directly in front of the sample. This determination of the temporal overlap is limited by a small difference in the optical path lengths of the fundamental and the high harmonics. Therefore, a final determination of the temporal overlap is done by searching for the onset of demagnetization as probed by the EUV light.

Spectrometer design

Spectroscopy of the reflected EUV light allows for the investigation of the sample magnetization and is realized by a custom-built spectrometer based on a plane grating as the dispersive element and a toroidal mirror as the focusing element. The spectrometer was designed to achieve an energy resolution of about 1 eV to distinguish between the individual harmonics, while also achieving a high efficiency. [124]

The sample reflects both the pump and probe beams towards the spectrometer chamber (see Fig. 4.1b). Here, a second aluminum filter is introduced into the beam path to block the reflected pump beam. The EUV beam is focused towards the CCD-camera (GE 2048 512 BI UV, Greateyes) by a toroidal mirror, which is identical to the toroidal mirror used to focus the

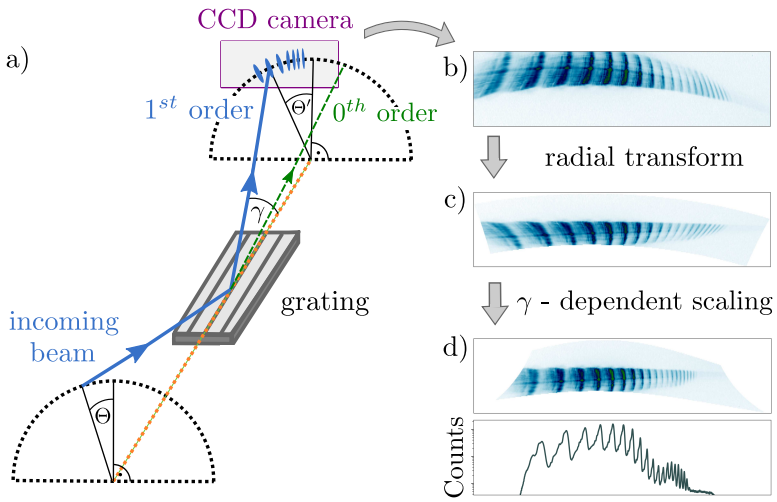

Figure 4.3.: a) Schematic overview of diffraction in the off-plane geometry for the planar grating: The light hits the grating with an azimuthal angle θ, the diffracted high harmonics lie on a cone with half-angleγ, also referred to as the altitude angle. b) Typical 2D high harmonic spectrum recorded with the EUV camera prior to any corrections. c) 2D spectrum after radial transformation onto a (θ', γ)-coordinate system. d) Fully corrected 2D and integrated high harmonic spectrum after a γ-dependent scaling of the diffraction angle.

EUV probe beam on the sample. As shown in Fig. 4.3a, the planar reflection grating is positioned in the off-plane geometry, where the grating grooves lie parallel to the plane of incidence of the light. An advantage of this geometry is that it allows for the use of efficient blazed gratings while maintaining the low grazing incidence angle which is necessary for high reflectivities at EUV wavelengths [124]. The grating is gold-coated and has a groove density of 1800 lines/mm. Given the blaze angle δ of 9.3°, optimal diffraction efficiency is achieved at the altitude angle γ of 6.5° for wavelengths near the M-edges of the *3d* ferromagnets. To prevent camera exposure during the sensor readout procedure, a shutter is positioned between the toroidal mirror and the grating.

A consequence of this spectrometer design is that the EUV wavefront incident on the grating is curved. Equivalently, it can be said that the azimuth angle θ and the altitude angle γ of the beam on the grating have a certain spread. This will lead to a distortion of the measured spectrum (see Fig. 4.3b), which is calculated here. The grating equation for this system is [125]

$$m\lambda\sigma = \sin\gamma(\sin\theta - \sin\theta'), \tag{4.2}$$

where m is the diffraction order, λ the wavelength, σ the grating constant and θ' the exit angle. Substituting $\theta \to \theta_0 + \Delta\theta$ and $\gamma \to \gamma_0 + \Delta\gamma$ and performing a Taylor expansion around $\Delta\theta = \Delta\gamma = 0$, we find

$$\theta' = \theta'_0 - c_1\Delta\theta + c_2\Delta\gamma + O(\Delta\theta^2 + \Delta\theta\Delta\gamma + \Delta\gamma^2). \tag{4.3}$$

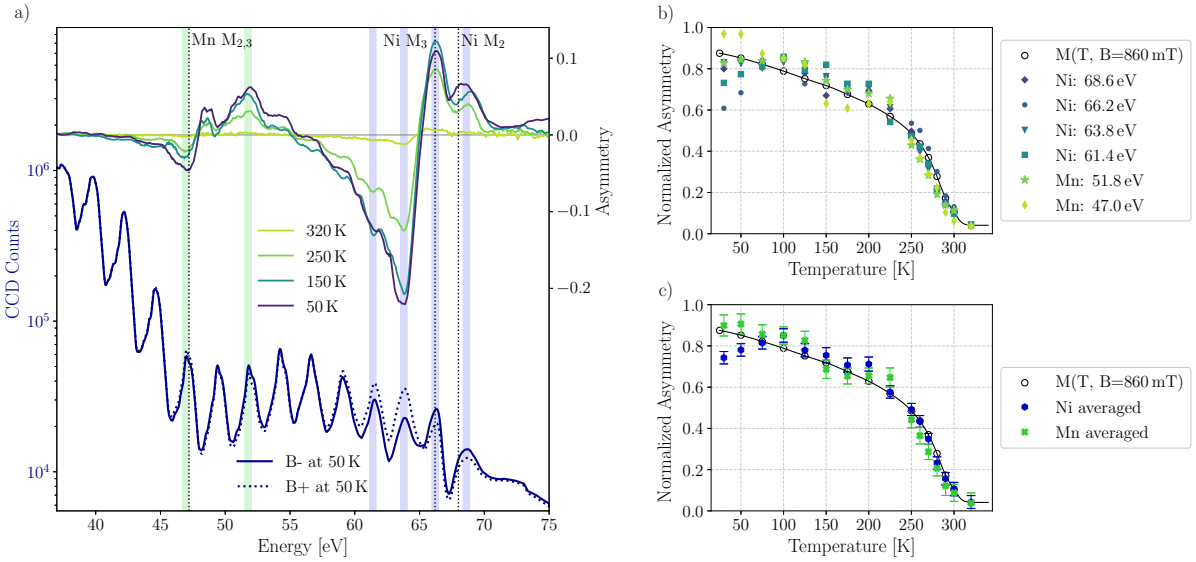

Figure 4.4.: Temperature dependence of the magnetic asymmetry of the LNMO phase transition. a) The magnetic asymmetry, together with typical HHG spectra at 50 K for the different magnetization directions. The indicated 0.5 eV intervals in green and blue correspond to the evaluated areas in the asymmetry for Mn and Ni. The dashed lines illustrate the M-absorption edges of both elements. b) Temperature-dependent magnetic asymmetry for 0.5 eV energy intervals around the relevant high harmonic energies of Mn and Ni. c) The magnetic asymmetry traces for Mn and Ni, averaged over all relevant high harmonics, including statistical error margins. The asymmetry traces in (b) and (c) nicely follow the $M(T, B = 860\ \text{mT})$ data points which were recorded using SQUID magnetometry. The black line is an interpolation of the $M(T, B = 860\ \text{mT})$ data and serves as a guide to the eye.

In our experimental geometry, $c_1 \approx 1.1$ and c_2 is typically on the order of 3. Higher order terms can be ignored because they are typically one to two orders of magnitude weaker than the linear terms. From this result, we can conclude the following: 1) the term linear in $\Delta\theta$ will increase the wavefront curvature, leading to an astigmatic focus of the diffracted beam. On the camera, this results in spots which are elongated perpendicular to the spectral direction. 2) the term linear in $\Delta\gamma$ will shift the diffracted beams depending on their altitude angle. Effectively, this leads to a grating dispersion which is stronger for shallower grazing incidence angles on the grating.

In order to correct for this deformation of the measured spectrum, we first transform the cartesian coordinates of the camera onto a (θ', γ)-coordinate system. Next, we apply a γ-dependent scaling of the diffraction angle, eliminating the tilt of the high harmonics. Finally, we integrate the two-dimensional measurement along the spatial dimension without loss of spectral resolution. An exemplary raw spectrum and the aforementioned procedure are shown in Fig. 4.3b-d.

In daily operation, the aluminum L_3 edge at 72.7 eV and the known separation of the high harmonics by twice the fundamental frequency are used to calibrate the energy of the recorded high harmonics. In addition, the energy calibration of the spectrum is verified by inserting a 200 nm thick tin filter, which transmits EUV light up to 23.6 eV allowing to identify the 19^{th} harmonic (22.9 eV) of our fundamental driver.

4.1.3. Exemplary experimental results and analysis

In the following, we present temperature- and time-dependent measurements of the magnetic asymmetry. The results show the ferromagnetic phase transition of La_2NiMnO_6 and the distinct ultrafast magnetization dynamics of iron and nickel in a $Fe_{19}Ni_{81}$ alloy. These measurements demonstrate the capabilities of our setup to record magnetization traces with a high signal-to-noise ratio over a broad range of sample temperatures between 10 and 420 K and with femtosecond time resolution.

Temperature-dependent magnetic asymmetry

Thin-film perovskite magnanites exhibit rich phase diagrams due to the strong correlations between charge, lattice and spin degrees of freedom [126–128], which can be of particular interest for ultrafast spin dynamics. Here, we investigated the ferromagnetic to paramagnetic phase transition in the double perovskite La_2NiMnO_6 (LNMO). The magnetic asymmetry was recorded in a temperature range of 30 K to 320 K. Typical HHG spectra at 50 K for both magnetization directions and the resulting asymmetry spanning the $M_{2,3}$ absorption edges of manganese (47.2 eV) and nickel (66.2 eV and 68 eV) for different temperatures are depicted in Fig. 4.4a. The measurements were performed in an applied magnetic field of 860 mT. For each temperature, 500 spectra with an exposure time of 1 second per magnetization direction were recorded. In order to analyze the quantitative temperature dependence of the asymmetry, we calculated the mean asymmetry in a 0.5 eV energy interval around the relevant high harmonic peaks for Mn and Ni, indicated by the shaded areas in Fig. 4.4a. As a reference, we extracted the sample magnetization at $B = 860$ mT from full hysteresis curves $M(B)$ in the temperature range of 5-300 K as measured using a superconducting quantum interference device (SQUID) magnetometer. In order to compare the observed magnetic asymmetry to the $M(T, B = 860\ \text{mT})$ data, we have normalized the magnetic asymmetry to the sum of the asymmetry values for all temperatures and then scaled it with the magnetization $M(T, B = 860\ \text{mT})$ integrated over the full temperature range.

The temperature-dependent magnetic asymmetry for all relevant harmonic peaks is shown together with the $M(T, B = 860\ \text{mT})$ data in Fig. 4.4b. The normalized asymmetry values for Mn and Ni show good agreement with the $M(T, B = 860\ \text{mT})$ reference measurement performed with SQUID across the entire temperature range. The expected loss of magnetization with increasing temperature is clearly visible. The remaining non-negligible magnetization beyond the

phase transition in Fig. 4.4b is induced by the strong external field of 860 mT applied during the measurement and evident in both the T-MOKE measurement and SQUID $M(T, B = 860\ \text{mT})$ data.

To extract a mean value of the magnetic asymmetry for both Mn and Ni, we averaged the asymmetry of the relevant harmonics for both elements. The resulting averaged magnetic asymmetry traces are shown in Fig. 4.4c. From the overall good agreement between the EUV magnetic asymmetry measurement and the SQUID measurement probing the element-integrated bulk magnetization, we conclude that static EUV T-MOKE effectively probes the magnetization of a 10-20 nm layer close to the sample surface in the steady state with elemental resolution. Small differences between the MOKE and SQUID signals likely stem from different probing volumes for both techniques or unwanted surface adsorbates at low temperatures, which may influence the MOKE signal slightly.

Time-resolved EUV-T-MOKE

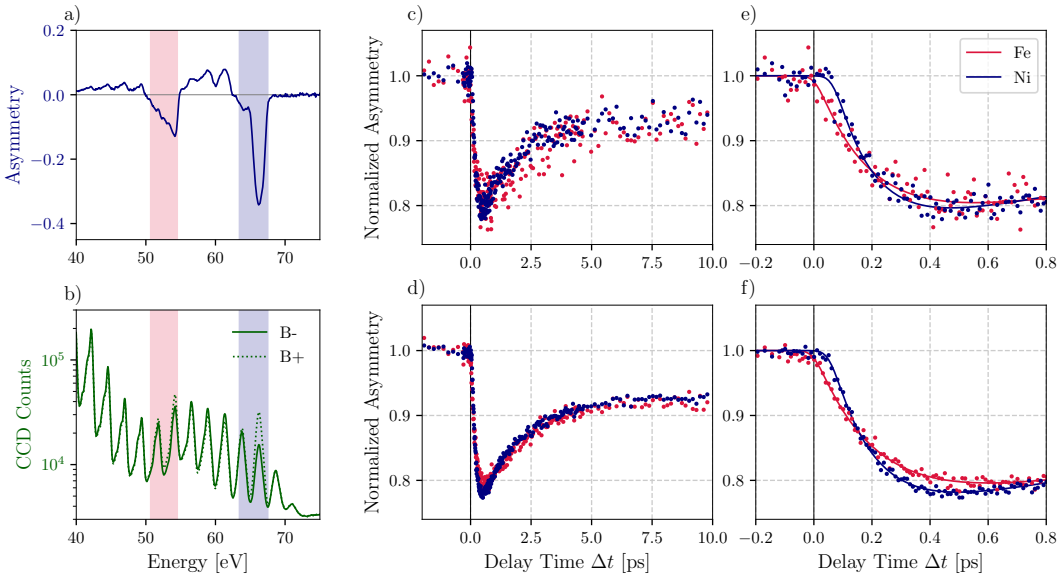

Figure 4.5.: Time-resolved demagnetization measurement of $Fe_{19}Ni_{81}$ for a short (1 hour) and long (12 hours) time measurement. a) Typical magnetic asymmetry of the sample before arrival of the pump pulse. b) Corresponding high-harmonic spectra for both magnetic field directions. c, d) Relative demagnetization time traces for iron and nickel for one and twelve hours measurement time respectively. Here, the asymmetry is averaged over the depicted energy intervals in (a) and normalized to time delays before time zero. e, f) Zoom-in on the short-timescale dynamics of (c) and (d) respectively. The solid lines are least-square fits according to a double exponential function (eq. (5.1)), the results of which are given in table 4.1.

To demonstrate the performance of our setup we recorded the time evolution of the ultrafast

demagnetization in a $Fe_{19}Ni_{81}$ thin film at 100 mT applied field. Ultrafast demagnetization is initiated by a 58 fs, 1.2 eV pump pulse (measured by autocorrelation, assuming Gaussian pulse shape). The absorbed pump fluence is ≈ 0.5 mJ/cm^2. At this fluence, the 750 mW incident power on the sample leads to a limited thermal demagnetization of around 5 % for our pulse repetition rate of 100 kHz. The measurement time was 12 hours which corresponds to 96 0.7-second measurements of the asymmetry per delay position. We will compare the results from this long integration to results from shorter integration slices selected from this data.

The results are summarized in Fig. 4.5, including recorded EUV spectra for both magnetization directions after subtraction of a background image, the resulting asymmetry according to equation (4.1), and the time dependence of the normalized magnetic asymmetry for a 12-hour measurement as well as an exemplary 1-hour data set selected from the long measurement. For the time-dependent data, the average magnetic asymmetry was determined for the indicated energy intervals in Fig. 4.5a. Negative time delays indicate that the EUV pulse probes the sample before the pump pulse arrives.

For the analysis of the raw asymmetry data, large energy regions around the M absorption edges were chosen: Fe between 50.7 and 54.5 eV and Ni between 63.4 and 67.5 eV. By integrating the off-diagonal component of the dielectric tensor over a wider energy range, we are less sensitive to spectrally distinct band-structure renormalization and population dynamics [19,31,36,44,88, 89,129], and we effectively probe the element-specific magnetization. Already from the 1-hour dataset, we can easily resolve the delayed demagnetization dynamics between nickel and iron, as previously seen in Refs. [29,31,41,42], which highlights the excellent signal-to-noise ratio of our setup. In order to provide a more quantitative analysis of the signal quality, we analyse the measurement data before zero delay. For the 1-hour dataset, we find an RMS noise level of 1.5%. For each data point, this constitutes 8 measurements of the magnetic asymmetry with a total measurement time of 15 seconds. For the complete dataset with 96 measurements per data point, this is reduced to 0.7%. On visual inspection, this noise level is comparable to, e.g., Ref. [42], however our results were obtained with less than 7% of the measurement time. We also compared our results to permalloy data from the setup used in Ref. [31]. Here, our setup provides 4 times lower RMS noise for the short term measurement, and still 2.7 times lower RMS noise for the long term measurement. In terms of total measurement time, this amounts to an order of magnitude improvement.

As an exemplary analysis of the data, we fit the time evolution of the asymmetry for both energy intervals using a double-exponential function convolved with a Gaussian function G(t) with a full width at half maximum of 60 fs, taking into account a pulse duration of 15 fs for the high harmonics. The full fit model is:

$$\frac{A(t)}{A(t<t_0)} = G(t) \circledast \left[1 - \Theta(t-t_0) \cdot \left[\Delta A_m \cdot \left(1 - e^{-\frac{t-t_0}{\tau_m}}\right) - \Delta A_r \cdot \left(1 - e^{-\frac{t-t_0}{\tau_r}}\right)\right]\right]. \quad (4.4)$$

Here, t_0 defines the onset of the demagnetization process, τ_m and τ_r are the demagnetization

Fe, 50.7 to 54.5 eV	1 hour	12 hours
t_0 (fs)	6 ± 10	0 ± 3
ΔA_m	0.253 ± 0.012	0.276 ± 0.005
ΔA_r	0.182 ± 0.010	0.199 ± 0.004
τ_m (fs)	185 ± 21	214 ± 8
τ_r (ps)	1.96 ± 0.24	1.85 ± 0.08
Ni, 63.4 to 67.5 eV	**1 hour**	**12 hours**
t_0 (fs)	67 ± 5	55.3 ± 1.9
ΔA_m	0.264 ± 0.008	0.280 ± 0.003
ΔA_r	0.197 ± 0.007	0.206 ± 0.003
τ_m (fs)	136 ± 10	146 ± 4
τ_r (ps)	1.5 ± 0.1	1.68 ± 0.04

Table 4.1.: Fit results using Eq. 5.1 of the demagnetization traces in Fig. 4.5. For the least-squares fit, measurement data were weighted according to the data spread at each delay individually. The given error margins correspond to the 1-sigma standard deviations of the fit.

and remagnetization constants, respectively, ΔA_m is proportional to the maximal fractional demagnetization, and ΔA_r is proportional to the fast remagnetization. For our data, ΔA_r is smaller than ΔA_m, meaning that the sample does not return to its ground state in the measured 10-ps time range. Full remagnetization is only achieved on a longer timescale. The least-square fit results are listed in table 4.1. In addition to the delayed dynamics in nickel, we observe a faster demagnetization time at the nickel M-edge as well as a slightly stronger demagnetization for the selected spectral ranges, which may be due to the shallower probing depth for the Ni M-edges compared to the Fe M-edges in case of permalloy [81].

Crucially, the fit results for the 1-hour data set differ only slightly from the results for the complete 12-hour data. The differences in demagnetization dynamics between iron and nickel are well-reproduced by this much shorter measurement. To verify that these results are not simply by choice of our 1 hour data set, we split the 12-hour data set in one-hour chunks and repeated the least-square fit for each of these. From this analysis, we find that overall, the 1-hour fit results closely match with the 12-hour result. However, the predicted error margins from a single least-square fit underestimate the true variance of the analysis results by roughly a factor two. For example for the onset of demagnetization in nickel, we find values centered on 53 fs with a 1-sigma standard deviation of 9 fs. Such differences are acceptably small however, and can easily be explained by small drifts in the experimental setup over the course of the long measurement.

4.1.4. Conclusion

In summary, we have presented a novel setup combining a high-repetition-rate high harmonic light source with a T-MOKE-setup enabling high magnetic fields up to 0.86 T and sample temperatures down to 10 K. We have shown that this setup allows for the detailed measurement of element-specific magnetization behavior in complex samples such as the double perovskite LNMO. Furthermore, using a $Fe_{19}Ni_{81}$ permalloy thin film as a well-known reference sample [29, 41, 42], we have demonstrated the capabilities of our setup to measure high-quality ultrafast demagnetization dynamics. We find that just 15 seconds of measurement time for each delay position allows us to achieve a noise level of 1.5% compared to the base signal before time zero. Consequently, a single hour of measurement time allows for a detailed view into the ultrafast dynamics in a 10-picosecond time window at a 40 fs average time step. For example, this measurement already allows us to determine the relative delay of the demagnetization in nickel compared to iron with 10 fs accuracy. Extending our measurement to 12 hours, we acquire excellent data with only 0.7% RMS noise, which can be directly attributed to the use of the high-power Yb-fiber laser, operating at 100 kHz repetition rate.

In the future, we will apply our setup to the measurement of element-resolved magnetic responses as a function of temperature, time and magnetic field. Amongst others, this work will contribute to a more profound microscopic understanding of the dynamics in complex magnetic alloys and strongly correlated electron systems.

4.1.5. Acknowledgments

H.P, K.S, S.M., V.M. and D.S. acknowledge support from the German Science Foundation through project number 399572199. G.S.M.J. acknowledges funding by the Alexander von Humboldt Foundation. We thank Manfred Albrecht from the University of Augsburg for the fabrication of the Permalloy sample. We thank S. Häuser, B. Stadtmüller and M. Aeschlimann for the Permalloy data from their setup, which we used for the RMS noise comparison. Also, we wish to thank Christof Schmidt and the team of the central workshop of physics for their excellent support in constructing the HHG EUV-T-MOKE setup.

4.1.6. Sample Preparation

The double perovskite LNMO film with a thickness of $d \approx 100$ nm was epitaxially grown on a MgO(100) substrate by means of a solution-based and vacuum-free metalorganic aerosol deposition (MAD) technique [130]. The investigated $Fe_{19}Ni_{81}$ sample is a 15-nm thin film deposited with magnetron sputtering at room temperature on a silicon substrate (Si/SiO_2(100 nm)) and capped with 5 nm Si_3N_4. The sample is poly-crystalline and exhibits an in-plane magnetization orientation.

4.2. Reflectivity measurements with s-polarized light

By measuring the transient magnetic asymmetry in our EUV T-MOKE setup, we aim to get a better understanding of the transient spin polarization and, thus, the ultrafast magnetization dynamics of our sample. The interesting information about the electronic redistribution of the charges after the optical excitation is only indirectly included. As described by La-o-Vokariat et al. [33] and in section 3.4, the s-polarized reflected intensity $I_s = |R_{0,s}|^2 \cdot I_0$ depends only on the refractive index of the sample n_0 and the incidence angle θ. The reflectivity for s-polarized light of the sample does not depend on the magnetization, in contrast to p-polarized EUV light used in common T-MOKE measurements. Changes in the electron occupancy in the band structure after ultrafast optical excitation will manifest as changes in the refractive index and hence in the reflection of s-polarized EUV light.

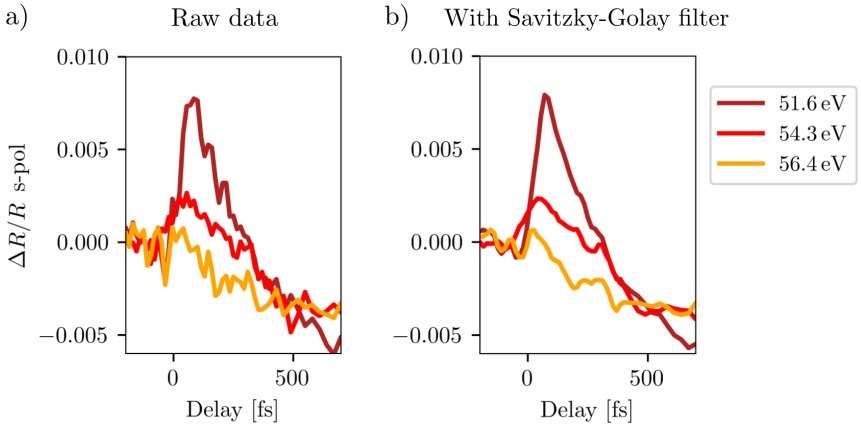

Figure 4.6.: Exemplary measurement of the reflectivity of s-polarized light from $Fe_{19}Ni_{81}$ for photon energies around the iron M absorption edge. a) shows the raw data and b) shows the data smoothed with a Savitzky-Golay filter (window length: 7 data points, polynomial order: 3). The photon energy of 54.3 eV shows an increase in reflectivity of only 0.2 %. The absorbed fluence for this measurement was $\approx 0.83 \pm 0.2$ $^{mJ}/_{cm^2}$ and the incidence angle was $\theta = 43.4°$.

Within this thesis, we have modified our setup to allow measurements of reflected *s*-polarized EUV light by changing one of the grazing incidence plates[1] shown in figure 4.1. The grazing incidence plates are necessary to filter out the fundamental beam that co-propagates with the generated EUV light. They have high reflection for the EUV light and an AR coating to achieve low reflection for the fundamental 1.2 eV beam. These AR coatings are highly polarization sensitive and work only for either p or s-polarization. Therefore, we exchanged one of these incidence plates to efficiently suppress the reflection of p-polarized light (later s-pol on sample) while the other plate still suppresses the reflection of s-polarized light (later p-pol on sample). This leads to a higher thermal load on the aluminum filter in the EUV T-MOKE measuring

[1] new incidence plate: Laser Comp. HR15-30HTp1030/80/AR RW80-50-10UV

geometry (p-pol on sample). Nonetheless, the aluminum filter is able to withstand the 500 mW residual power of the fundamental beam because of a relatively large beam diameter at this position. The grazing incidence plates tend to degrade over time due to carbon contamination, which reduces the performance of the AR coating. The residual power on the aluminum filter could be further reduced by exchanging the old grazing incidence plate. Such contamination usually becomes visible after a few months of continuous operation time.

Figure 4.6 shows the measured reflectivity change for s-polarized light after the optical excitation with a 1.2 eV pump pulse for a $Fe_{19}Ni_{81}$ alloy. The reflectivity change is defined as $\frac{\Delta R}{R} = \frac{I_s(t) - I_s(t_0)}{I_s(t_0)}$. This measurement may also serve as an example of the good data quality we obtain in our setup. We are able to resolve an increase in reflectivity of only 0.2 % at the photon energy of 54.3 eV. Johnsen et al. [101] used an additional reference spectrometer to improve their data quality in their EUV T-MOKE setup. Even without using such a reference spectrometer, we have a better signal-to-noise ratio when comparing our data to the s-polarized reflectivity of Ni published in Johnsen et al. [101], where a 2.8 % reflectivity change is resolved. The reflection for s-polarized light is multiple magnitudes higher compared to the reflection for p-polarized light allowing for short exposure times of our camera (e.g., 80 ms) and, thus, short total acquisition times (2.6 minutes per delay position in this case).

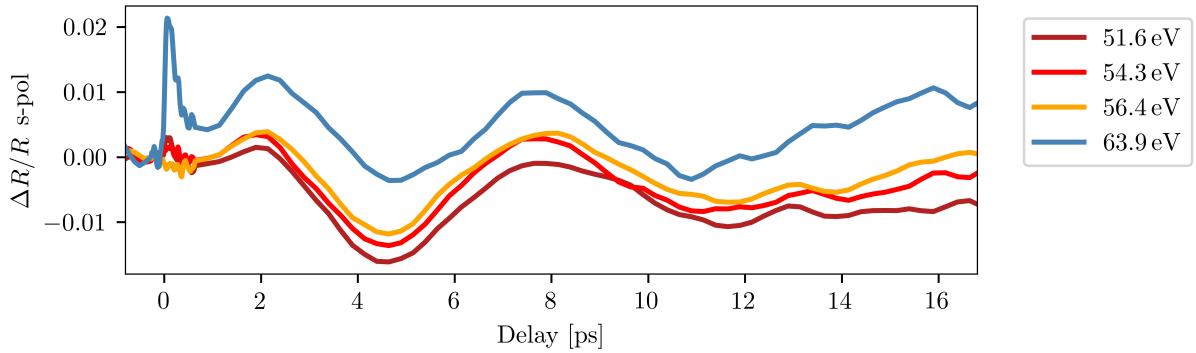

Figure 4.7.: Reflectivity change of s-polarized light for large time delays after the ultrafast excitation of $Fe_{19}Ni_{81}$. We can clearly observe oscillations with a period of 5.57 ps (for 63.9 eV), which can be attributed to a standing acoustic wave within the magnetic film. The absorbed fluence in this measurement was $0.55 \pm 0.2\, {}^{mJ}/_{cm^2}$ and the incidence angle was $\theta = 43.5°$. The data was smoothed with the same Savitzky-Golay filter used in figure 4.6.

As demonstrated in [131] and [101], the reflected EUV light also gives access to acoustic waves present in our sample. The ultrafast optical excitation with our pump pulse leads to a thermal expansion of the thin metallic film and induces a strain wave, which partially enters the substrate. Figure 4.7 shows the measured reflectivity change for s-polarized light of $Fe_{19}Ni_{81}$ for larger time delays. For a photon energy of 63.9 eV, we find a frequency of 180 GHz for this oscillation.
The acoustic impedance of the FeNi thin film and the underlying substrate (SiO_2 on Si) are

quite different resulting in a high acoustic mismatch of approx. 0.7 [132, 133]. Thus, the strain wave enters partially into the substrate, but a significant part is reflected at the FeNi/SiO_2 interface and a standing acoustic wave within the 15 nm FeNi film forms. As the refractive index of the FeNi film is strain-dependent, the reflected EUV light is affected by this standing acoustic wave. Further details on acoustic waves and Brillouin scattering in our measurement data can be found in the master thesis of Mariana Brede [134].

4.3. Transverse magneto-optical Kerr effect for different incidence angles

The magnetic asymmetry in EUV T-MOKE is usually measured for incidence angles around $\theta = 45°$, which is close to the Brewster angle for EUV light. Thus, only a few p-polarized photons will be reflected from the sample, which makes the intensity measurement of the reflected EUV light more challenging, but enhances the magnetic contrast in the reflected light.

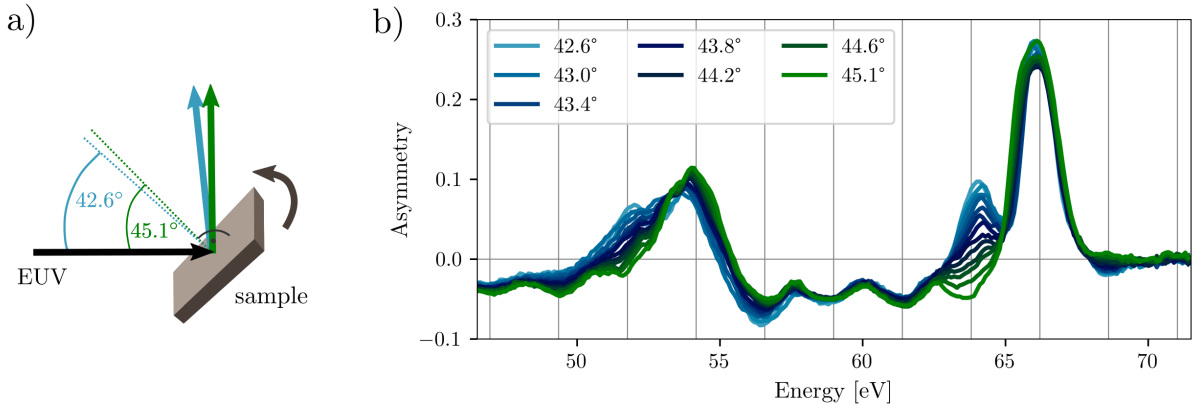

Figure 4.8.: a) Schematic drawing of the sample and two different incidence angles when tilting the sample. b) Recorded magnetic asymmetries for $Fe_{19}Ni_{81}$ for incidence angles between 42.6° and 45.1°. The zero crossings shift and – for certain spectral regions – the asymmetry changes its sign for different incidence angles.

The shape of the static magnetic asymmetry strongly depends on the angle of incidence θ as described in section 3.4. To vary the angle of incidence in a controlled manner, we have included a new sample holder in our setup. It is mounted on a vacuum compatible SmarAct stage (SLC-1720-UHVT-NM) and a Smaract tip-tilt mirror mount (STT-12.7-UHVT-NM). This allows for tilting of the sample (<3° angular range) with respect to the incident beam under vacuum conditions, i.e., during the measurements. We are also able to move the sample after each measurement without changing the incidence angle and, hence, avoid influences from effects like carbon contamination. The drawback of this sample holder is the lack of temperature control (heating or cooling), which is only possible with the cryostat holder.

Figure 4.8 b) shows the asymmetries of $Fe_{19}Ni_{81}$ for 13 different incidence angles varying from

42.6° to 45.1°. For certain photon energies, e.g., 63.8 eV and 51.2 eV, the changes in the asymmetry are more pronounced and lead to sign changes of the asymmetry.

The SmarAct tilting mirror mount has no active feedback loop and, thus, cannot provide any information on the angle of the sample. To quantify and track the angle change of the sample, we use an alignment laser, which hits the sample near normal incidence as shown in figure 4.9 a). The position of the reflected alignment laser on a screen is recorded with a camera. The recorded positions of the reflected alignment laser are shown in figure 4.9 b) for the 13 incidence angles used in figure 4.8. This procedure allows for the precise tracking of the angle change of the sample. In this case, the alignment laser moved by a distance of 17.3 mm, which corresponds to an angle change of 2.5° (distance sample – screen of 40.5 cm).

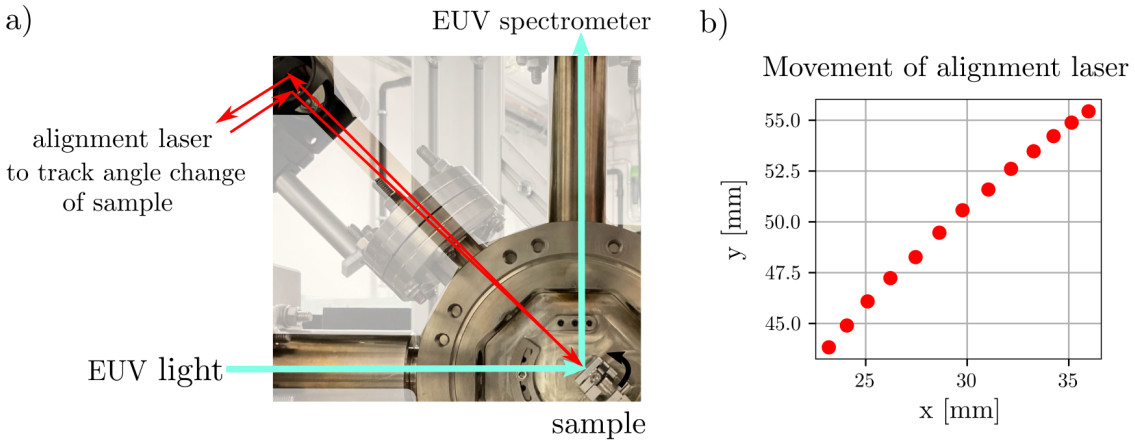

Figure 4.9.: a) Photo of the sample holder and beampath of the EUV light, which is reflected from the sample and then guided to the EUV spectrometer. The beampath of the alignment laser hitting the sample close to normal incidence is also shown. b) Position of the reflected alignment laser when tilting the sample. From this information, the tilting of the sample (here, 2.5°) can be calculated.

Using the adjustment laser, the change of the incidence angles between consecutive measurements can be quantified, but not the exact absolute value of the incidence angle. We estimate that the absolute angle calibration is accurate to within 0.3°.

In our setup, tilting of the sample to adjust the incidence angle does not cause strong changes of the incidence angles in the EUV spectrometer because the plane of incidence turns by 90° between the sample and the entrance in the EUV spectrometer. This means that a change of the incidence angle on the sample only results in a change of the height of the beam on the optics in the spectrometer. In other setups, an adjustment of optics in the EUV spectrometer might be necessary to counteract the change in the angle of incidence.

With this improvement of the setup, we are able to precisely control the incidence angle on the sample during the T-MOKE measurement, which is essential for the results presented in chapter 5.

5

Optical intersite spin transfer in FeNi alloys

This chapter presents a joint experimental and theoretical study to verify the optical intersite spin transfer in $Fe_{50}Ni_{50}$ and $Fe_{19}Ni_{81}$ alloys. We apply our new approach to extract the dielectric tensor from angle-resolved EUV T-MOKE data – described in section 3.5 and our publication [63]. Thus, we can directly compare the experimental transient magneto-optical response with the same quantity calculated by TDDFT. Our results also explain the origin of the often discussed delay between Ni and Fe in FeNi alloys.

The goal of this chapter is to provide answers to the following questions:

- Does optical intersite spin transfer (OISTR) really exist in FeNi alloys?
- Do quantitative differences exist between the spin transfer in $Fe_{50}Ni_{50}$, $Fe_{19}Ni_{81}$ and pure Ni?
- What causes the delay between Ni and Fe in FeNi alloys?
- How can we interpret the transient dynamics in the EUV T-MOKE asymmetry which are drastically different for different angles of incidence?
- Are the OISTR signatures accompanied by a refractive index change?

The main part of this chapter (section 5.1) has been published in

> C. Möller, H. Probst, G. S. M. Jansen, et al. Verification of ultrafast spin transfer effects in FeNi alloys. `arXiv:2306.02793 [cond-mat.mtrl-sci]`, 2023

 The author of this thesis contributed as follows: I performed the experiments together with Henrike Probst, Maren Schumacher and Mariana Brede. The measurements on ferromagnetic nickel were performed by Henrike Probst and are also published in Ref. [63]. I developed the new fitting routine to reconstruct the dielectric tensor together with Henrike Probst and Matthijs Jansen. I contributed substantially to the interpretation of the data and to the writing of the manuscript.

5.1. Verification of ultrafast spin transfer effects in FeNi alloys

The optical intersite spin transfer (OISTR) effect was recently verified in $Fe_{50}Ni_{50}$ using magneto-optical Kerr measurements in the extreme ultraviolet range. However, one of the main experimental signatures analyzed in this work, namely a magnetic moment increase at a specific energy in Ni, was subsequently found also in pure Ni, where no transfer from one element to another is possible. Hence, it is a much-discussed issue whether OISTR in FeNi alloys is real and whether it can be verified experimentally or not. Here, we present a comparative study of spin transfer in $Fe_{50}Ni_{50}$, $Fe_{19}Ni_{81}$ and pure Ni. We conclusively show that an increase in the magneto-optical signal is indeed insufficient to verify OISTR. However, we also show how an extended data analysis overcomes this problem and allows to unambiguously identify spin transfer effects. Concomitantly, our work solves the long-standing riddle about the origin of delayed demagnetization behavior of Ni in FeNi alloys.

5.1.1. Introduction

The ability to drive spin dynamics by ultrashort laser pulses offers a unique opportunity to bring the field of spintronics into the femtosecond regime, as demonstrated for example by the successful application of superdiffusive spin currents [20,21,136,137] in spintronic emitters [138] and the possibility of direct magnetic phase switching by femtosecond laser pulses [139–141]. Recently, a fascinating discovery was made in this context: given a suitable material, it is possible to drive spin transfer between sublattices directly by a strong optical field [12, 30–32, 44, 57]. This process, called optical intersite spin transfer (OISTR), even precedes the ultrafast demagnetization process and thus provides a path to even faster spintronic applications [142].

OISTR was first proposed theoretically by the Sharma group [43] and has meanwhile been experimentally verified in a number of experiments. In the OISTR process, an ultrafast optical excitation drives spin-preserving electronic transitions from below the Fermi level to above the Fermi level. Due to the exchange-split bands in ferromagnets, different numbers of spin-up and spin-down electrons are excited by the laser pulse, which leads to an ultrafast spectral redistribution of the electron density as well as to an ultrafast spectral redistribution of the spins and thus to ultrafast dynamics in the spin-polarization. If the initial states for such an excitation are predominantly found in one elementary subsystem, e.g. of an alloy, and the final states are predominantly found in another elementary subsystem, an intersite spin-transfer occurs, which offers the potential for an advanced and extremely fast control of magnetic behavior.

One of the first experiments to verify the OISTR effect was an experiment on a $Fe_{50}Ni_{50}$ alloy using the ultrafast transverse magneto-optical effect (T-MOKE) in the extreme ultraviolet (EUV) region [31]. The T-MOKE experiment showed a spectrally-dependent increase in magnetic asymmetry in Ni and a concomitant decrease in Fe, and the corresponding transient dynamics of majority and minority spin occupation in the $Fe_{50}Ni_{50}$ alloy were calculated by TDDFT.

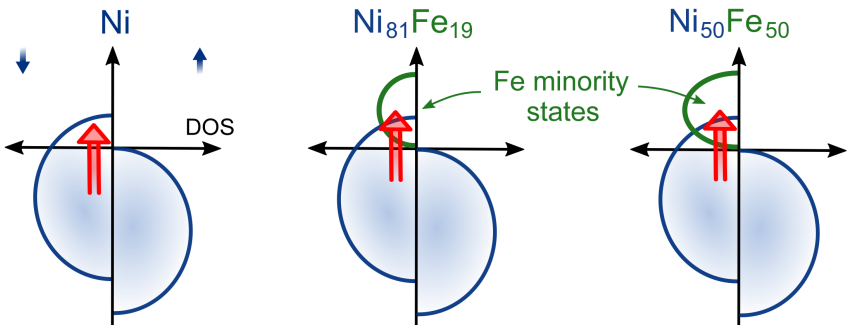

Figure 5.1.: Simplified illustration of the 3d states in Ni, $Fe_{19}Ni_{81}$ and $Fe_{50}Ni_{50}$. The addition of Fe in the alloys leads to additional unoccupied states in the minority channel that can be populated through OISTR. TDDFT calculations predict a stronger OISTR effect in $Fe_{50}Ni_{50}$ compared to $Fe_{19}Ni_{81}$ due to the larger amount of available Fe states above the Fermi level [143]. On the other hand, in elemental Ni, the OISTR process is not possible.

However, a similar ultrafast increase in Ni has recently also been observed in pure Ni material [63, 89], where spin transfer to another subsystem is not possible. On the one hand, such a signature is not unexpected, since ultrafast excitation also drives occupation changes in pure materials. On the other hand, the question arises to what extent the observed increase in the magnetic asymmetry is a valid signature to verify spin transfer from Ni to the Fe in $Fe_{50}Ni_{50}$. The situation is further complicated by the fact that it was found that identical magnetization dynamics in EUV T-MOKE can appear drastically different depending on the precise experimental geometry [63]. The critical question is therefore whether OISTR can experimentally be verified in $Fe_{50}Ni_{50}$.

In this work, we present new data on this topic in a comparative experimental and theoretical study of laser-driven spin transfer processes in $Fe_{50}Ni_{50}$, $Fe_{19}Ni_{81}$ (permalloy), and pure Ni (see Fig. 5.1). We revisit the previously observed signatures of the OISTR effect and, following the approach that we developed in Ref. [63], perform a full time-resolved reconstruction of the dielectric tensor. This allows us to directly compare the same quantity obtained from experiment and theory: namely, the transient dynamics in the dielectric tensor. We find that in all three materials signatures of the ultrafast laser-driven spectral redistribution of spins can be clearly identified. Furthermore, we find that the amplitude of these dynamics at the Ni site increases with increasing Fe content in the alloy, supporting the OISTR description. In the case of $Fe_{50}Ni_{50}$, we experimentally verify the transfer of minority spins from the Ni subsystem to the Fe subsystem, i.e. the OISTR effect. Finally, we are also able to explain the origin of the much discussed delayed demagnetization behavior of Fe and Ni in these alloys [29,40–42,88,102].

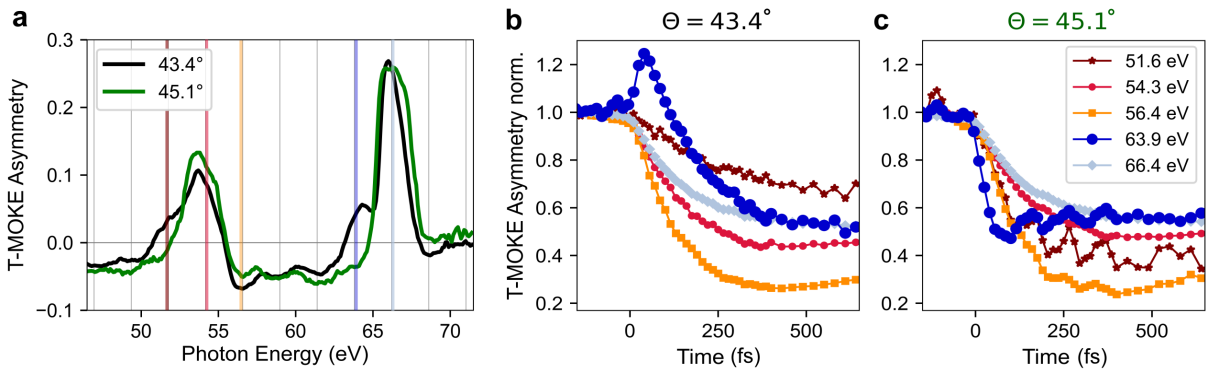

Figure 5.2.: Apparently contradictory EUV T-MOKE measurements of OISTR in $Fe_{19}Ni_{81}$, recorded at different EUV incidence angles and otherwise identical conditions (the data of $Fe_{50}Ni_{50}$ and Ni can be found in the Supplementary Figure 1). (a) Static T-MOKE asymmetry for two incidence angles. Note that the magnetic asymmetry changes sign around 52 eV and 64 eV for the two different incidence angles. (b, c) Time-resolved magnetic asymmetry traces for 43.4° and 45.1° incidence angle, respectively. The analyzed photon energies around the M absorption edges of Fe and Ni are marked as colored bars in (a). At 43.4°, the typical transient increase at 63.9 eV that was previously associated with OISTR is seen [31], while no such increase is visible at 45.1°.

5.1.2. Results

We begin with a measurement of $Fe_{19}Ni_{81}$ that very clearly illustrates that an increase in T-MOKE asymmetry in a specific spectral region may not be sufficient to verify spin transfer effects without further analysis. Fig. 5.2a shows energy-resolved magnetic asymmetries measured with EUV T-MOKE of the $Fe_{19}Ni_{81}$ sample for two different incidence angles (θ) of the EUV light. While the asymmetries look quite similar, the zero crossings are slightly shifted so that there are spectral regions where the asymmetry is negative for one angle of incidence and positive for the other, most notably at 52 and 64 eV. Most curiously, we find apparently contradictory ultrafast dynamics of the T-MOKE asymmetry in the time-resolved experiment for these spectral regions: Fig. 5.2b shows the time-resolved change of the asymmetry as a function of EUV energy at $\theta = 43.4°$. Here, the signal at 63.9 eV (dark blue) shows a time-resolved increase in the T-MOKE asymmetry, which is exactly the signature used to verify the OISTR effect in our previous work. However, in Fig. 5.2c, for a slightly different angle of incidence ($\theta = 45.1°$), the same spectral region shows the exact opposite behavior, namely an ultrafast decrease. Note that we observe this behavior for all three samples Ni, $Fe_{19}Ni_{81}$, and $Fe_{50}Ni_{50}$ (cf. Supplementary Figure 1). Clearly, no conclusion should be drawn from these data without further knowledge of the OISTR effect and its signatures in the T-MOKE signal.

To overcome this problem, we apply an extended analysis, based on the experimental determination of the transient dynamics of the dielectric tensor that we developed in Ref. [63]. This

analysis shows that the peculiar behavior of the asymmetry increase and decrease for two different incidence angles is due to a transient rotation of the off-diagonal element of the dielectric tensor (ϵ_{xy}) in the complex plane. If this rotation of ϵ_{xy} happens at photon energies near the zero-crossings of the T-MOKE asymmetry, it can lead to opposite dynamics in the magnetic asymmetry due to the projection of ϵ_{xy} onto an angle-dependent probe vector (see Ref. [63] for the description of the analysis and the influence of the rotation of ϵ_{xy} on the T-MOKE asymmetry spectra; see SI for the additional data needed to perform this analysis). Instead, extracting ϵ_{xy} from the angle-dependent T-MOKE asymmetry data has several advantages: (i) the real part of ϵ_{xy} is related to the spin-polarization of the unoccupied states and can also be measured by other techniques, such as X-ray magnetic circular dichroism (XMCD); (ii) the quantity ϵ_{xy} is now independent of the measurement technique or geometry used; (iii) the transient changes in ϵ_{xy} allow a direct comparison with TDDFT calculations.

Fig. 5.3a shows TDDFT calculations [55, 144] of the transient dynamics of the spin-resolved occupation in Fe and Ni in the $Fe_{50}Ni_{50}$ sample. A calculation of $Fe_{19}Ni_{81}$ is computationally very costly due to the large required supercell size and was therefore not performed for the present study. The calculations for $Fe_{50}Ni_{50}$ are similar to the results presented in Hofherr *et al.* [31], but adapted for the pump pulse energy (1.2 eV) and pulse duration (47 fs) of the present experiment [145]. While the Fe and Ni electrons share a common (metallic) band structure in the alloy, the character of the different states can be projected onto bands originating dominantly from the Ni or Fe subsystem. The OISTR effect then manifests itself in transitions from minority states below the Fermi level with predominantly Ni character to minority states above the Fermi level with predominantly Fe character. Of course, other transitions within the subsystems also contribute to the optical response, but they do not transfer spin from one subsystem to the other subsystem and are therefore not discussed further here. Transitions between the subsystems within the majority channel are also possible, but these are only minor changes compared to the strong changes in the minority channel (cf. Supplementary Figure 4). As can be seen from these calculations, there is a spectral region below the Fermi level that shows a depletion of minority spins for states with a predominant Ni character, leading to an increase in the energy-resolved magnetic moment at the Ni site. Conversely, there are spectral regions above the Fermi level of the Fe states where the increase in minority spins leads to a rapid quenching of the energy-resolved magnetic moment. Hofherr *et al.* [31] found two similar features in the time-resolved asymmetry and interpreted them as indicators of the OISTR effect.

However, for the reasons given above, we now go one step further and calculate from TDDFT the signature of OISTR on the transient dynamics of the dielectric tensor [37, 146]. Fig. 5.3b shows the real part of ϵ_{xy} from theory (lines) and experiment (points) for two exemplary pump-probe delays (before time zero and at 55 fs). The first important observation from the calculated time- and spectrally-resolved $\mathrm{Re}(\epsilon_{xy})$ data is that the spectrally very distinct dynamics in the spin-resolved DOS (Fig. 5.3a) are strongly broadened. This is due to the intrinsic linewidth of the 3p

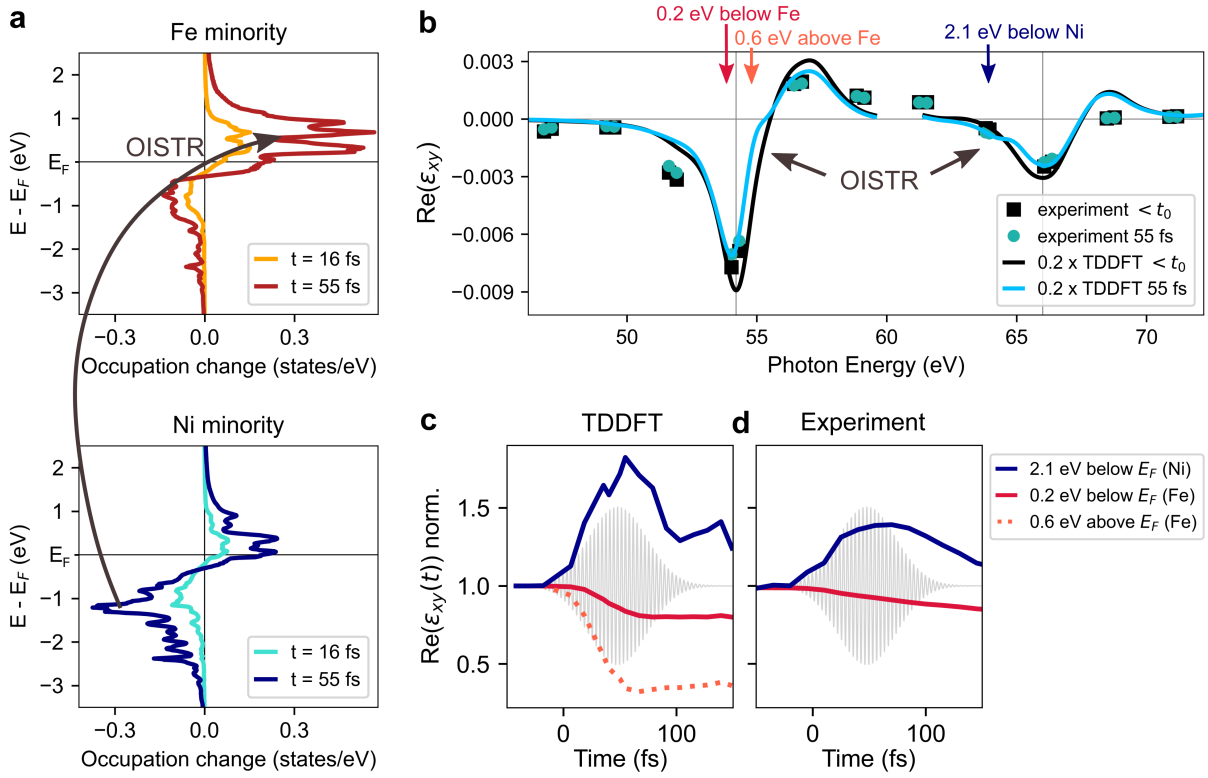

Figure 5.3.: TDDFT calculations of OISTR in $Fe_{50}Ni_{50}$, compared to experiment. a) The transient occupation change of minority spins at the Ni and Fe sites in $Fe_{50}Ni_{50}$. The OISTR process excites minority spins in Ni from below the Fermi edge to Fe minority states above the Fermi edge. b) Comparison of the static off-diagonal dielectric tensor element to the transient state at 40 fs, as extracted from measured EUV T-MOKE data (points) and TDDFT calculations (lines). For the red, orange, and blue arrows, 54.2 eV and 66 eV were used for the M edges of Fe and Ni, respectively, which allows to reference the energy scale to the Fermi level. In (c) and (d), the transient evolution of the real part of ϵ_{xy} is shown at specific energies referenced to the Fermi level from TDDFT and experiment, respectively. For quantitative comparison, ϵ_{xy}(t) was normalized to its value before the pump pulse arrives.

core levels and their partial overlap. Nevertheless, the second important observation is that it is still possible to pinpoint the OISTR effect from the theory data: For photon energies between 63.0 eV and 64.4 eV, there is a relative increase in $\mathrm{Re}(\epsilon_{xy})$ caused by the pump-induced ultrafast loss of minority spins in Ni. Conversely, in the 55 eV energy region, Fe shows a rapid decrease in $\mathrm{Re}(\epsilon_{xy})$ on the timescale of the pump pulse due to the addition of transferred minority spins originating from Ni states.

Fig. 5.3c summarizes the expected transient behavior of $\mathrm{Re}(\epsilon_{xy})$ from TDDFT for the discussed energies, with the blue curve showing the increase in Ni and the orange dotted curve showing the corresponding rapid decrease in Fe, now approximately referenced to the Fermi levels of Ni and Fe, respectively, by subtracting the respective M-edge energies from the photon energies (cf. Fig. 5.3b for the corresponding photon energies). In direct comparison, Fig. 5.3d shows the experimentally extracted transient dynamics of $\mathrm{Re}(\epsilon_{xy})$ for respective photon energies. First, we see that we are able to verify the important increase in $\mathrm{Re}(\epsilon_{xy})$ in experiment, which is indicative of the loss of minority spins in Ni due to optical pumping (blue line). Second, however, we do not have sufficient EUV intensity in the important spectral region just above the Fe M-edge, which is expected to show the strong and rapid decrease due to the increase of minority spins above the Fermi level (orange dotted line in theory, Fig. 5.3c, absent in experiment, Fig. 5.3d). The next available EUV harmonic with sufficient intensity in our experimental data is at 0.2 eV below Fe M-edge, and we find good qualitative agreement with theory (red lines in Fig. 5.3c,d). However, there is also a qualitative discrepancy with respect to timescales larger than 80 fs, where the theoretical magnetization remains constant while the experimental magnetization decreases. This can be understood by considering the limitations of the TDDFT calculations: TDDFT is well suited to describe the very early magnetization dynamics induced by the pump pulse and in particular the excitation. On longer timescales, however, the well-known demagnetization processes evolve, not all of which are included in TDDFT. In particular, Elliott-Yafet spin-flip electron-phonon scattering [17] is not included in TDDFT, which explains that TDDFT does not capture the full magnetization decrease for timescales >80 fs. In summary, we can clearly verify the loss of minority spins in the Ni subsystem from these experimental data, but we have no experimental evidence that these spins are transferred to the Fe subsystem.

For the present work, we now aim to compare the spectrally-resolved T-MOKE data of pure Ni [1], where only an inter-energy spin-transfer is involved, with data from $\mathrm{Fe_{19}Ni_{81}}$ and $\mathrm{Fe_{50}Ni_{50}}$, where an intersite spin transfer between Ni and Fe becomes possible and is predicted by theory (for the $\mathrm{Fe_{50}Ni_{50}}$ alloy). Fig. 5.4a shows the experimentally analyzed transient change of $\mathrm{Re}(\epsilon_{xy})$ for the spectral region where the OISTR-induced increase was expected and verified in the case of $\mathrm{Fe_{50}Ni_{50}}$ (dashed). Compared to $\mathrm{Fe_{50}Ni_{50}}$, the increase in $\mathrm{Fe_{19}Ni_{81}}$ (dotted) is much less pronounced and mostly seen as a delay in the case of pure Ni material (line). From this data, we can directly conclude that the OISTR-relevant transition is most efficiently excited in the

[1] This data is reproduced from Ref. [63], where we describe the ϵ_{xy} analysis procedure in detail.

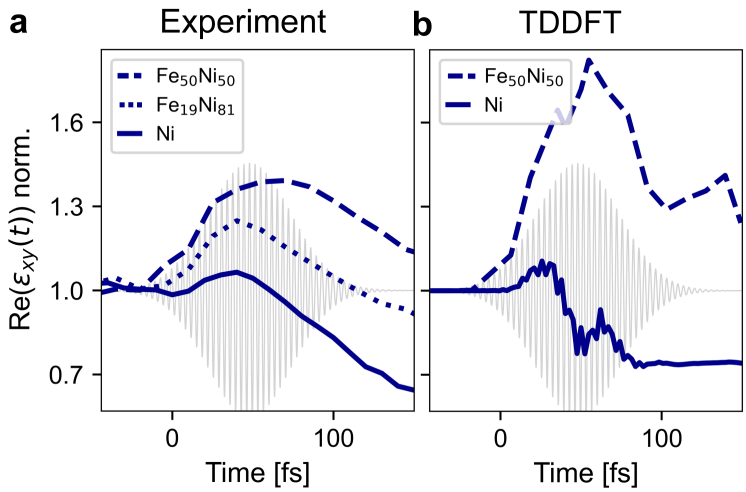

Figure 5.4.: Comparison of the transient off-diagonal tensor element $\mathrm{Re}(\epsilon_{xy})$ for 63.9 eV for $Fe_{50}Ni_{50}$, $Fe_{19}Ni_{81}$ and Ni, (a) extracted from measured EUV T-MOKE data, and (b) calculated by TDDFT. The spin transfer between Ni and Fe is visible by an increase of $\mathrm{Re}(\epsilon_{xy})$ at 63.9 eV, which probes Ni minority states below the Fermi level. In experiment, the spin transfer is found to be more efficient in $Fe_{50}Ni_{50}$ than in $Fe_{19}Ni_{81}$. In Ni, minority electrons are excited from below to above the Fermi level, which results in a short and comparatively small increase of $\mathrm{Re}(\epsilon_{xy})$.

$Fe_{50}Ni_{50}$, less efficiently in $Fe_{19}Ni_{81}$, and even less in Ni. In comparison with theory (Fig. 5.4b), we again find good qualitative agreement for $Fe_{50}Ni_{50}$ as discussed above, but also for Ni. Note that the absorbed fluence and the quenching of the transient asymmetry are not the same for all three measurements (cf. SI).

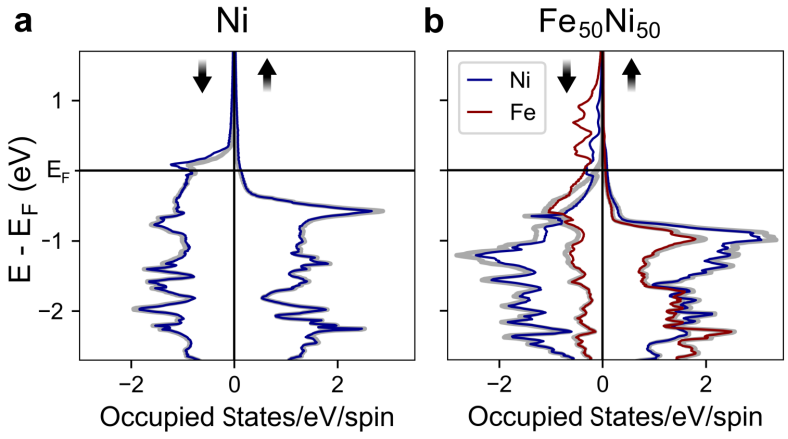

Figure 5.5.: Occupied minority and majority states before (grey) and after the optical excitation (t=55 fs, blue and red) calculated with TDDFT for Ni (a) and $Fe_{50}Ni_{50}$ (b).

To shed light on the origin of the observed differences in excitation efficiencies in the minority channels, we take a closer look at the band structure of these materials, and possible excitation pathways. Fig. 5.5a shows the spin-resolved density of states for pure Ni material. In Ni, more

(spin-conserving optical) excitations are possible in the minority channel than in the majority channel. These transitions are captured in theory and experiment by a loss of minority spins below the Fermi level, and lead to the observed small increase for $\mathrm{Re}(\epsilon_{xy})$ at ≈2.1 eV below the Ni edge. In the case of $Fe_{50}Ni_{50}$, as shown in Fig. 5.5b, the situation is different. Here, the addition of Fe adds additional final states above the Fermi level in the minority channel. Thus, a first glance at the band structure suggests that additional transitions from the Ni minority states below the Fermi level to the Fe minority states above the Fermi level become possible. According to theory, this is indeed the case and leads to the strong relative increase of $\mathrm{Re}(\epsilon_{xy})$ at 2.1 eV below the Ni edge and, in addition, to a rapid relative decrease of $\mathrm{Re}(\epsilon_{xy})$ just above the Fe edge. While we cannot probe the rapid decrease with the given EUV light source in our experiment, we very well reproduce the modified efficiency of the OISTR transition and therefore conclude that the experiment also shows that in $Fe_{50}Ni_{50}$ OISTR is operative, i.e. minority spins from Ni are indeed pumped into minority states of Fe by the ultrafast laser excitation. Next, we see that the $Fe_{19}Ni_{81}$ alloy, according to the experiment (see Fig. 5.4a), lies between the situation of Ni, where no intersite spin transfer is possible, and $Fe_{50}Ni_{50}$, where OISTR is apparently strong. Using the same reasoning as above, one would expect some amount of Fe DOS above the Fermi level, but less than in the case of $Fe_{50}Ni_{50}$. Indeed, such a series of spin-resolved DOS has already been calculated in Ref. [143] and is in full agreement with the expectations and observations developed above.

Finally, we would like to discuss our new results in relation to the results on permalloy obtained in the last decade with EUV T-MOKE (Mathias *et al.* [29], Günther *et al.* [41] suppl., Jana *et al.* [42]). In this work, Fe and Ni showed a delayed demagnetization behavior with identical demagnetization time constants, which was recently verified in time-resolved X-ray magnetic circular dichroism (XMCD) experiments at the L-edges of Fe and Ni [40]. The identical demagnetization time constants for Fe and Ni aren't surprising: Fe and Ni are strongly exchange-coupled in these alloys. However, the important question has always been what causes the delay between the two subsystems. The interpretation of the OISTR process induced by the pump pulse now makes this clear. OISTR initiates a non-equilibrium between the Ni and Fe subsystems via the transfer of minority spins on the very short timescale of the pump excitation. Subsequently, demagnetization occurs via the well-known spin-flip and exchange scattering processes, and both subsystems start to demagnetize at the same rate. At the time of the first experiment [29], the small increase due to OISTR in permalloy was not resolved, but the subsequent delayed behavior in the demagnetization of the Fe and Ni subsystems was clearly identified. However, for the reasons given above, we also revisit the delayed demagnetization of Ni and Fe and perform an energy-integrated analysis of $\mathrm{Re}(\epsilon_{xy})$. From this extended analysis, we still find a demagnetization delay in $Fe_{19}Ni_{81}$ of 12 ± 3 fs, while $Fe_{50}Ni_{50}$ actually shows both a transient increase in Ni and a relative delay of 95 ± 7 fs (cf. SI for more detail). We emphasize that it is really the stronger OISTR effect that enhances the delayed behavior, and not a modification of the exchange coupling that also influences the delayed behavior, as was previously observed for

permalloy alloyed with Cu [29].

In conclusion, we have carried out a combined experimental-theoretical analysis of the spin-transfer effect in Ni, $Fe_{19}Ni_{81}$, and $Fe_{50}Ni_{50}$. We have paid special attention to the observed increase and delay of the magnetic asymmetry in T-MOKE, which was found in the alloys, but also in pure Ni material. Through an extended analysis (see Ref. [63]), we are able to directly compare transient dynamics in the real part of the off-diagonal element of the dielectric tensor $\mathrm{Re}(\epsilon_{xy})$, which probes the spin polarization of the unoccupied states. Crucially, this procedure allows us to make a direct comparison with TDDFT theory calculations, which helps us to identify and elucidate all the observed signals. In summary, we verify OISTR in $Fe_{50}Ni_{50}$ and elucidate the origin of the previously found delays in these material systems.

5.1.3. Methods

EUV T-MOKE data for FeNi alloys and Ni

We measured the transient T-MOKE asymmetry for multiple incidence angles in order to be able to extract the transient off-diagonal tensor element $\mathrm{Re}(\epsilon_{xy})$. The reflected 100 kHz EUV probe beam spans energies between 30-72 eV. We estimate the resolution of the spectrometer to be better than 0.2 eV, while the photon energy calibration is accurate to $< 2\%$. Details on the angle-resolved measurement and analysis are given in Ref. [63], while general information on the experimental setup can be found in Ref. [102].

The experimental T-MOKE asymmetries and their dynamics for $Fe_{50}Ni_{50}$, $Fe_{19}Ni_{81}$ and Ni are shown in Supplementary Figure 1. Here, we pumped the samples with a 47 ± 5 fs pulses (Gauss FWHM) with a photon energy of 1.2 eV. The absorbed fluence is slightly different for each measurement: 0.8 ± 0.2 $\mathrm{mJ/cm^2}$ for Ni, 1.1 ± 0.2 $\mathrm{mJ/cm^2}$ for $Fe_{50}Ni_{50}$ and 0.8 ± 0.2 $\mathrm{mJ/cm^2}$ for $Fe_{19}Ni_{81}$.

5.1.4. Data availability

The data that support the findings of this study are available from the corresponding author upon reasonable request.

5.1.5. Acknowledgements

We thank Mario Fix and Manfred Albrecht from the University of Augsburg for the fabrication of the FeNi samples. We also thank Thomas Brede from the Institut für Materialphysik Göttingen for the fabrication of the Ni sample. This work was funded by the Deutsche Forschungsgemeinschaft (DFG, German Research Foundation) - project IDs 399572199 and 432680300/SFB 1456. G.S.M.J. acknowledges financial support by the Alexander von Humboldt Foundation. S.S. and

J.K.D. would like to thank the DFG for funding through project-ID 328545488 TRR227 (project A04).

5.1.6. Author contributions

G.S.M.J., M.R., D.S., S.S. and S.M. conceived the research. C.M., H.P., M.S. and M.B. carried out the measurements. C.M., H.P. and G.S.M.J. performed the data analysis. J.K.D. and S.S. performed the TDDFT calculations. All authors discussed the results. G.S.M.J., D.S. and S.M. were responsible for the overall project direction. C.M., H.P., G.S.M.J. and S.M. wrote the manuscript with contributions from all co-authors.

Supplementary Material

Supplementary Figure 5.6 shows the complete data sets that were used to fit Re(ϵ_{xy}).

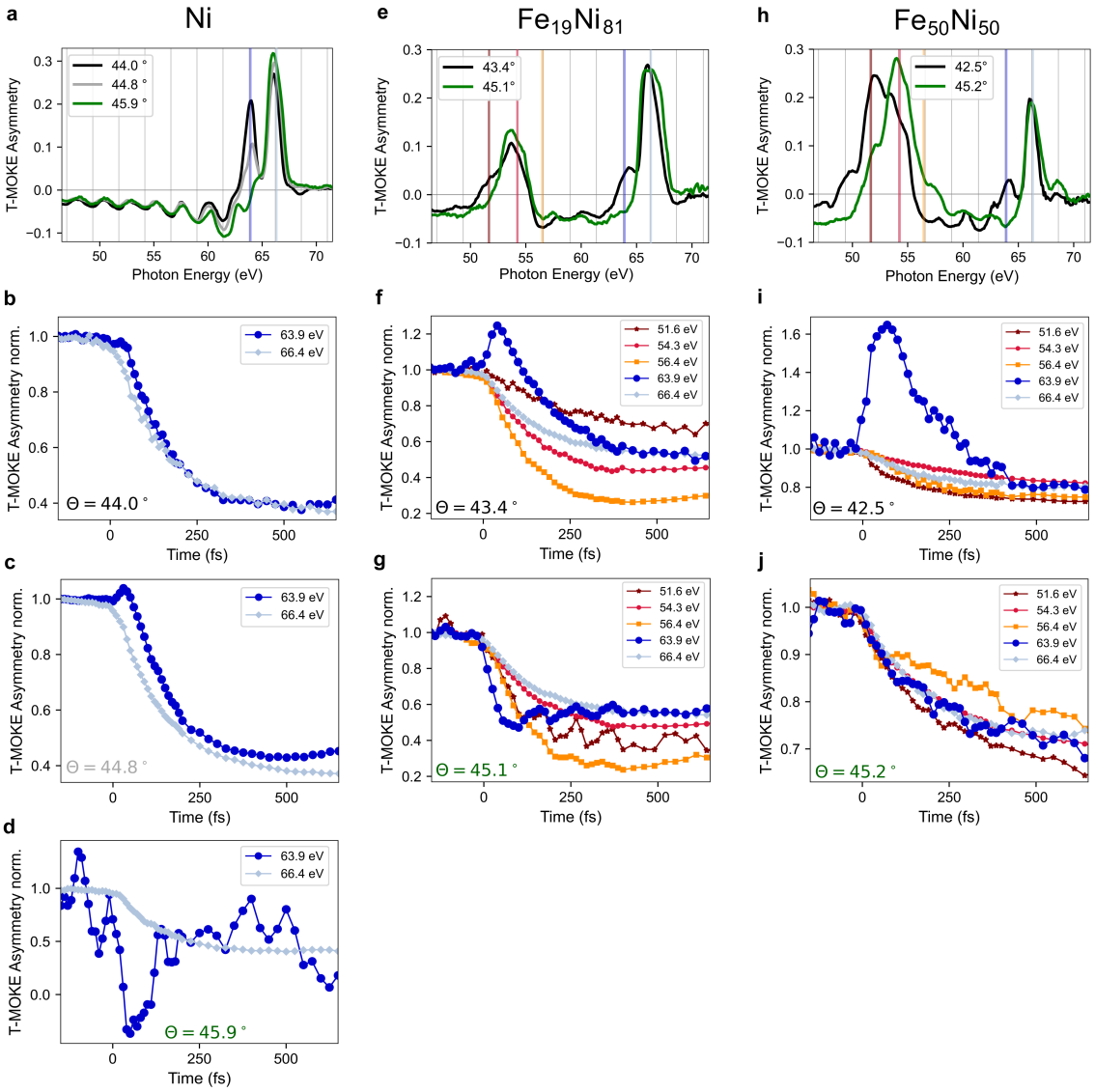

Figure 5.6.: All experimental results for Ni, $Fe_{19}Ni_{81}$ and $Fe_{50}Ni_{50}$. We measured the transient T-MOKE asymmetry for three different incidence angles for Ni (a-d), and for two different incidence angles for the two FeNi alloys (e-j). The asymmetry around 63.9 eV photon energy shows dramatically different dynamics for different incidence angles.

5.1.7. Delayed dynamics in FeNi alloys

In order to extract the relative demagnetization delay, we evaluate the FeNi asymmetries for large energy regions around the M edge, as has been done in earlier T-MOKE studies [29,41,42,102]. In contrast to the spectrally-resolved analysis in the main paper, we would call this an element-specific analysis of the data.

Supplementary Figure 5.7 shows the experimental transient evolution of the T-MOKE asymmetry in the marked energy regions. We note that the dynamics strongly differ for different incidence angles θ.

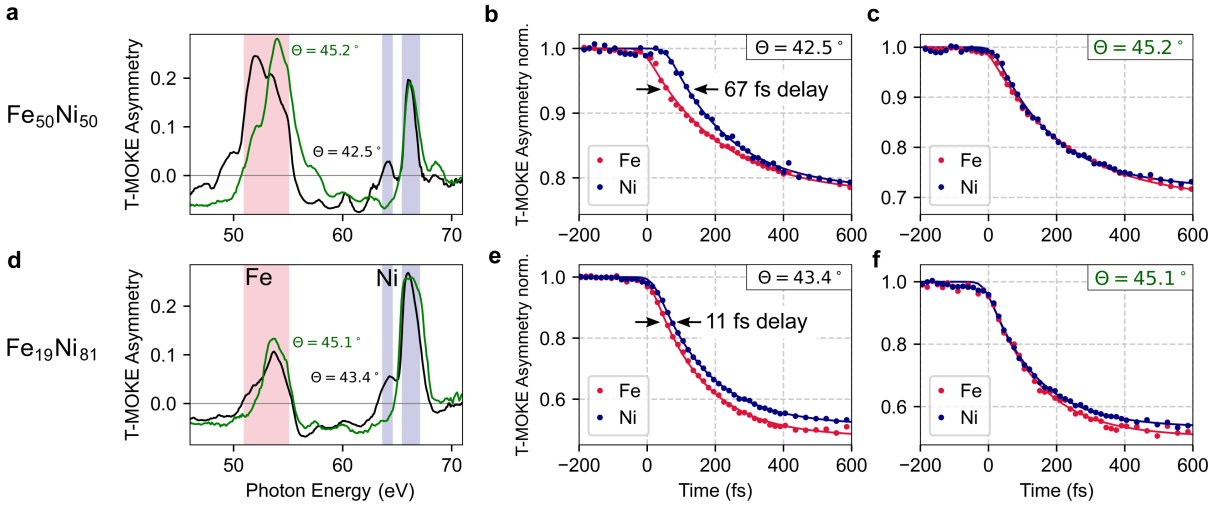

Figure 5.7.: Magnetic asymmetry for two incidence angles of a) $Fe_{50}Ni_{50}$ and d) $Fe_{19}Ni_{81}$. b), c), e) and f) Transient evolution of the magnetic asymmetry integrated in the marked energy regions around each absorption edge: Fe: 51 - 55 eV, Ni: 63.7 - 64.5 eV and 65.5 - 67 eV. We observe the delayed behavior of Ni compared to Fe at the smaller incidence angle [b) and e)], while there is no such delay present for the transient asymmetry measured at the larger incidence angle.

Integrating over extended energy regions results in a "mixing" of the spectral features: at the smaller incidence angle, the integral of the ultrafast increase around 64 eV and the decrease around 66 eV is measured. This leads to the previously reported delay of the ultrafast dynamics of Ni compared to Fe. In contrast, the delay in the energy-integrated signal vanishes at larger incidence angles, because the increase at $h\nu = 64$ eV is not present in the transient asymmetry (cf. Fig. 2 in the main text).

Therefore, the transient evolution of the T-MOKE asymmetry is not always a good indication of the magnetic moment and depends strongly on the incidence angle, as described in the previous section and in detail in Ref. [63]. In consequence, we performed an element-specific evaluation of the off-diagonal tensor element $\mathrm{Re}(\epsilon_{xy})$, which is shown in Supplementary Figure 5.8.

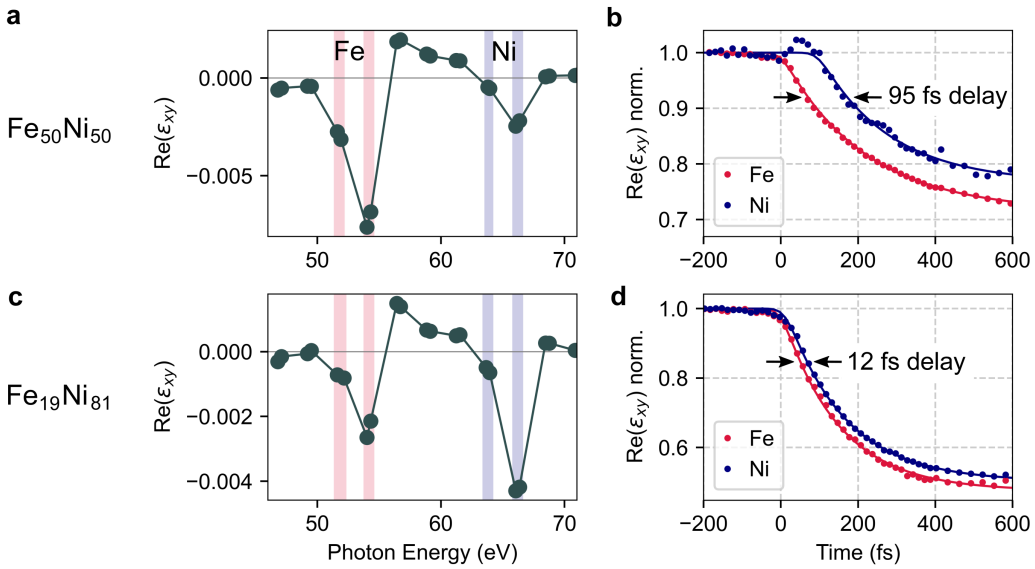

Figure 5.8.: a) Off-diagonal tensor element of $Fe_{50}Ni_{50}$ and c) $Fe_{19}Ni_{81}$. b) and d) Transient evolution of ϵ_{xy} integrated for multiple harmonics around each absorption edge: Fe: 51.6, 51.9, 54.0, and 54.3 eV; Ni: 63.6, 63.9, 66.1 and 66.4 eV.

We fitted the transient evolution of $\mathrm{Re}(\epsilon_{xy})$ with a simple exponential decay fit given by

$$\frac{A(t)}{A(t<t_0)} = G(t) \circledast \left[1 - \Theta(t-t_0) \cdot \Delta A_m \cdot \left(1 - e^{-\frac{t-t_0}{\tau_m}}\right)\right]. \tag{5.1}$$

Here, t_0 defines the onset of the dynamics, τ_m is the demagnetization constant, and ΔA_m is proportional to the maximum demagnetization. The fit results are shown in Table 5.1.7. We observe a delayed onset of the dynamics of $\mathrm{Re}(\epsilon_{xy})$ for Ni compared to Fe which amounts to 12 ± 3 fs for $Fe_{19}Ni_{81}$ and to 95 ± 7 fs for $Fe_{50}Ni_{50}$.

	$Fe_{50}Ni_{50}$		$Fe_{19}Ni_{81}$	
	Fe	Ni	Fe	Ni
t_0 (fs)	0 ± 2	95 ± 6	0 ± 2	12 ± 2
ΔA_m	0.286 ± 0.003	0.234 ± 0.008	0.525 ± 0.004	0.498 ± 0.004
τ_m (fs)	215 ± 6	184 ± 19	147 ± 4	153 ± 3

Table 5.1.: Fit results of the exponential fits to the transient evolution of $\mathrm{Re}(\epsilon_{xy})$ (Supplementary Figure 5.8) for Fe and Ni in both FeNi alloys.

5.1.8. TDDFT: OISTR and spin flips in FeNi

Fig. 5.9 shows the transient changes in the occupation of the minority and majority channels in $Fe_{50}Ni_{50}$ calculated by TDDFT. As expected, optical excitation with a 1.2 eV pump pulse will induce a decrease of carriers below the Fermi level and an increase above the Fermi level. The incident fluence is 18 $\mathrm{mJ/cm^2}$.

The optical intersite spin transfer (OISTR) can be seen by the strong loss of minority Ni carriers around 1 eV below E_F and by a strong increase of Fe minority carriers $\approx$ 1 eV above E_F. This process happens directly at the onset of the optical laser pulse (47 fs FWHM). At a time of t=120 fs we find that scattering processes already dominate the dynamics. Spin-orbit mediated spin flips below the Fermi level lead to the strong losses in the majority channel both for Ni and Fe.

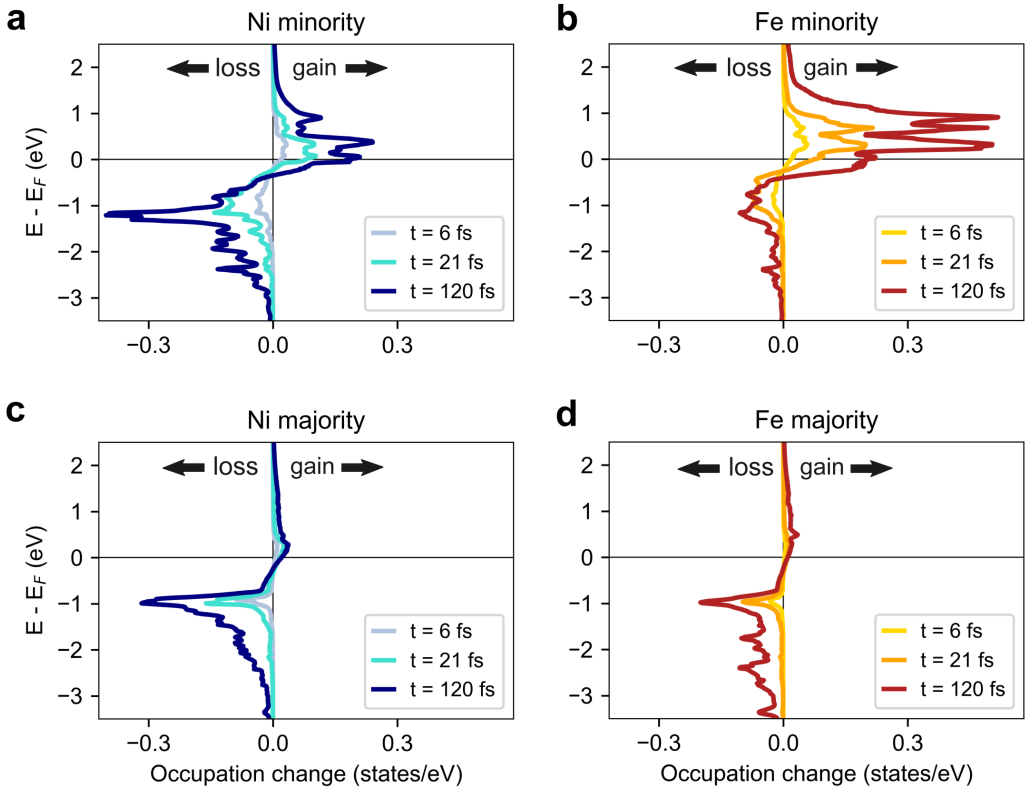

Figure 5.9.: TDDFT calculations of the transient occupation change in $Fe_{50}Ni_{50}$ for minority carriers (a) and (b) and majority carriers (c) and (d).

5.2. Why do the transient EUV T-MOKE asymmetries differ for different incidence angles?

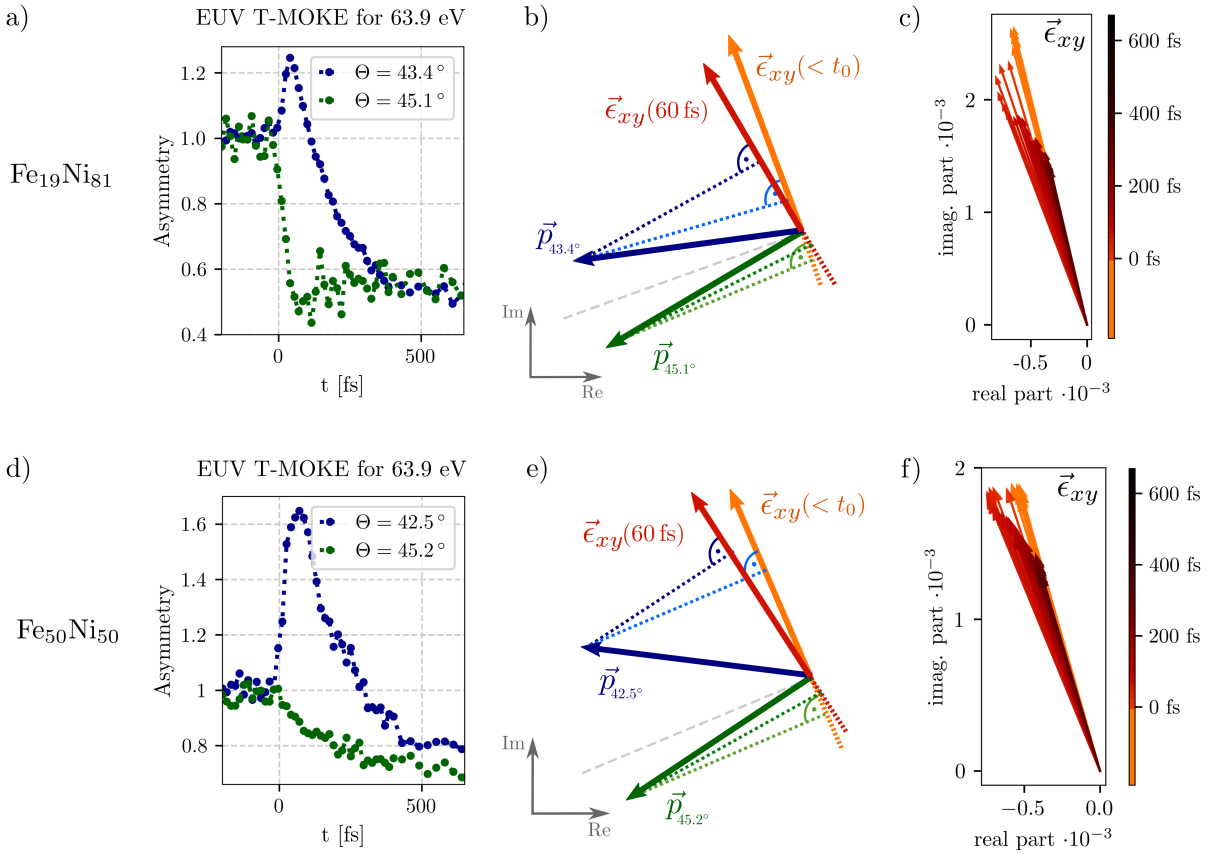

Figure 5.10.: a), d) Different dynamics of the experimental asymmetry for a photon energy of 63.9 eV for different incidence angles θ in our EUV T-MOKE setup. For the smaller incidence angle (blue curves) we observe a strong increase in the T-MOKE asymmetry for $Fe_{19}Ni_{81}$ and $Fe_{50}Ni_{50}$. In contrast, the measurements with a larger incidence angle (green curves) show a decreasing asymmetry. b), e) Schematic drawing of the $\vec{\epsilon}_{xy}$ vector and the probe vectors $\vec{p}$. The EUV T-MOKE asymmetry is the scalar product of both vectors. In the illustrated case, the rotation of the $\vec{\epsilon}_{xy}$ vector corresponds to a smaller projection of $\vec{p}$ on $\vec{\epsilon}_{xy}$ for the larger incidence angle (decrease in asymmetry), and to a larger projection of $\vec{p}$ on $\vec{\epsilon}_{xy}$ for the smaller incidence angle (increase in asymmetry). c), f) Extracted off-diagonal tensor element $\vec{\epsilon}_{xy}$ in the complex plane for different time delays. The fast rotation of the $\vec{\epsilon}_{xy}$ vector in combination with measurements at different incidence angles leads to the strikingly different dynamic behavior of the time-resolved T-MOKE asymmetry.

The main paper in section 5.1 already shows the previously unexpected distinct dynamics of the EUV T-MOKE asymmetry for different incidence angles (cf fig. 5.2 and 5.6). These mea-

surements were indeed alarming because exactly the increase of the asymmetry for 64 eV was interpreted as evidence for the first observation of OISTR in $Fe_{50}Ni_{50}$ by Hofherr et al. [31]. In the following section, the origin of the seemingly contradictory dynamics of the EUV T-MOKE asymmetry is explained in detail. An extensive discussion for the case of Ni is carried out in [63].

Consider measuring the time evolution of the T-MOKE asymmetry for $Fe_{19}Ni_{81}$ and $Fe_{50}Ni_{50}$ at a photon energy of 63.9 eV for two different incidence angles. Instinctively, one would expect identical dynamics when *only* the incidence angle is modified and all other parameters remain unchanged. However, surprisingly, we see different dynamics for different incidence angles (blue and green) as depicted in figure 5.10 a) and d). For the smaller incidence angle we measure an increase of the T-MOKE asymmetry for both samples, which has also been reported by Hofherr et al. [31]. In contrast to this, an initially unexpected decrease of the asymmetry is observed for the larger incidence angle for both materials.

This observation of different dynamics for different incidence angles can be explained as follows. Varying the incidence angle in EUV T-MOKE does not affect the off-diagonal tensor element $\vec{\epsilon}_{xy}$ itself because the dielectric tensor is a universal quantity. Different incidence angles correspond to a different orientation of the so-called probe vector $\vec{p}$ in the complex plane as shown in figure 5.10 b) and e). The relative orientation of $\vec{\epsilon}_{xy}$ to the probe vector $\vec{p}$ is important for EUV T-MOKE as already described in section 3.4. We can express the measured asymmetry A as the scalar product of the $\vec{\epsilon}_{xy}$ and the $\vec{p}$ vector:

$$\begin{aligned} A &\approx \frac{2\mathrm{Re}(R_0^* R_m \epsilon_{xy})}{|R_0|^2} \\ &= \vec{p} \cdot \vec{\epsilon}_{xy} \\ &= |\vec{p}| \cdot |\vec{\epsilon}_{xy}| \cdot \cos(\sphericalangle(\vec{p}, \vec{\epsilon_{xy}})), \end{aligned} \tag{5.2}$$

where the probe vector $\vec{p}$ depends on the incidence angle θ and the optical refractive index n_0.

Different angles of incidence and, thus, different probe vectors change the value of the static EUV T-MOKE asymmetry for specific photon energies (see figure 3.8 in section 3.4). The question now is, how does this angle affect the measured transient dynamics of the asymmetry?

Fig. 5.10 b) and e) show the interesting arrangement of the two probe vectors $\vec{p}$ and the $\vec{\epsilon}_{xy}$ vector for the photon energy of 63.9 eV. Both probe vectors have an angle close to 90° to $\vec{\epsilon}_{xy}$. A change in angle due to a rotation of one of the vectors will, therefore, have an enormous effect on the magnetic asymmetry due to the cosine function in equation (5.2). This effect is reversed depending on whether the angle is greater or less than 90°, which is exactly the case in our scenario. Our new analysis indeed reveals a rotation of the $\vec{\epsilon}_{xy}$ vector, see fig. 5.10 c) and f).

For the smaller incidence angle of 43.4°, the counterclockwise rotation of $\vec{\epsilon}_{xy}$ leads to a larger

projection of $\vec{p}$ onto $\vec{\epsilon}_{xy}$ and, thus, an increase in the asymmetry, even if the length of the $|\vec{\epsilon}_{xy}|$ stays constant or decreases slightly. In the case of the other probe vector $\vec{p}_{45.1^\circ}$ (shown in green in Fig. 5.10 b)), the counterclockwise rotation of $\vec{\epsilon}_{xy}$ leads to a smaller projection of $\vec{p}$ onto $\vec{\epsilon}_{xy}$, which corresponds to the decrease of the T-MOKE asymmetry.

Note that a rotation of the probe vector $\vec{p}$ caused by transient refractive index changes can have the same effect on the measured EUV T-MOKE data. With our new fitting routine, we can distinguish between magnetic and non-magnetic effects, namely the rotation of the off-diagonal tensor element $\vec{\epsilon}_{xy}$ and the rotation of the probe vector $\vec{p}$.

Our analysis reveals that the rotation of the off-diagonal tensor element $\vec{\epsilon}_{xy}$ is much larger than the rotation of the probe vector $\vec{p}$, see figure 5.11. For $Fe_{19}Ni_{81}$ at 63.9 eV, the off-diagonal tensor element $\vec{\epsilon}_{xy}$ rotates by 7° while the probe vectors for both angles rotate by 0.16° only. The length of both vectors also affects the measured asymmetry and is shown in figure 5.11 b) and d). The decrease of $|\vec{\epsilon}_{xy}|$ dominates the dynamics and the length of the prefactors only changes less than 1 %. A change in the length of the vectors cannot lead to the different dynamics of the EUV T-MOKE asymmetry. Instead, the rotation of the $\vec{\epsilon}_{xy}$ vector in the complex plane and an angle around 90° between $\vec{\epsilon}_{xy}$ and $\vec{p}$, in combination with the cosine function in equation (5.2) lead to the unexpected distinct dynamics for the EUV T-MOKE asymmetry (cf. fig. 5.10 a) and d)).

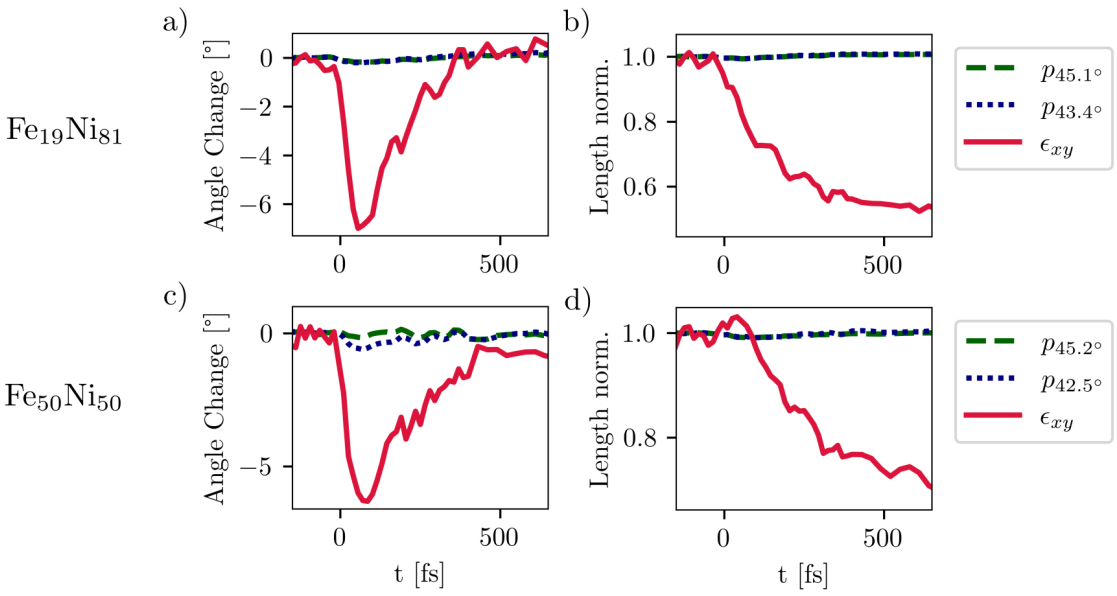

Figure 5.11.: Comparison of the rotation of the $\vec{\epsilon}_{xy}$ and $\vec{p}$ vectors in the complex plane for $Fe_{19}Ni_{81}$ a) and $Fe_{50}Ni_{50}$ c) for a photon energy of 63.9 eV. Normalized length of these vectors after the optical excitation in b) and d). The rotation of the off-diagonal tensor element $\vec{\epsilon}_{xy}$ is much larger than the rotation of the probe vector $\vec{p}$.

5.3. Ultrafast spin transfer and refractive index changes

In the main paper (section 5) we focused on the dynamics of the off-diagonal tensor element ϵ_{xy}. In the following, we clarify whether the diagonal element ϵ_{xx} changes in the presence of ultrafast spin transfer. We expect strong charge dynamics for the photon energies relevant to OISTR, because they correspond to energies around the Fermi level where strong changes in the electronic occupation occur. This section shows that we can cross-check the refractive index changes predicted by our new dielectric tensor fitting routine with an independent measurement of the s-polarized reflectivity.

Due to the strong optical excitation, the OISTR feature in the off-diagonal tensor element ϵ_{xy} at 2.1 eV below the Ni edge should be accompanied by a fast increase in the optical absorption, which is described by the imaginary part β of the refractive index $n_0 \equiv 1 - \delta + i\beta = \sqrt{\epsilon_{xx}}$. In our extended analysis of the T-MOKE data, we are able to extract the transient change of the refractive index, which allows us to quantify the changes in the optical absorption, cf. Fig. 5.12 c) and f). In our analysis, the optical absorption β increases by 0.9% for $Fe_{50}Ni_{50}$ and by 1.6% for $Fe_{19}Ni_{81}$ at a photon energy of 63.9 eV. There is a strong loss of minority (and majority) carriers in Ni below the Fermi edge which increases the absorption of EUV light (driving transitions from the 3p core levels to newly available states below the Fermi level), cf. TDDFT calculations in Fig. 5.9. The expected coexistence of the OISTR feature and a strong charge response can also be found in Tengdin et al. [30] for the optical intersite spin transfer in Co_2MnGe.

An indication for a strong optical response can also be seen in the symmetric or asymmetric behavior of the transient reflected intensity curves $I_{\uparrow/\downarrow}$ (see section 3.5). Here, $I_\uparrow$ is intensity of the reflected p-polarized EUV light for one magnetic field direction and $I_\downarrow$ for the other magnetic field direction:

$$I_{\uparrow/\downarrow} = I_0 \cdot \left[|R_0|^2 + |R_m \epsilon_{xy}|^2 \pm 2\mathrm{Re}(R_0^* R_m \epsilon_{xy}) \right], \tag{5.3}$$

where R_0 and R_m are functions of the refractive index n_0 and the incidence angle θ.

The measured intensity curves are shown for two photon energies in Fig. 5.12 a) and 5.12 d). For the photon energy of 63.9 eV (dark blue), $I_\uparrow$ and $I_\downarrow$ are asymmetric around the $I = 0.5$ axis and both curves increase after the optical excitation (orange arrows). This is a strong indication for an optical refractive index change because both curves increase, which is caused by a purely optical increasing $|R_0|^2$ term (if $|R_m \epsilon_{xy}|^2 \ll |R_0|^2$). In contrast, the reflectivity at a photon energy of 66.1 eV shows a symmetric behavior (green arrows), where $I_\uparrow$ decreases and $I_\downarrow$ increases, which indicates a purely magnetic signal. Note that the asymmetric behavior of $I_{\uparrow/\downarrow}$ can only be reproduced with our fit when optical index changes are taken into account (see figure 3.12 in section 3.5).

Therefore, we can extract the transient dynamics of the off-diagonal tensor element ϵ_{xy} (fig. 5.12 b) and 5.12 e)) and the refractive index n_0 (fig. 5.12 c) and f)). As expected by the asymmetric

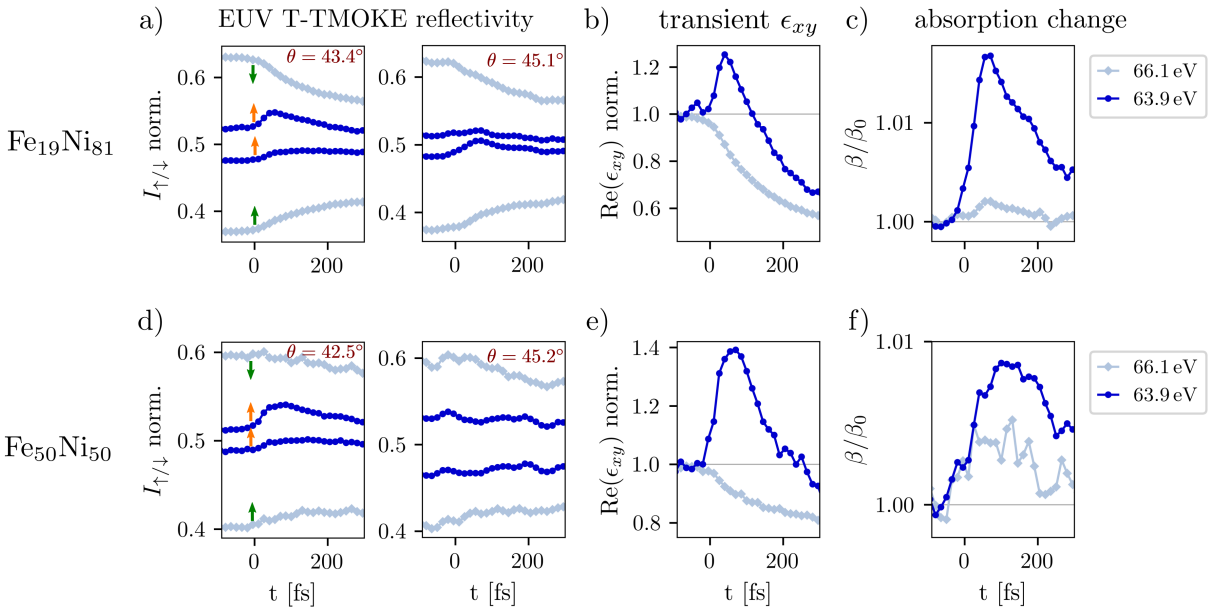

Figure 5.12.: Experimental data for the reflected intensity curves for $Fe_{19}Ni_{81}$ (a) and $Fe_{50}Ni_{50}$ (d) for two incidence angles and two photon energies around the Ni edge. A symmetric behavior of the reflected intensities $I_\uparrow$ and $I_\downarrow$ around the $I = 0.5$ axis can be found for the photon energy of 66.1 eV (light blue). Because $I_\uparrow$ decreases and $I_\downarrow$ increases (cf. green arrows), this is an indication for a purely magnetic signal. For a photon energy of 63.9 eV (dark blue), the $I_\uparrow$ and $I_\downarrow$ both increase (orange arrows) – the curves are not symmetric around the $I = 0.5$ axis. Thus, we conclude that the optical term $|R_0|^2$ also transiently changes for this EUV photon energy. Here, the measured reflected intensity curves are normalized to their sum before time zero $\frac{I_{\uparrow/\downarrow}(E,t)}{I_\uparrow(E,t_0)+I_\downarrow(E,t_0)}$ because the incident light intensity I_0 (before the sample) is strongly photon energy dependent and cannot be measured in our setup. b), e) Transient evolution of the off-diagonal tensor element. c), f) Change in imaginary part of the refractive index β indicating a strong change for 63.9 eV. This increase in absorption leads to the asymmetric shape of the reflected intensity curves in a) and d). Note that the refractive index change in both FeNi alloys may not be compared quantitatively because of different incident fluences and different demagnetization quenchings.

$I_{\uparrow/\downarrow}$ curves, the optical absorption (β) increases for the photon energy of 63.9 eV, which leads to the increase of both $I_\uparrow$ and $I_\downarrow$.

As a cross-check, we can compare the transient dynamics in the optical absorption from the ϵ_{xy} analysis with an independent measurement of the s-polarized reflectivity, which must also reflect the transient refractive index changes (cf. Fig 5.13). For s-polarized light the reflection

coefficient does not depend on the magnetization of the sample

$$R_{0,s} = \frac{\cos(\theta) - n_0\sqrt{1 - \frac{\sin^2(\theta)}{n_0^2}}}{\cos(\theta) + n_0\sqrt{1 - \frac{\sin^2(\theta)}{n_0^2}}}.$$

The experimental s-polarized reflectivity for $Fe_{19}Ni_{81}$ is shown in figure 5.13 b) in comparison to the reflectivity change which is predicted by our fit to the experimental p-polarized EUV T-MOKE data (fig. 5.13 a)). Qualitatively the dynamics for the different photon energies are reproduced well by our fit. The magnitude of the reflectivity change for the photon energy of 63.9 eV is underestimated by our fit. The overall stronger reflectivity change may possibly result from hot carrier dynamics in Si_3N_4 or from the fact that we use literature values for the refractive index before time-zero in our analysis and that we neglect any depth dependence of the pump pulse.

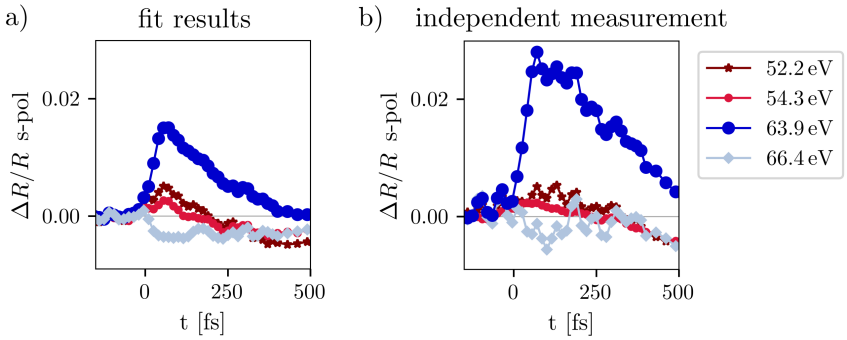

Figure 5.13.: Our analysis of the EUV T-MOKE data also reveals the non-magnetic component of the time-resolved dielectric tensor. The transient changes of the refractive index lead to a reflectivity change for s-polarized light. Here, we compare the predicted reflectivity change from our fit for $Fe_{19}Ni_{81}$ (a) with an independent measurement of the s-polarized reflectivity (b).

We can conclude that the expected change in optical absorption β for the OISTR transitions is indeed verified by an independent reflectivity measurement of s-polarized light.

6

Conclusion and outlook

The results reported in this thesis are threefold: First, we implemented a new EUV T-MOKE setup with a high harmonic source based on a high repetition laser system. The second contribution is the expansion of the EUV T-MOKE technique to capture the dynamics of the full dielectric tensor [63]. By measuring the T-MOKE response for different incidence angles and implementing a new fitting routine to the data we can fully disentangle the optical and magnetic contributions to the signal. The third contribution consists of the verification of the optical intersite spin transfer from Ni to Fe in two FeNi alloys through a thorough analysis of the spin dynamics in these systems.

The build-up of the experiment, the measurements, the data analysis and interpretations were carried out by the T-MOKE team with the main contributions from Henrike Probst and myself. The specific contributions are listed at the beginning of the respective chapters.

Here, I summarize the overall results of our work and discuss possible future steps and challenges ahead.

EUV T-MOKE setup We have presented our new EUV T-MOKE setup using a table-top high harmonic source with a photon energy range of 30 to 72 eV. High harmonic generation has the great advantage of generating multiple EUV wavelengths that all probe the samples' magnetic state within the same pump-probe event. In contrast, alternative EUV sources such as femtoslicing synchrotrons and free electron lasers require energy scanning to retrieve energy-resolved data.

Our fiber-laser-driven high harmonic source operates at a higher repetition rate of 100 kHz compared to other EUV T-MOKE setups [42, 100, 101, 147]. The high repetition rate and the intrinsic stability of the fiber laser result in a good signal-to-noise ratio, as EUV sources in general have quite high inherent intensity fluctuations.

Additionally, the specific properties of our setup – high magnetic fields up to 0.86 T and cooling of the sample down to 10 K – enabled us to investigate perovskite magnanite thin films in the ferromagnetic state. This class of materials is a promising candidate for unusual ultrafast spin dynamics due to the strong correlations between charge, lattice and spin degrees of freedom

[126–128]. Visible light reflectivity studies on different perovskites show a dynamical spectral weight transfer of magnetic origin [148–151]. According to Pincelli et al. [152], the MOKE signal on the ultrashort timescale is influenced by the charge dynamics. Thus, an element-resolved study with EUV T-MOKE in combination with our new analysis could disentangle the magnetic and optical contribution and shine further light on the ultrafast spin dynamics in perovskites.

Another key feature is the precise control of the angle of incidence on the sample, which is crucial for the experimental results presented on the two FeNi alloys. Moreover, the option to measure the EUV reflectivity changes of our samples using s-polarized light allows us to measure refractive index changes after the optical excitation. This makes it possible to compare the results of the refractive index change of our new ϵ_{xy} analysis with an independent measurement.

Further improvements to the current setup are conceivable. For example, our data quality would benefit from the implementation of a reference spectrometer, as, e.g., done by Johnson et al. [101] and Hennecke et al. [100], which helps to correct for intensity fluctuations of the EUV light. Such an approach works by splitting the EUV beam into two parts before the sample, either with a toroidal grating and its zeroth and first order reflections, or with a thin membrane placed at a certain angle in the beam. The spectrum of the light not hitting the sample is recorded with a CCD camera and serves as a reference spectrum. Figure 6.1 shows an innovative implementation of the reference spectrometer by Abel et al. [153] who place the membrane to split the EUV beam directly in front of the sample such that the same CCD camera for both EUV spectra can be used. For this geometry, of course, a clever realization must be found to incorporate the pump beam. Moreover, Heinrich et al. [154] combined the recorded reference spectrum with machine learning algorithms to impressively eliminate source noise from the transient EUV absorption spectroscopy data.

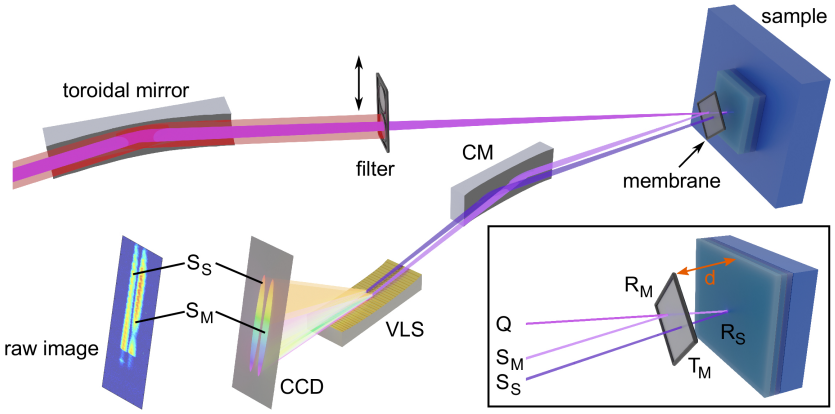

Figure 6.1.: Membrane in front of the sample to get an EUV reference spectrum inside the same spectrometer. Reprinted from Ref. [153], used here in accordance with the *Creative Commons Attribution License 4.0* (CC BY 4.0).

A more continuous EUV spectrum would allow to probe the magnetization of the sample with more densely spaced photon energies. To obtain a more contiunous EUV spectrum, at least two options exist: Either the generation of much shorter driving pulses (e.g. 10 fs) using a second hollow core fiber compression stage [155] or the implementation of a two-color high harmonic generation scheme [156] to generate not only the odd, but also the even harmonics of the fundamental laser beam. Regarding the latter, we already started to build an inline-device between focusing lens and generation point similar to Kfir et al. [157], but further improvements to get both pulses (1030 nm and 515 nm) without any time delay at the same focus position would be necessary.

Dielectric tensor from EUV T-MOKE data The first research question raised in the introduction was "How can we interpret the measurement signal in EUV T-MOKE?". The EUV T-MOKE asymmetry for one photon energy is *not* directly proportional to the magnetization. The magnetization describes the difference in majority and minority spins summed up for all energies. Earlier EUV T-MOKE studies such as [31] associated the asymmetry at a specific photon energy to the energy resolved magnetic moment at a specific energy around the Fermi level by subtracting the respective M edge energy. This interpretation is too simplified for two reasons (see figure 6.2). First, the asymmetry is linked via a scalar product to the off-diagonal tensor element ϵ_{xy}, so that changes in the asymmetry are not necessarily linked to changes in the real part of ϵ_{xy} (see section 3.4 and 5.2). Second, the off-diagonal tensor element ϵ_{xy} for a specific photon energy represents multiple transitions from the broad 3p core levels to different final states in the 3d bands. Thus, ϵ_{xy} for a specific photon energy gives a broadened view on the imbalance between majority and minority carriers. Advanced theory, as, e.g., time-resolved density functional theory (TDDFT) is needed to interpret the dynamics of ϵ_{xy} in terms of the transient spin resolved occupation in a specific material.

As part of our joint publication [63], a fitting routine for angle- and time-resolved EUV T-MOKE data was developed to extract the full transient dielectric tensor. The dependence of the T-MOKE asymmetry on the incidence angle θ (via the probe vector $\vec{p}$) allowed us to fit either the magnetic asymmetry or the reflected intensity for both magnetic field directions $I_{\uparrow/\downarrow}$. This new method should be applicable in already existing EUV T-MOKE setups because only a small range of incidence angles (2.5° in our case) has to be scanned. With our approach, we not only reconstruct the off-diagonal element ϵ_{xy} of the dielectric tensor, but also the on-diagonal element ϵ_{xx}. This method disentangles the magnetic and optical contributions to the signal, which is also a great advantage compared to earlier studies [52, 70].

The transient dielectric tensor can also be calculated with TDDFT. Hence, a direct comparison of the same quantity between experiment and theory via our new approach and TDDFT is now possible. In earlier works less immediate comparisons were made in magneto-optical spectroscopy . For example, Siegrist et al. [12] compare the experimental transient EUV MCD signal

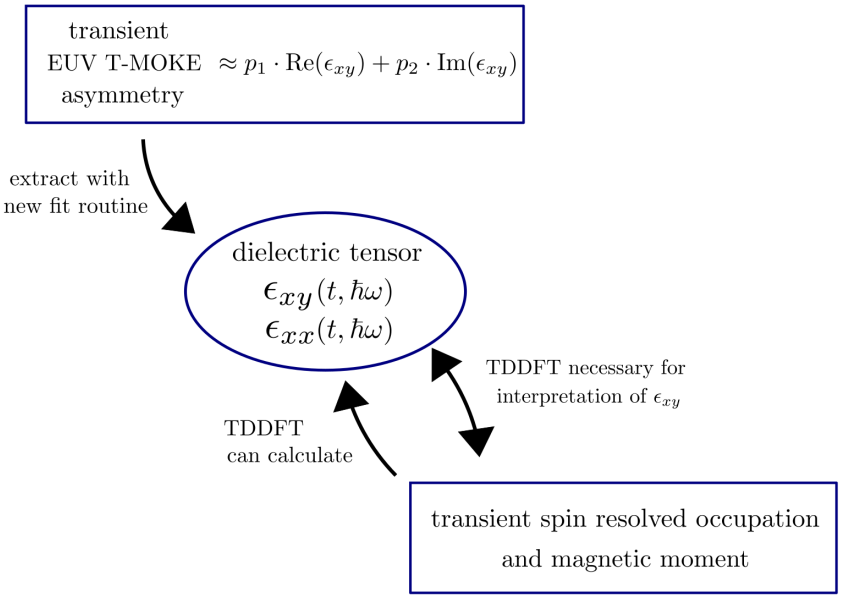

Figure 6.2.: Connection between the EUV T-MOKE asymmetry and the spin-resolved occupation via the dielectric tensor.

with the theoretical transient magnetic moment. Hofherr et al. [31] compare the experimental transient EUV T-MOKE asymmetry for specific photon energies with the element-specific transient spin polarization for specific energies around the Fermi level.

For the reconstruction of the dielectric tensor in chapter 5 we used tabulated values for the complex refractive index as an input for the fit. Ideally, the refractive index in the EUV was determined experimentally for the specific sample under investigation. In the future, it would be very helpful to build a new setup for these measurements or to collaborate with existing experiments that can measure the refractive index in the EUV. One method to do so is angle-resolved reflectometry, where the reflectance of a thin film is measured at different incidence angles [158–160]. By fitting the obtained data to an appropriate model, film parameters like the complex refractive index, density, thickness, and roughness can be determined. Another way is to measure the photoabsorption, namely the transmittance of the EUV light through a very thin film, and to employ the Kramers Kronig relation to obtain the dispersive part of the complex refractive index [161, 162]. More recent measurements are based on interferometry of which there are two versions: Either parts of the same EUV beam pass through the thin film while the rest is the reference wave [163] or two independently generated but phase-locked EUV beams interfere with a variable delay (Fourier transform spectroscopy) [164].

Since different magneto-optical techniques like MCD and EUV T-MOKE can be used to probe similar quantities, there is much to be learned from the comparison of different experimental techniques. A promising starting point could be a comparison of the transient response after ultrafast excitation from different measurement techniques using the same pump pulses and the same samples. A joint work in combination with TDDFT could shine light on different sides of

the same coin. For example, the observed redshift of the MCD spectra in Hennes et al. [89] below the M edge for pure nickel is similar to our experiments on nickel published in [63]. We observe a small increase in the off-diagonal tensor element ϵ_{xy} during the optical excitation for photon energies below the M edge indicating a larger loss of minority than majority carriers below the Fermi level. Hennes et al. attribute the red shift to changes in the electron occupation, namely a depletion of electrons below the Fermi energy. Our interpretation in [63] aligns well with this observation.

Spin transfer in FeNi alloys The optical intersite spin transfer (OISTR) describes the excitation of spins from one atomic species to another in an alloy or multilayer. The question "Does (strong) optical intersite spin transfer exist in FeNi alloys?" is addressed in this thesis by measuring the ultrafast dynamics of the EUV T-MOKE asymmetry in $Fe_{50}Ni_{50}$, which initially seems to be in partial contrast to the measurements by Hofherr et al. [31]. Depending on the incidence angle, we find an increase or decrease of the asymmetry for the photon energy of 64 eV exactly where the increase for this photon energy was interpreted as evidence for optical intersite spin transfer in Hofherr et al. We were able to trace the origin of the observed different dynamics to the rotation of the $\vec{\epsilon}_{xy}$ vector in the complex plane in combination with angles close to 90° between $\vec{\epsilon}_{xy}$ and the different probe vectors $\vec{p}$.

With our new approach to reconstruct the full dielectric tensor, we were able to find signatures of optical intersite spin transfer in $Fe_{50}Ni_{50}$ and $Fe_{19}Ni_{81}$. The off-diagonal tensor element ϵ_{xy} increases for the photon energy of 64 eV after the optical excitation. With the help of TDDFT we can associate this increase of ϵ_{xy} to the loss of minority carriers in nickel below the Fermi level. We do not observe the fast decrease of ϵ_{xy} for photon energies above the iron M edge (corresponding to the gain of minority spins in iron above E_F) as we do not have enough photons in the spectral region of interest.

We are able to make a quantitative comparison between the strength of the OISTR signature in ϵ_{xy} for the photon energy of 64 eV in $Fe_{50}Ni_{50}$, $Fe_{19}Ni_{81}$ and pure nickel. Our experimental data of ϵ_{xy} agree with the dynamics of ϵ_{xy} calculated by TDDFT and show a stronger increase of ϵ_{xy} for $Fe_{50}Ni_{50}$ than for $Fe_{19}Ni_{81}$ than for pure Ni. Thus, the OISTR-relevant transition (from Ni to Fe) that leads to the loss of minority Ni electrons below E_F is more efficiently excited in $Fe_{50}Ni_{50}$ than in $Fe_{19}Ni_{81}$. This is in line with density functional theory calculations by Minar et al. [143], who predict a larger projected density of states of Fe above the Fermi level in $Fe_{50}Ni_{50}$ enhancing the optical intersite spin transfer.

The observation of optical intersite spin transfer in FeNi alloys is directly linked to the long-lasting debate on the delay between nickel and iron found by Mathias et al. [29] in 2012. Radu et al. [38] and Eschenlohr [39] did not observe a delayed behavior in FeNi using tr-XMCD. However, a recent study by Jana et al. [40], also using time-resolved X-ray magnetic circular dichroism (XMCD) experiments at the L-edges, confirms the delay between Ni and Fe. In

these new measurements an x-ray optical cross correlator (XOCC) as a unique time reference to obtain a common time axis for the measurements at both edges was used. Note that the early experiments by Radu and Eschenlohr did not have this capability, so that an independent determination of time zero for the different photon energies at the Fe and Ni L edge was not possible. Instead, both datasets were shifted manually in time, which makes it impossible to measure a delay between both curves.

In this thesis, we experimentally observed the delay between nickel and iron in FeNi alloys in the energy-integrated off-diagonal tensor element ϵ_{xy}. When only looking at the EUV T-MOKE asymmetry, one has to measure at a specific incidence angle to measure such delayed behavior (cf. figure 5.7 in section 5.1.6), otherwise it is not present. Regarding the last research question from the introduction "What is the microscopic origin of the controversially discussed delayed demagnetization of Fe and Ni in FeNi alloys?", we conclude that the delay originates from the optical intersite spin transfer. OISTR initiates a non-equilibrium between the Ni and Fe subsystems via the transfer of minority spins on the very short timescale during the optical excitation. Subsequently, demagnetization takes place through spin flips and exchange scattering processes, resulting in both subsystems demagnetizing at a comparable rate. The increase of ϵ_{xy} at a photon energy of 64 eV (associated with the loss of Ni minority spins below E_F due to OISTR) is the main reason of the delayed behavior of nickel in the energy-integrated signal where the increase for 64 eV and the decrease for 66 eV are mixed. Thus, the delay is also significantly larger in $Fe_{50}Ni_{50}$ with 95 fs compared to 12 fs in $Fe_{19}Ni_{81}$, which fits well to the stronger OISTR effect in $Fe_{50}Ni_{50}$.

In future research, it would be great to detect the specific signature of OISTR in the Fe signal, which was not possible in our work due to the low number of photons in the relevant spectral region. More generally, a continuous EUV spectrum would allow to measure the fingerprints of specific microscopic effects in the transient off-diagonal tensor element, which potentially are only present in small energetic regions.

In earlier measurements on $Fe_{19}Ni_{81}$, we found a dependence of the time delay between Ni and Fe on the sample temperature. Figure 6.3 shows the transient dynamics of the EUV T-MOKE asymmetry (at one specific angle of incidence) for sample temperatures of 50 K (b), 175 K (d) and 400 K (f). The delay seems to increase for lower sample temperatures. Of course, a sophisticated study measuring at multiple incidence angles and extracting the off-diagonal tensor element is necessary in the future to verify and further investigate this observation. However, in his thesis, Bobowksi [165] suggests that optical intersite spin transfer should have a stronger effect at lower temperatures because the excited carriers already have a higher spin polarization. It would be very interesting to study the effect of the sample temperature on the presence of OISTR in more detail, e.g., by using FeNi alloys diluted with Cu (cf. Mathias et al. [29]), which have a significantly lower Curie temperature of ≈ 400 K which is accessible with our EUV T-MOKE setup.

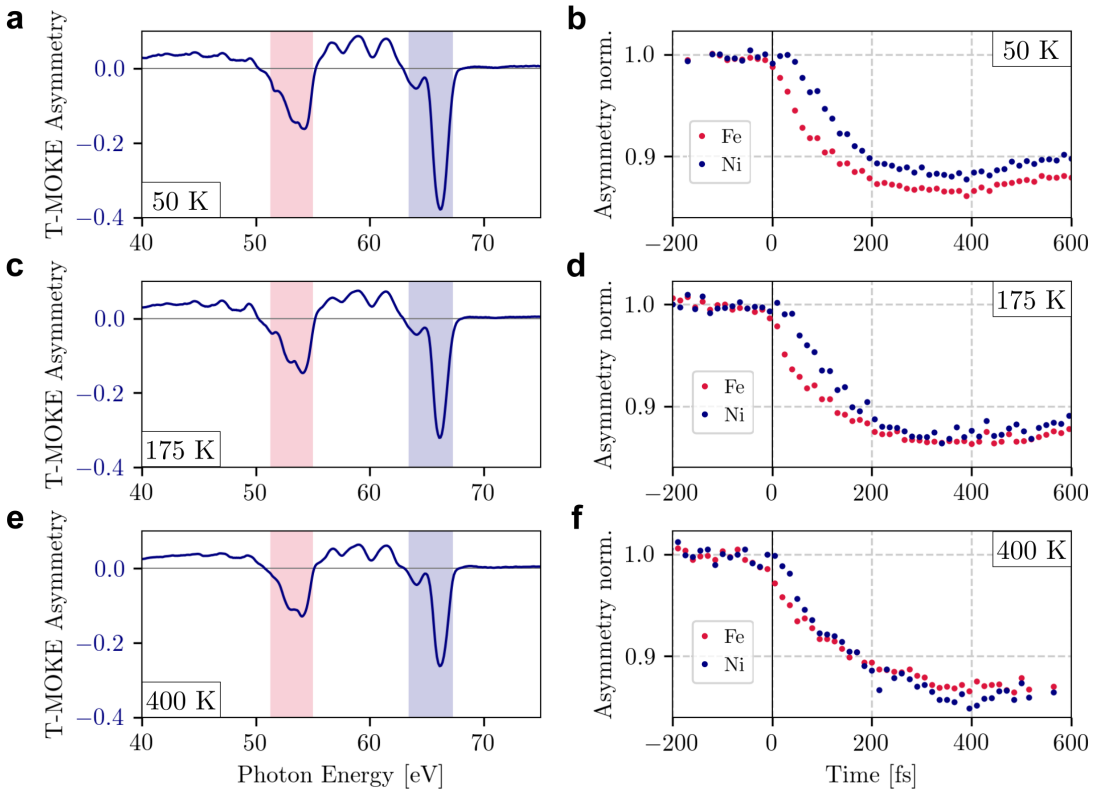

Figure 6.3.: Static EUV T-MOKE asymmetries for different sample temperatures of 50 K (a), 175 K (c) and 400 K (e) for the same angle of incidence. b), d) and f) show the corresponding transient asymmetries evaluated in large energy regions around the M edges of Fe and Ni: 51.4 - 54.9 eV for Fe and 63.5 - 67.2 eV for Ni.

Overall, we were able to show that the optical intersite spin transfer in FeNi alloys is real and thus explain the origin of the delay between nickel and iron. We found that the relationship between the EUV T-MOKE measurement signal and the dielectric tensor is more complex. The combination of our angle-resolved EUV T-MOKE setup and the new approach to reconstruct the full dielectric tensor paves the way to study the spin dynamics of many interesting multilayers and complex alloys.

A

Appendix

A.1. List of publications

Publications directly related to this thesis

- C. Möller, H. Probst, J. Otto, et al. Ultrafast element-resolved magneto-optics using a fiber-laser-driven extreme ultraviolet light source. *Review of Scientific Instruments*, 92(6):065107, 2021
- C. Möller, H. Probst, G. S. M. Jansen, et al. Verification of ultrafast spin transfer effects in FeNi alloys. `arXiv:2306.02793 [cond-mat.mtrl-sci]`, 2023
- H. Probst, C. Möller, M. Schumacher, et al. Unraveling femtosecond spin and charge dynamics with EUV T-MOKE spectroscopy. `arXiv:2306.02783 [cond-mat.mtrl-sci]`, 2023

Further publications

- M. Keunecke, C. Möller, D. Schmitt, et al. Time-resolved momentum microscopy with a 1 MHz high-harmonic extreme ultraviolet beamline. *Review of Scientific Instruments*, 91(6):063905, 2020
- G. S. M. Jansen, M. Keunecke, M. Düvel, C. Möller, et al. Efficient orbital imaging based on ultrafast momentum microscopy and sparsity-driven phase retrieval. *New Journal of Physics*, 22(6):063012, 2020
- M. Keunecke, M. Reutzel, D. Schmitt, A. Osterkorn, T. A. Mishra, C. Möller, et al. Electromagnetic dressing of the electron energy spectrum of Au(111) at high momenta. *Phys. Rev. B*, 102:161403, 2020

A.2. FeNi measurements details and ϵ_{xy} analysis

All parameters specific to the measurements on $Fe_{19}Ni_{81}$ (see figure 5.6) are described in table A.1. The same is presented in table A.3 for $Fe_{50}Ni_{50}$. The vacuum conditions in the different vacuum chambers (see section 4.1) for these measurements are given in table A.2.

	$Fe_{19}Ni_{81}$	
	M09 - 19.07.2022	M14 - 18.07.2022
	$\theta = 45.1°$	$\theta = 43.4°$
pump pulse at sample	1030 nm, p-pol , 43 fs sech^2, 100 kHz, 540 mW, $650 \times 550\,\mu m^2$	
absorbed pump fluence	0.83 mJ/cm^2	
reflectivity for pump	39 % for 1030 nm, p-pol at 45°	
probe pulse at sample	30-72 eV, p-pol, 100 kHz, $80 \times 120\,\mu m^2$	
CCD camera	8x vert. binning, 5°, 3000 kHz readout	
CCD exposure time	1500 ms	900 ms
total acquisition time	2.5 hours	10 hours
acquisition time per delay	1.7 minutes	7 minutes
measured asymmetries per delay	30	160
magnet	±10 A, ±50 mT,	
sample	$Fe_{19}Ni_{81}$ - B2D1118_8 - M. Albrecht Si_3N_4(5 nm)/$Fe_{19}Ni_{81}$(15 nm)/SiO_2(100 nm)/Si	

Table A.1.: Parameters for the EUV T-MOKE measurements on $Fe_{19}Ni_{81}$ presented in chapter 5. The pulse length of the pump beam was determined via an intensity autocorrelation at the position of the sample. The beam sizes were recorded with a beam profiling camera. For the EUV, we only recorded the beam size of the fundamental IR driver at the sample position to get an estimate of the EUV beam size.

HHG generation chamber	1.16 mbar
mirror chamber	$1 \cdot 10^{-4}$ mbar
sample chamber	$8 \cdot 10^{-8}$ mbar
spectrometer	$8 \cdot 10^{-7}$ mbar

Table A.2.: Vacuum conditions in operation with a 100 μm gas nozzle and a backing pressure of 20 bar Argon.

	$Fe_{50}Ni_{50}$	
	M18 - 06.06.2022	M08 - 07.06.2022
	$\theta = 45.2°$	$\theta = 42.5°$
pump pulse at sample	1030 nm, p-pol , 43 fs sech^2, 100 kHz, 500 mW, $550 \times 470\,\mu m^2$	
absorbed pump fluence	$1.13\,\text{mJ/cm}^2$	
reflectivity for pump	35 % for 1030 nm, p-pol at 45°	
probe pulse at sample	30-72 eV, p-pol, 100 kHz, $110 \times 180\,\mu m^2$	
CCD camera	8x vert. binning, 5°, 3000 kHz readout	
CCD exposure time	500 ms	700 ms
total acquisition time	2.5 hours	17 hours
acquisition time per delay	1.6 minutes	12.7 minutes
measured asymmetries per delay	48	306
magnet	±20 A, ±100 mT,	
sample	$Fe_{50}Ni_{50}$ - B220316_1 - M. Albrecht Si_3N_4(3 nm)/$Fe_{50}Ni_{50}$(15 nm)/SiO_2(100 nm)/Si	

Table A.3.: Parameters for the EUV T-MOKE measurements on $Fe_{50}Ni_{50}$ presented in chapter 5. The pulse length of the pump beam was determined via an intensity autocorrelation at the position of the sample. The beam sizes were recorded with a beam profiling camera. For the EUV, we only recorded the beam size of the fundamental IR driver at the sample position to get an estimate of the EUV beam size.

Chapter 5 highlights the results of the ϵ_{xy} analysis for both FeNi alloys in the context of ultrafast spin transfer. Here, figures A.1 and A.2 show the results for the off-diagonal tensor element and the refractive index for all photon energies around the M edges of iron and nickel.

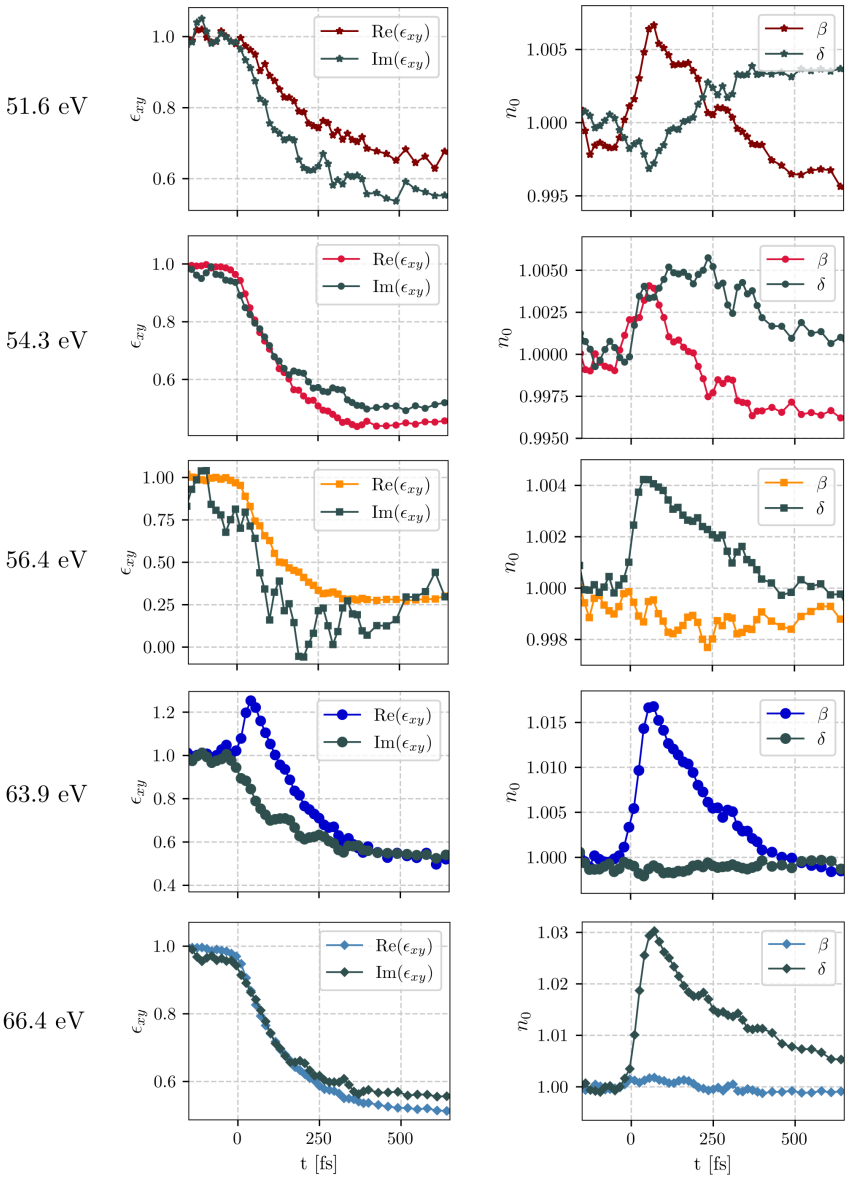

Figure A.1.: Complete results of the ϵ_{xy} analysis for $Fe_{19}Ni_{81}$. The left column shows the dynamics of off-diagonal tensor element normed to their values before the pump pulse arrives. The dynamics of the refractive index n_0 are shown in the right column for the different photon energies.

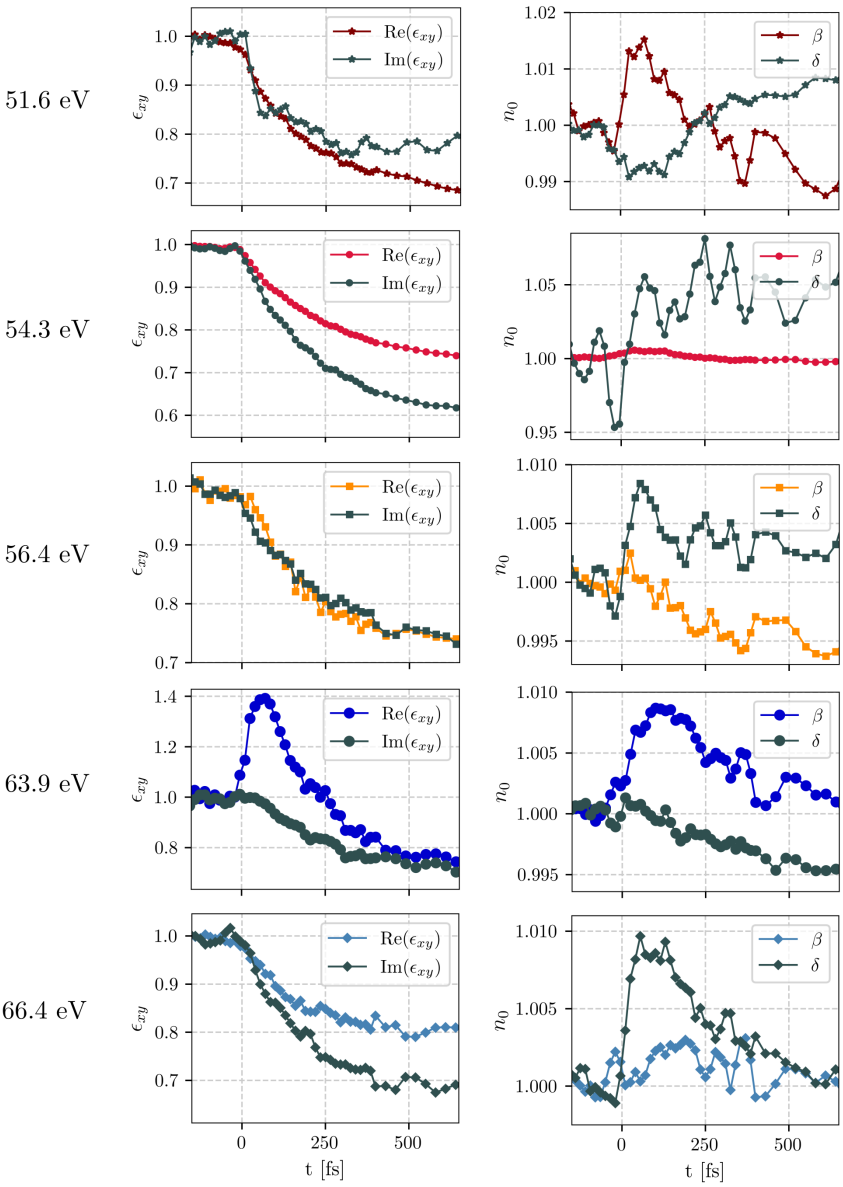

Figure A.2.: Results of the ϵ_{xy} analysis for $Fe_{50}Ni_{50}$. The left column shows the dynamics of off-diagonal tensor element normed to their values before the pump pulse arrives. The dynamics of the refractive index n_0 are shown in the right column for the different photon energies.

Bibliography

[1] K. J. Gaffney and H. N. Chapman. Imaging atomic structure and dynamics with ultrafast X-ray scattering. *Science*, 1444(2007):1444–1449, 2013.

[2] F. Büttner, B. Pfau, M. Böttcher, et al. Observation of fluctuation-mediated picosecond nucleation of a topological phase. *Nature Materials*, 20(1):30–37, 2021.

[3] S. Zayko, O. Kfir, M. Heigl, et al. Ultrafast high-harmonic nanoscopy of magnetization dynamics. *Nature Communications*, 12(1):1–8, 2021.

[4] S. Hell. Far-field optical nanoscopy. *Science*, 316:1153–1158, 2007.

[5] H. N. Chapman and K. a. Nugent. Coherent lensless X-ray imaging. *Nature Photonics*, 4(12):833–839, 2010.

[6] P. U. Jepsen, D. G. Cooke, and M. Koch. Terahertz spectroscopy and imaging - Modern techniques and applications. *Laser and Photonics Reviews*, 5(1):124–166, 2011.

[7] P. M. Kraus, M. Zürch, S. K. Cushing, D. M. Neumark, and S. R. Leone. The ultrafast X-ray spectroscopic revolution in chemical dynamics. *Nature Reviews Chemistry*, 2(6):82–94, 2018.

[8] C. Tzschaschel, T. Satoh, and M. Fiebig. Tracking the ultrafast motion of an antiferromagnetic order parameter. *Nature Communications*, 10(1):1–6, 2019.

[9] J. Lloyd-Hughes, P. M. Oppeneer, T. Pereira Dos Santos, et al. The 2021 ultrafast spectroscopic probes of condensed matter roadmap. *Journal of Physics Condensed Matter*, 33(35), 2021.

[10] P. Oppeneer. Chapter 3: Magneto-optical kerr spectra. volume 13 of *Handbook of Magnetic Materials*, pages 229–422. Elsevier, 2001.

[11] A. Kirilyuk, A. V. Kimel, and T. Rasing. Ultrafast optical manipulation of magnetic order. *Rev. Mod. Phys.*, 82:2731–2784, 2010.

[12] F. Siegrist, J. A. Gessner, M. Ossiander, et al. Light-wave dynamic control of magnetism. *Nature*, 571(240-244), 2019.

[13] S. R. Tauchert, M. Volkov, D. Ehberger, et al. Polarized phonons carry angular momentum in ultrafast demagnetization. *Nature*, 602(7895):73–77, 2022.

[14] A. Kimel, A. Zvezdin, S. Sharma, et al. The 2022 magneto-optics roadmap. *Journal of Physics D: Applied Physics*, 55(463003), 2022.

[15] G. P. Zhang and W. Hübner. Laser-induced ultrafast demagnetization in ferromagnetic metals. *Phys. Rev. Lett.*, 85:3025–3028, 2000.

[16] R. J. Elliott. Theory of the effect of spin-orbit coupling on magnetic resonance in some semiconductors. *Phys. Rev.*, 96:266–279, 1954.

[17] B. Koopmans, G. Malinowski, F. Dalla Longa, et al. Explaining the paradoxical diversity of ultrafast laser-induced demagnetization. *Nature Materials*, 9(3):259–265, 2010.

[18] E. Carpene, E. Mancini, C. Dallera, et al. Dynamics of electron-magnon interaction and ultrafast demagnetization in thin iron films. *Phys. Rev. B*, 78:174422, 2008.

[19] S. Eich, M. Plötzing, M. Rollinger, et al. Band structure evolution during the ultrafast ferromagnetic-paramagnetic phase transition in cobalt. *Science Advances*, 3(3), 2017.

[20] M. Battiato, K. Carva, and P. M. Oppeneer. Superdiffusive spin transport as a mechanism of ultrafast demagnetization. *Phys. Rev. Lett.*, 105:027203, 2010.

[21] D. Rudolf, C. La-O-Vorakiat, M. Battiato, et al. Ultrafast magnetization enhancement in metallic multilayers driven by superdiffusive spin current. *Nature Communications*, 3:1037, 2012.

[22] W. Zhang, P. Maldonado, Z. Jin, et al. Ultrafast terahertz magnetometry. *Nature Communications*, 11(1):1–9, 2020.

[23] R. Rouzegar, L. Brandt, L. c. v. Nádvorník, et al. Laser-induced terahertz spin transport in magnetic nanostructures arises from the same force as ultrafast demagnetization. *Phys. Rev. B*, 106:144427, 2022.

[24] B. Koopmans, M. van Kampen, and W. J. M. de Jonge. Experimental access to femtosecond spin dynamics. *Journal of Physics: Condensed Matter*, 15(5):S723, 2003.

[25] G. P. Zhang, W. Hübner, G. Lefkidis, Y. Bai, and T. F. George. Paradigm of the time-resolved magneto-optical Kerr effect for femtosecond magnetism. *Nature Physics*, 5(7):499–502, 2009.

[26] K. Carva, M. Battiato, and P. M. Oppeneer. Is the controversy over femtosecond magneto-optics really solved? *Nature Physics*, 7(9):665, 2011.

[27] B. Koopmans, M. van Kampen, J. T. Kohlhepp, and W. J. M. de Jonge. Ultrafast magneto-optics in nickel: Magnetism or optics? *Phys. Rev. Lett.*, 85:844–847, 2000.

[28] C. La-O-Vorakiat, M. Siemens, M. M. Murnane, et al. Ultrafast demagnetization dynamics at the M edges of magnetic elements observed using a tabletop high-harmonic soft X-ray source. *Phys. Rev. Lett.*, 103:257402, 2009.

[29] S. Mathias, C. La-O-Vorakiat, P. Grychtol, et al. Probing the timescale of the exchange interaction in a ferromagnetic alloy. *Proceedings of the National Academy of Sciences*, 109(13):4792–4797, 2012.

[30] P. Tengdin, C. Gentry, A. Blonsky, et al. Direct light–induced spin transfer between different elements in a spintronic Heusler material via femtosecond laser excitation. *Science Advances*, 6(3):1–8, 2020.

[31] M. Hofherr, S. Häuser, J. K. Dewhurst, et al. Ultrafast optically induced spin transfer in ferromagnetic alloys. *Science Advances*, 6(3):1–8, 2020.

[32] S. A. Ryan, P. C. Johnsen, M. F. Elhanoty, et al. Optically controlling the competition between spin flips and intersite spin transfer in a Heusler half-metal on sub-100 fs timescales. `arXiv:2305.16455 [cond-mat.mtrl-sci]`, 2023.

[33] C. La-O-Vorakiat, E. Turgut, C. A. Teale, et al. Ultrafast demagnetization measurements using extreme ultraviolet light: Comparison of electronic and magnetic contributions. *Phys. Rev. X*, 2:011005, 2012.

[34] B. Vodungbo, J. Gautier, G. Lambert, P. Zeitoun, and J. Lüning. Comment on "Ultrafast demagnetization measurements using extreme ultraviolet light: Comparison of electronic and magnetic contributions". *Phys. Rev. X*, 3:038001, 2013.

[35] E. Turgut, P. Grychtol, C. La-O-Vorakiat, et al. Reply to "Comment on 'Ultrafast demagnetization measurements using extreme ultraviolet light: Comparison of electronic and magnetic contributions' ". *Phys. Rev. X*, 3:038002, 2013.

[36] S. Jana, R. S. Malik, Y. O. Kvashnin, et al. Analysis of the linear relationship between asymmetry and magnetic moment at the M edge of 3 d transition metals. *Physical Review Research*, 2(1):013180, 2020.

[37] J. K. Dewhurst, F. Willems, P. Elliott, et al. Element Specificity of Transient Extreme Ultraviolet Magnetic Dichroism. *Physical Review Letters*, 124(7):077203, 2020.

[38] I. Radu, C. Stamm, A. Eschenlohr, et al. Ultrafast and distinct spin dynamics in magnetic alloys. *SPIN*, 5(3):1–10, 2015.

[39] A. Eschenlohr. *Element-resolved ultrafast magnetization dynamics in ferromagnetic alloys and multilayers*. PhD thesis, Universität Potsdam, 2012.

[40] S. Jana, R. Knut, S. Muralidhar, et al. Experimental confirmation of the delayed Ni demagnetization in FeNi alloy. *Applied Physics Letters*, 120(10):102404, 2022.

[41] S. Günther, C. Spezzani, R. Ciprian, et al. Testing spin-flip scattering as a possible mechanism of ultrafast demagnetization in ordered magnetic alloys. *Phys. Rev. B*, 90:180407, 2014.

[42] S. Jana, J. A. Terschlüsen, R. Stefanuik, et al. A setup for element specific magnetization dynamics using the transverse magneto-optic Kerr effect in the energy range of 30-72 eV. *Review of Scientific Instruments*, 88(3):033113, 2017.

[43] J. K. Dewhurst, P. Elliott, S. Shallcross, E. K. U. Gross, and S. Sharma. Laser-induced intersite spin transfer. *Nano Letters*, 18(3):1842–1848, 2018.

[44] F. Willems, C. von Korff Schmising, C. Strüber, et al. Optical inter-site spin transfer probed by energy and spin-resolved transient absorption spectroscopy. *Nature Communications*, 11(1):1–7, 2020.

[45] J.-Y. Bigot and M. Vomir. Ultrafast magnetization dynamics of nanostructures. *Annalen der Physik*, 525(1-2):2–30, 2013.

[46] M. Fähnle and C. Illg. Electron theory of fast and ultrafast dissipative magnetization dynamics. *Journal of Physics: Condensed Matter*, 23(49):493201, 2011.

[47] S. Jeppson and R. Kukreja. Capturing ultrafast magnetization phenomenon using femtosecond X-rays. *APL Materials*, 9(10):100702, 2021.

[48] J. Walowski and M. Münzenberg. Perspective: Ultrafast magnetism and THz spintronics. *Journal of Applied Physics*, 120(14), 2016.

[49] K. Carva, M. Battiato, and P. M. Oppeneer. Ab initio investigation of the Elliott-Yafet electron-phonon mechanism in laser-induced ultrafast demagnetization. *Phys. Rev. Lett.*, 107:207201, 2011.

[50] M. Krauß, T. Roth, S. Alebrand, et al. Ultrafast demagnetization of ferromagnetic transition metals: The role of the coulomb interaction. *Phys. Rev. B*, 80:180407, 2009.

[51] A. B. Schmidt, M. Pickel, M. Donath, et al. Ultrafast magnon generation in an Fe film on Cu(100). *Phys. Rev. Lett.*, 105:197401, 2010.

[52] E. Turgut, D. Zusin, D. Legut, et al. Stoner versus heisenberg: Ultrafast exchange reduction and magnon generation during laser-induced demagnetization. *Phys. Rev. B*, 94:220408, 2016.

[53] M. Battiato, K. Carva, and P. M. Oppeneer. Theory of laser-induced ultrafast superdiffusive spin transport in layered heterostructures. *Phys. Rev. B*, 86:024404, 2012.

[54] P. Elliott, N. Singh, K. Krieger, et al. The microscopic origin of spin-orbit mediated spin-flips. *Journal of Magnetism and Magnetic Materials*, 502:166473, 2020.

[55] K. Krieger, J. K. Dewhurst, P. Elliott, S. Sharma, and E. K. U. Gross. Laser-induced demagnetization at ultrashort time scales: Predictions of TDDFT. *Journal of Chemical Theory and Computation*, 11(10):4870–4874, 2015.

[56] J. Chen, U. Bovensiepen, A. Eschenlohr, et al. Competing spin transfer and dissipation at Co/Cu (001) interfaces on femtosecond timescales. *Physical Review Letters*, 122(6):67202, 2019.

[57] D. Steil, J. Walowski, F. Gerhard, et al. Efficiency of ultrafast optically induced spin transfer in Heusler compounds. *Phys. Rev. Research*, 2:023199, 2020.

[58] E. Golias, I. Kumberg, I. Gelen, et al. Ultrafast optically induced ferromagnetic state in an elemental antiferromagnet. *Phys. Rev. Lett.*, 126:107202, 2021.

[59] B. Liu, H. Xiao, and M. Weinelt. Microscopic insights to spin transport driven ultrafast magnetization dynamics in a Gd/Fe bilayer. *Science Advances*, 9(20):eade0286, 2023.

[60] S. Häuser, S. T. Weber, C. Seibel, et al. Competing signatures of intersite and interlayer spin transfer in the ultrafast magnetization dynamics. `arXiv:2304.14957 [cond-mat.mtrl-sci]`, 2023.

[61] S. Sharma. Ultrafast spin, charge and nuclear dynamics. Talk presented at the Online SPICE-SPIN+X Seminars, `https://download.uni-mainz.de/fb08-spice/2021-SPICE-SpinX-Online-Seminar/2021-Spice-SpinX-Online-Seminar-Sharma.pdf`, 2021.

[62] M. F. Elhanoty, O. Eriksson, R. Knut, O. Karis, and O. Granäs. Element-selective ultrafast magnetization dynamics of hybrid Stoner-Heisenberg magnets. *Phys. Rev. B*, 105:L100401, 2022.

[63] H. Probst, C. Möller, M. Schumacher, et al. Unraveling femtosecond spin and charge dynamics with EUV T-MOKE spectroscopy. `arXiv:2306.02783 [cond-mat.mtrl-sci]`, 2023.

[64] D. J. Griffiths. *Introduction to Electrodynamics*. Prentice Hall Inc., 3 edition, 1999.

[65] E. Beaurepaire, H. Bulou, F. Scheurer, and J.-P. Kappler. *Magnetism: A synchrotron radiation approach, lect. notes phys. 697*. Springer, Berlin Heidelberg, 2006.

[66] P. S. Pershan. Magneto-optical effects. *Journal of Applied Physics*, 38(3):1482–1490, 1967.

[67] J. L. Erskine and E. A. Stern. Calculation of the $M_{2,3}$ magneto-optical absorption spectrum of ferromagnetic nickel. *Physical Review B*, 12(11):5016–5024, 1975.

[68] L. D. Landau and E. M. Lifshitz, editors. *Electrodynamics of continuous media*. Pergamon Press, New York, 1960.

[69] I. M. Boswarva, R. E. Howard, and A. B. Lidiard. Faraday effect in semiconductors. *Proceedings of the Royal Society of London. Series A, Mathematical and Physical Sciences*, 269(1336):125–141, 1962.

[70] D. Zusin, P. M. Tengdin, M. Gopalakrishnan, et al. Direct measurement of the static and transient magneto-optical permittivity of cobalt across the entire M edge in reflection geometry by use of polarization scanning. *Physical Review B*, 97(2):1–11, 2018.

[71] H. Höchst, D. Rioux, D. Zhao, and D. L. Huber. Magnetic linear dichroism effects in reflection spectroscopy: A case study at the Fe M2,3 edge. *Journal of Applied Physics*, 81(11):7584–7588, 1997.

[72] H. Ebert. *Magnetic Spectroscopy.* John Wiley and Sons, Ltd, 2007.

[73] R. Kubo. Statistical-mechanical theory of irreversible processes. General theory and simple applications to magnetic and conduction problems. *Journal of the Physical Society of Japan*, 12(6):570–586, 1957.

[74] P. Bruno, Y. Suzuki, and C. Chappert. Magneto-optical Kerr effect in a paramagnetic overlayer on a ferromagnetic substrate: A spin-polarized quantum size effect. *Phys. Rev. B*, 53:9214–9220, 1996.

[75] H. S. Bennett and E. A. Stern. Faraday effect in solids. *Phys. Rev.*, 137:A448–A461, 1965.

[76] A. Scherz. *Spectroscopy of 3d Transition Metals : Systematics and Applications.* PhD thesis, Universität Berlin, 2003.

[77] G. van der Laan and A. I. Figueroa. X-ray magnetic circular dichroism - A versatile tool to study magnetism. *Coordination Chemistry Reviews*, 277:95–129, 2014.

[78] J. Stöhr. Exploring the microscopic origin of magnetic anisotropies with X-ray magnetic circular dichroism (XMCD) spectroscopy. *Journal of Magnetism and Magnetic Materials*, 200(1-3):470–497, 1999.

[79] C. M. Guenther. *Application and Development of Fourier Transform Holography.* PhD thesis, Technische Universität Berlin, 2012.

[80] D. Attwood. *Soft X-Rays and Extreme Ultraviolet Radiation: Principles and Applications.* Cambridge University Press, 1999.

[81] B. L. Henke, E. M. Gullikson, and J. C. Davis. X-ray interactions: Photoabsorption, scattering, transmission, and reflection at E = 50-30,000 eV, Z = 1-92. *At. Data Nucl. Data Tables*, 54(2):181–342, 1993.

[82] A. C. Thompson. X-ray properties of the elements. In *X-Ray Data Booklet.* Lawrence Berkeley National Laboratory, University of California, 2009.

[83] J. Stöhr and H. C. Siegmann. *Magnetism from fundamentals to nanoscale dynamics.* Springer, Berlin Heidelberg, 2006.

[84] S. Sharma, S. Shallcross, P. Elliott, et al. Computational analysis of transient xmcd

sum rules for laser pumped systems: When do they fail? *Applied Physics Letters*, 120(6):062409, 2022.

[85] R. Nyholm, N. Martensson, A. Lebugle, and U. Axelsson. Auger and Coster-Kronig broadening effects in the 2p and 3p photoelectron spectra from the metals ^{22}Ti-^{30}Zn. *Journal of Physics F: Metal Physics*, 11(8):1727, 1981.

[86] M. Vijayakumar and M. Gopinathan. Spin-orbit coupling constants of transition metal atoms and ions in density functional theory. *Journal of Molecular Structure: THEOCHEM*, 361(1):15–19, 1996.

[87] F. Willems, S. Sharma, C. V. Korff Schmising, et al. Magneto-optical functions at the 3p resonances of Fe, Co, and Ni: Ab initio description and experiment. *Physical Review Letters*, 122(21):217202, 2019.

[88] K. Yao, F. Willems, C. von Korff Schmising, et al. Distinct spectral response in M edge magnetic circular dichroism. *Phys. Rev. B*, 102:100405, 2020.

[89] M. Hennes, B. Rösner, V. Chardonnet, et al. Time-resolved XUV absorption spectroscopy and magnetic circular dichroism at the Ni $M_{2,3}$ edges. *Applied Sciences*, 11(1), 2021.

[90] S. Shallcross, C. v. K. Schmising, P. Elliott, et al. Electronic origin of x-ray absorption peak shifts. *Phys. Rev. B*, 106:L060302, 2022.

[91] F. A. Willems. *Ultrafast optical demagnetization dynamics in thin elemental films and alloys : Foundations of and results from helicity-dependent and time-resolved XUV spectroscopy*. PhD thesis, Technische Universität Berlin, 2019.

[92] J. Kerr. On rotation of the plane of polarization by reflection from the pole of a magnet. *The London, Edinburgh, and Dublin Philosophical Magazine and Journal of Science*, 3(19):321–343, 1877.

[93] C. La-o vorakiat. *Element-Selective Ultrafast Magnetization Dynamics with a Tabletop Light Source*. PhD thesis, University of Colorado, 2011.

[94] J. Zak, E. Moog, C. Liu, and S. Bader. Universal approach to magneto-optics. *Journal of Magnetism and Magnetic Materials*, 89(1-2):107–123, 1990.

[95] J. Zak, E. Moog, C. Liu, and S. Bader. Magneto-optics of multilayers with arbitrary magnetization directions. *Physical Review B*, 43(8):6423, 1991.

[96] J. Zak, E. Moog, C. Liu, and S. Bader. Erratum: Magneto-optics of multilayers with arbitrary magnetization directions. *Physical Review B*, 46(9):5883, 1992.

[97] A. Meurer, C. P. Smith, M. Paprocki, et al. SymPy: symbolic computing in Python. *PeerJ Computer Science*, 3:e103, 2017.

[98] K. Yamamoto, Y. Kubota, M. Suzuki, et al. Ultrafast demagnetization of Pt magnetic moment in L_{10}-FePt probed by magnetic circular dichroism at a hard X-ray free electron laser. *New Journal of Physics*, 21(12):0–9, 2019.

[99] B. Watts. Calculation of the Kramers-Kronig transform of X-ray spectra by a piecewise Laurent polynomial method. *Opt. Express*, 22(19):23628–23639, 2014.

[100] M. Hennecke, D. Schick, T. Sidiropoulos, et al. Ultrafast element- and depth-resolved magnetization dynamics probed by transverse magneto-optical kerr effect spectroscopy in the soft x-ray range. *Phys. Rev. Res.*, 4:L022062, 2022.

[101] P. C. Johnsen, S. A. Ryan, C. Gentry, et al. A beamline for ultrafast extreme ultraviolet magneto-optical spectroscopy in reflection near the shot noise limit. *Review of Scientific Instruments*, 94(3):033001, 2023.

[102] C. Möller, H. Probst, J. Otto, et al. Ultrafast element-resolved magneto-optics using a fiber-laser-driven extreme ultraviolet light source. *Review of Scientific Instruments*, 92(6):065107, 2021.

[103] E. Beaurepaire, J.-C. Merle, A. Daunois, and J.-Y. Bigot. Ultrafast spin dynamics in ferromagnetic nickel. *Physical review letters*, 76(22):4250, 1996.

[104] E. Turgut, C. La-O-Vorakiat, J. M. Shaw, et al. Controlling the competition between optically induced ultrafast spin-flip scattering and spin transport in magnetic multilayers. *Physical Review Letters*, 110(19):1–6, 2013.

[105] P. Elliott, T. Müller, J. K. Dewhurst, S. Sharma, and E. K. U. Gross. Ultrafast laser induced local magnetization dynamics in Heusler compounds. *Sci. Rep.*, 6:38911, 2016.

[106] I. Radu, K. Vahaplar, C. Stamm, et al. Transient ferromagnetic-like state mediating ultrafast reversal of antiferromagnetically coupled spins. *Nature*, 472(7342):205–208, 2011.

[107] K. Yao, F. Willems, C. von Korff Schmising, et al. A tabletop setup for ultrafast helicity-dependent and element-specific absorption spectroscopy and scattering in the extreme ultraviolet spectral range. *Review of Scientific Instruments*, 91(9):093001, 2020.

[108] R. Geneaux, H. J. B. Marroux, A. Guggenmos, D. M. Neumark, and S. R. Leone. Transient absorption spectroscopy using high harmonic generation: a review of ultrafast X-ray dynamics in molecules and solids. *Philosophical Transactions of the Royal Society A: Mathematical, Physical and Engineering Sciences*, 377(2145):20170463, 2019.

[109] M. Lewenstein, P. Balcou, M. Y. Ivanov, A. L'Huillier, and P. B. Corkum. Theory of high-harmonic generation by low-frequency laser fields. *Physical Review A*, 49(3):2117–2132, 1994.

[110] T. Popmintchev, M.-C. Chen, P. Arpin, M. M. Murnane, and H. C. Kapteyn. The at-

tosecond nonlinear optics of bright coherent X-ray generation. *Nat. Photon.*, 4(12):822, 2010.

[111] W. Ackermann, G. Asova, V. Ayvazyan, et al. Operation of a free-electron laser from the extreme ultraviolet to the water window. *Nature Photonics*, 1(6):336–342, 2007.

[112] R. W. Schoenlein. Generation of femtosecond pulses of synchrotron radiation. *Science*, 287(5461):2237–2240, 2000.

[113] A. A. Zholents and M. S. Zolotorev. Femtosecond X-ray pulses of synchrotron radiation. *Physical Review Letters*, 76(6):912–915, 1996.

[114] W. Boutu, M. Ducousso, J.-F. Hergott, and H. Merdji. Overview on HHG High-Flux Sources. In F. Canova and L. Poletto, editors, *Optical Technologies for Extreme-Ultraviolet and Soft X-ray Coherent Sources*, Springer Series in Optical Sciences, pages 63–78. Springer, Berlin, Heidelberg, 2015.

[115] S. Hädrich, J. Rothhardt, M. Krebs, et al. Single-pass high harmonic generation at high repetition rate and photon flux. *Journal of Physics B: Atomic, Molecular and Optical Physics*, 49(17):172002, 2016.

[116] S. Yamamoto and I. Matsuda. Measurement of the resonant magneto-optical Kerr effect using a free electron laser. *Applied Sciences*, 7(7), 2017.

[117] C. von Korff Schmising, F. Willems, S. Sharma, et al. Element-specific magnetization dynamics of complex magnetic systems probed by ultrafast magneto-optical spectroscopy. *Applied Sciences*, 10(21):7580, 2020.

[118] C. Alves, G. Lambert, V. Malka, et al. Resonant Faraday effect using high-order harmonics for the investigation of ultrafast demagnetization. *Phys. Rev. B*, 100(14):144421, 2019.

[119] S. Mathias, C. La-o vorakiat, J. M. Shaw, et al. Ultrafast element-specific magnetization dynamics of complex magnetic materials on a table-top. *J. Electron Spectrosc. Relat. Phenom.*, 189:164–170, 2013.

[120] A. Yaresko, A. Perlov, V. Antonov, and B. Harmon. Band-Structure Theory of Dichroism. In E. Beaurepaire, H. Bulou, F. Scheurer, and J.-P. Kappler, editors, *Magnetism: A Synchrotron Radiation Approach*, Lecture Notes in Physics, pages 121–141. Springer, Berlin, Heidelberg, 2006.

[121] M. Hecker, P. M. Oppeneer, S. Valencia, H. C. Mertins, and C. M. Schneider. Soft X-ray magnetic reflection spectroscopy at the 3p absorption edges of thin Fe films. *Journal of Electron Spectroscopy and Related Phenomena*, 144-147:881–884, 2005.

[122] M. Pretorius, J. Friedrich, A. Ranck, et al. Transverse magneto-optical Kerr effect of Fe at the Fe 3p threshold. *Phys. Rev. B*, 55(21):14133–14135, 1997.

[123] O. Pronin, V. Pervak, E. Fill, et al. Ultrabroadband efficient intracavity XUV output coupler. *Opt. Express*, 19(11):10232–10240, 2011.

[124] F. Frassetto, C. Cacho, C. A. Froud, et al. Single-grating monochromator for extreme-ultraviolet ultrashort pulses. *Optics Express*, 19(20):19169, 2011.

[125] W. Cash. Echelle spectrographs at grazing incidence. *Applied Optics*, 21(4):710–717, 1982.

[126] M. Imada, A. Fujimori, and Y. Tokura. Metal-insulator transitions. *Reviews of modern physics*, 70(4):1039, 1998.

[127] Y. Tokura and Y. Tomioka. Colossal magnetoresistive manganites. *Journal of magnetism and magnetic materials*, 200(1-3):1–23, 1999.

[128] V. Moshnyaga and K. Samwer. Ferromagnetic manganite films. *Handbook of Magnetism and Advanced Magnetic Materials*, 2007.

[129] R. Gort, K. Bühlmann, G. Saerens, et al. Ultrafast magnetism: The magneto-optical kerr effect and conduction electrons. *Applied Physics Letters*, 116(11):112404, 2020.

[130] M. Jungbauer, S. Hühn, R. Egoavil, et al. Atomic layer epitaxy of Ruddlesden-Popper SrO ($SrTiO_3$) n films by means of metalorganic aerosol deposition. *Applied Physics Letters*, 105(25):251603, 2014.

[131] K. M. Hoogeboom-Pot, E. Turgut, J. N. Hernandez-Charpak, et al. Nondestructive measurement of the evolution of layer-specific mechanical properties in sub-10 nm bilayer films. *Nano Letters*, 16(8):4773–4778, 2016.

[132] R. J. Stoner and H. J. Maris. Kapitza conductance and heat flow between solids at temperatures from 50 to 300 K. *Phys. Rev. B*, 48:16373–16387, 1993.

[133] H. Meer. Time-resolved spectroscopy on correlated oxides. Master's thesis, University of Göttingen, 2019.

[134] M. Brede. Ultrafast spectrally-resolved spin dynamics in cobalt. Master's thesis, University of Göttingen, 2022.

[135] C. Möller, H. Probst, G. S. M. Jansen, et al. Verification of ultrafast spin transfer effects in FeNi alloys. `arXiv:2306.02793 [cond-mat.mtrl-sci]`, 2023.

[136] G. Malinowski, F. D. Longa, J. H. H. Rietjens, et al. Control of speed and efficiency of ultrafast demagnetization by direct transfer of spin angular momentum. *Nature Physics*, 4(11):855–858, 2008.

[137] A. Melnikov, I. Razdolski, T. O. Wehling, et al. Ultrafast Transport of Laser-Excited Spin-Polarized Carriers in Au / Fe / MgO (001). *Physical Review Letters*, 107(7):076601, 2011.

[138] T. Seifert, S. Jaiswal, U. Martens, et al. Efficient metallic spintronic emitters of ultrabroadband terahertz radiation. *Nature Photon*, 10(7):483–488, 2016.

[139] C. D. Stanciu, F. Hansteen, A. V. Kimel, et al. All-optical magnetic recording with circularly polarized light. *Phys. Rev. Lett.*, 99:047601, 2007.

[140] C.-H. Lambert, S. Mangin, C. B. Varaprasad, et al. All-optical control of ferromagnetic thin films and nanostructures. *Science*, 345(6202):1337–1340, 2014.

[141] S. Schlauderer, C. Lange, S. Baierl, et al. Temporal and spectral fingerprints of ultrafast all-coherent spin switching. *Nature*, 569(7756):383–387, 2019.

[142] A. El-Ghazaly, J. Gorchon, R. B. Wilson, A. Pattabi, and J. Bokor. Progress towards ultrafast spintronics applications. *Journal of Magnetism and Magnetic Materials*, 502:166478, 2020.

[143] J. Minar, S. Mankovsky, O. Sipr, D. Benea, and H. Ebert. Correlation effects in fcc Fe_xNi_{1-x} alloys investigated by means of the KKR-CPA. *Journal of Physics: Condensed Matter*, 26(27):274206, 2014.

[144] J. Dewhurst, K. Krieger, S. Sharma, and E. Gross. An efficient algorithm for time propagation as applied to linearized augmented plane wave method. *Computer Physics Communications*, 209:92–95, 2016.

[145] U. Bierbrauer, S. T. Weber, D. Schummer, et al. Ultrafast magnetization dynamics in nickel: impact of pump photon energy. *Journal of Physics: Condensed Matter*, 29(24):244002, 2017.

[146] J. K. Dewhurst, S. Sharma, and et. al. `elk.sourceforge.net`.

[147] M. Hofherr, S. Moretti, J. Shim, et al. Induced versus intrinsic magnetic moments in ultrafast magnetization dynamics. *Physical Review B*, 98(17):1–7, 2018.

[148] C. Seick, K. Stroh, T. Titze, et al. Energy relaxation in $(La_{0.6}Pr_{0.4})_{0.7}ca_{0.3}mno_3$ films across the metal-insulator transition. *Phys. Rev. B*, 107:085115, 2023.

[149] Y. H. Ren, M. Ebrahim, H. B. Zhao, et al. Time-resolved optical studies of spin and quasiparticle dynamics in colossal magnetoresistance materials: $La_{0.67}Ca_{0.33}MnO_3$, $La_{0.67}Sr_{0.33}MnO_3$, and Sr_2FeMoO_60. *Phys. Rev. B*, 78:014408, 2008.

[150] A. I. Lobad, A. Taylor, C. Kwon, S. Trugman, and T. Gosnell. Laser induced dynamic spectral weight transfer in $La_{0.7}Ca_{0.3}MnO_3$. *Chemical Physics*, 251(1):227–236, 2000.

[151] T. Ogasawara, M. Matsubara, Y. Tomioka, et al. Photoinduced spin dynamics in $La_{0.6}Sr_{0.4}MnO_3$ observed by time-resolved magneto-optical Kerr spectroscopy. *Phys. Rev. B*, 68:180407, 2003.

[152] T. Pincelli, R. Cucini, A. Verna, et al. Transient quantum isolation and critical behavior in the magnetization dynamics of half-metallic manganites. *Phys. Rev. B*, 100:045118, 2019.

[153] J. J. Abel, F. Wiesner, J. Nathanael, et al. Absolute EUV reflectivity measurements using a broadband high-harmonic source and an in situ single exposure reference scheme. *Opt. Express*, 30(20):35671–35683, 2022.

[154] T. Heinrich, H.-T. Chang, S. Zayko, M. Sivis, and C. Ropers. High-sensitivity extreme-ultraviolet transient absorption spectroscopy enabled by machine learning. `arXiv:2305.02236 [physics.optics]`, 2023.

[155] R. Klas, W. Eschen, A. Kirsche, J. Rothhardt, and J. Limpert. Generation of coherent broadband high photon flux continua in the XUV with a sub-two-cycle fiber laser. *Opt. Express*, 28(5):6188–6196, 2020.

[156] M. Sayrac, A. A. Kolomenskii, J. Dong, and H. A. Schuessler. Generation of even and odd harmonics in the XUV region with controlling the relative delay and polarization of two-color fields. *Optik*, 226:165966, 2021.

[157] O. Kfir, E. Bordo, G. Ilan Haham, et al. In-line production of a bi-circular field for generation of helically polarized high-order harmonics. *Applied Physics Letters*, 108(21), 2016.

[158] D. L. Windt, W. C. Cash, M. Scott, et al. Optical constants for thin films of C, diamond, Al, Si, and CVD SiC from 24 A to 1216 A. *Appl. Opt.*, 27(2):279–295, 1988.

[159] C. Tarrio, R. N. Watts, T. B. Lucatorto, J. M. Slaughter, and C. M. Falco. Optical constants of in situ-deposited films of important extreme-ultraviolet multilayer mirror materials. *Appl. Opt.*, 37(19):4100–4104, 1998.

[160] C. J. Kaplan, P. M. Kraus, E. M. Gullikson, et al. Retrieval of the complex-valued refractive index of germanium near the $M_{4,5}$ absorption edge. *J. Opt. Soc. Am. B*, 36(6):1716–1720, 2019.

[161] R. Soufli, A. L. Aquila, F. Salmassi, M. Fernández-Perea, and E. M. Gullikson. Optical constants of magnetron-sputtered boron carbide thin films from photoabsorption data in the range 30 to 770 eV. *Appl. Opt.*, 47(25):4633–4639, 2008.

[162] B. Kjornrattanawanich, D. L. Windt, J. A. Bellotti, and J. F.Seely. Measurement of dysprosium optical constants in the 2-830 eV spectral range using a transmittance method, and compilation of the revised optical constants of lanthanum, terbium, neodymium, and gadolinium. *Appl. Opt.*, 48(16):3084–3093, 2009.

[163] C. Chang, E. Anderson, P. Naulleau, et al. Direct measurement of index of refraction in the

extreme-ultraviolet wavelength region with a novel interferometer. *Opt. Lett.*, 27(12):1028–1030, 2002.

[164] G. S. M. Jansen, X. Liu, K. S. E. Eikema, and S. Witte. Broadband extreme ultraviolet dispersion measurements using a high-harmonic source. *Opt. Lett.*, 44(15):3625–3628, 2019.

[165] K. N. Bobowski. *Magnetization dynamics in the lanthanide metal gadolinium*. PhD thesis, Freie Universität Berlin, 2020.

[166] M. Keunecke, C. Möller, D. Schmitt, et al. Time-resolved momentum microscopy with a 1 MHz high-harmonic extreme ultraviolet beamline. *Review of Scientific Instruments*, 91(6):063905, 2020.

[167] G. S. M. Jansen, M. Keunecke, M. Düvel, C. Möller, et al. Efficient orbital imaging based on ultrafast momentum microscopy and sparsity-driven phase retrieval. *New Journal of Physics*, 22(6):063012, 2020.

[168] M. Keunecke, M. Reutzel, D. Schmitt, A. Osterkorn, T. A. Mishra, C. Möller, et al. Electromagnetic dressing of the electron energy spectrum of Au(111) at high momenta. *Phys. Rev. B*, 102:161403, 2020.

Acknowledgements

First of all, I would like to thank Stefan Mathias for the opportunity to work on this interesting PhD project. I have benefited from your immense expertise and scientific advice as well as the freedom to pursue my own ideas. It has been a great time to see the lab and our group grow. Thank you for the opportunity to attend international conferences and summer schools. Your passion for your research and your enthusiasm are always contagious and inspiring.

I would like to thank Prof. Dr. Claus Ropers for being the second reviewer and Prof. Dr. Simone Techert, PD Dr. Martin Wenderoth, Prof. Dr. Vasily Moshnyaga and PD Dr. Salvatore R. Manmana for being part of the examination board.

I want to thank Henrike Probst for the close, fruitful and sincere teamwork over the last years. We discussed all details, doubts, and crazy ideas and I knew I could always rely on you. Thanks for your great support and our friendship!

Furthermore, I want to thank Daniel Steil – *the* expert in magnetism – for always providing a useful answer to all our questions or problems, and for having a broad overview of the field. Equal thanks go to Matthijs Jansen who strongly supported all T-MOKE projects, in particular with excellent writing and programming skills.

Special thanks go to Johannes Otto for his contribution at the beginning of the project as part of his master's thesis. Without your passion for technical details and your excellent measurement program our setup would not run as smoothly.

Tell me and I forget.
Teach me and I remember.
Involve me and I learn.
- Benjamin Franklin -

I am grateful for the contribution of all master's and bachelor's students who have been involved in various projects over the years. It was a pleasure to work and learn together; Maren Schumacher, Mariana Brede, Lars Matthiesen, Marie Gutberlet, Germaine Arend, and Amelie Schulte.

I would like to thank all technicians at the I. Institute, especially Carsten Mahn, Uta Filip-

pich, and our workshop and the central workshop. Without your excellent technical support and immediate help when something was (urgently) needed, this work would not have been possible.

I would like to thank Philipp, Daniel and Matthijs for proofreading various parts of my thesis.

Thanks to all members of the AG Mathias and the I. Institute for the great time!

Working hard for something we don't care about is called stress.
Working hard for something we love is called passion.

- Simon Sinek -